Measuring galactic distances and metallicity through RR Lyrae optical and infrared light curves

by

Joseph Peter Mullen

A dissertation submitted to the graduate faculty

in partial fulfillment of the requirements for the degree of

DOCTOR OF PHILOSOPHY

Major: Astrophysics

Program of Study Committee:
Massimo Marengo, Co-major Professor
Steven Kawaler, Co-major Professor
Charles Kerton
Cinzia Cervato
James Evans

The student author, whose presentation of the scholarship herein was approved by the program of study committee, is solely responsible for the content of this dissertation. The Graduate College will ensure this dissertation is globally accessible and will not permit alterations after a degree is conferred.

Iowa State University

Ames, Iowa

2023

TABLE OF CONTENTS

LIST OF TABLES

LIST OF FIGURES

ACKNOWLEDGMENTS

First and foremost, I'd like to thank my advisor, Massimo Marengo, for his guidance and encouragement throughout this work. Your enthusiasm and patience in answering countless questions has further cemented my love for astronomy. I'd also like to thank Clara Martínez-Vázquez and my wide group of collaborators for their support and mentoring over the years. I prize the friendships we've been able to develop and look forward to working together on many future endeavors. To all of the astronomy faculty and graduate students at ISU, thank you for teaching me so much and always believing in my abilities.

To my wife, Kylee, I would not have been able to complete this work without your support. Thank you for always prioritizing my education and allowing me countless extra hours of research as you entertained our fickle and cranky newborn.

To my daughter Elliana, I hope this provides proof that anything you dream of doing is possible.

ABSTRACT

RR Lyrae stars (RRLs) are radially pulsating stars that are widely used tracers of old (age > 10 Gyr) stellar populations in the Milky Way and Local Group galaxies. The number of known RRLs has significantly increased with the advent of large-area photometric surveys (e.g., ASAS-SN, Catalina Sky Survey, PanSTARRS, DES, Gaia, TESS). RRLs with known metal abundances remain limited due to the reliance on spectra, which require large amounts of telescope/analysis time and are difficult to obtain at large distances or in high extinction environments. Reliable metallicity measurements are pivotal in utilizing RRLs as distance indicators through standard candle (Period-Luminosity-Metallicity) relations.

Properties of RRL light curves, such as shape (described via Fourier decomposition parameters, e.g., ϕ_{31}), are inherently linked to fundamental parameters such as metallicity. In this work, to derive accurate metallicities from readily available photometry, I present newly-calibrated period-ϕ_{31}-[Fe/H] relations for RRLs in the fundamental (RRab) and first overtone (RRc) mode in the optical (ASAS-SN V-band) and, inaugurally, in the mid-infrared (WISE $W1$ and $W2$ bands). I further present new empirical infrared Period-Luminosity-Metallicity (PLZ) and Period-Wesenheit-Metallicity (PWZ) relations for RRLs based on the latest Gaia EDR3 parallaxes, in the $W1$ and $W2$ bands, as well as in the $W(W1, V - W1)$ and $W(W2, V - W2)$ Wesenheit magnitudes. These works rely upon the same calibration dataset, which provides the largest and most comprehensive span of parameter space to date, with homogeneous spectroscopic metallicities from $\sim$9000 Galactic halo field RRL spanning $-3 < $ [Fe/H] $\lesssim 0.0$. Using the same calibration set and parameter extraction techniques ensures a homogeneous and straightforward application of photometric metallicities to PLZ/PWZ distances.

The optical period-ϕ_{31}-[Fe/H] relations are compared with those available in the literature and are demonstrated to minimize systematic trends in the lower and higher metallicity range. The

relations are directly tested by measuring both the metallicity of the Sculptor dSph and a sample of Galactic globular clusters rich in both RRab and RRc stars. The average metallicity obtained for the combined RRab+RRc sample in each cluster is consistent within ± 0.08 dex of their spectroscopic metallicities, supporting the good performance of this work's optical relations. The infrared relations are shown to possess a similar dispersion to the optical relations. The metallicity error is shown to decrease further when optical and infrared relations are used together.

Finally, the performance of the PLZ and PWZ relations are tested by determining the distance moduli of both galactic and extragalactic stellar associations, including: the Sculptor dwarf spheroidal galaxy in the Local Group (finding $\bar{\mu}_0 = 19.47 \pm 0.06$), the Galactic globular clusters M4 ($\bar{\mu}_0 = 11.16 \pm 0.05$) and the Reticulum globular cluster in the Large Magellanic Cloud ($\bar{\mu}_0 = 18.23 \pm 0.06$). The distance moduli determined through all PLZ/PWZ relations are internally self-consistent (within $\lesssim 0.05$ mag) but are systematically smaller (by $\sim$ 2-3σ) than previous literature measurements taken from a variety of methods/anchors. We link this systematic effect to literature relations based on different parallax anchors (from HST, Gaia DR2, and the newest Gaia DR3) leading to slight differences in zero-points and, in turn, distance. A comparison with recent RRL PLZ/PWZ empirical relations similarly anchored with Gaia EDR3 likewise shows a systematically smaller distance modulus.

The relations obtained in this work greatly impact future studies (such as the Vera Rubin LSST survey and the Roman Space telescope), where we will reach across the Local Group to larger distances and into higher-extinction domains where spectroscopic observations will not be feasible. Knowing the chemical and structural distribution of RRLs, corresponding to some of our galaxy's oldest stellar populations, will better constrain the mechanisms behind galactic formation and evolution.

CHAPTER 1. GENERAL INTRODUCTION

Modern astrometric-based surveys, such as Gaia (Gaia Collaboration et al., 2022), are providing ever-increasing amounts of high-precision 3-dimensional position and motion measurements for a vast quantity of stellar sources. These astrometric measurements are enabling broad structural analyses of the disk and inner halo of the Milky Way. When paired with various methods to determine chemical abundances, this data has been vital in constraining galactic formation models and in providing clues about past merger events (e.g., Belokurov et al. (2019); Koposov et al. (2019); Torrealba et al. (2019)). However, chemical-structural analysis is often truncated to regions where either spectroscopic chemical abundances or parallax distance measurements are more available or reliable (see, e.g., Helmi (2020) for a review). This work seeks to overcome these limitations and expand the ability for chemical-structural analysis to be made in more diverse regions of the Milky Way by leveraging the unique properties of RR Lyrae variable stars as metallicity and distance indicators.

1.1 What are RR Lyrae stars?

RR Lyrae stars (RRLs) are widely used tracers of old (age > 10 Gyr) stellar populations in the Milky Way (MW) and Local Group (LG) galaxies (see e.g., Catelan and Smith (2015); Monelli and Fiorentino (2022) for reviews). RRLs represent a group of low-mass stars, initially very similar to our own sun; however, through natural aging, they have depleted hydrogen in their core and now rely on helium core burning and hydrogen shell burning as their power source. These stars thus fall upon the Horizontal Branch (HB) region of the Hertzsprung-Russell (HR) diagram (a plot of luminosity vs. temperature where a star's position is inherently tied to its physical characteristics and evolutionary state) with RRLs possessing luminosity $\sim$40 L$_\odot$ and mean effective temperatures from $6000-7250$ K (Catelan et al., 2004). The exact location of

RRLs on the HB is inherently tied to its evolutionary point, chemical abundance, and the varying amounts of mass loss during the Red-Giant Branch (RGB) phase. RRLs generally possess a mass ranging from $0.5-0.8$ $M_\odot$.

Due to the initial mass function of our galaxy favoring the production of low-mass stars, RRLs are large in number and nearly ubiquitous through all galactic latitudes and MW components. Furthermore, their luminosity (being evolved HB stars) makes them capable of being observed throughout the LG.
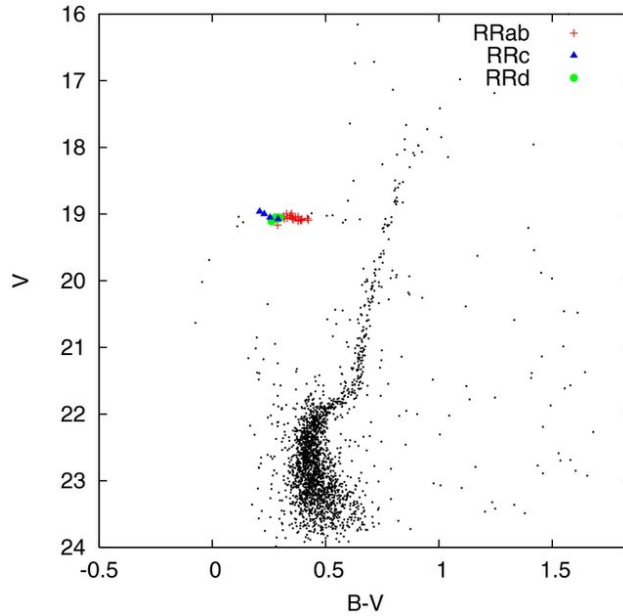
Figure 1.1 $V, B - V$ color magnitude diagram for the Large Magellanic Cloud GC Reticulum. The positions of the RRLs on the HB are indicated. Figure from Kuehn et al. (2013).

In addition to being luminous and ubiquitous, RRLs are easily identifiable as their exact location on the HB intersects that of the instability strip. The location of RRLs on the HB is shown in the color-magnitude diagram of Figure 1.1. Stars in this region radially pulsate due to periodic changes in opacity. RRLs possess a pulsational period between 1.5-24 hours and generally pulsate in either the fundamental (RRab) or first overtone mode (RRc). RRab generally have longer periods, larger amplitudes, and a characteristic saw-toothed/asymmetric-shaped light

curve. The RRc are shorter period variables with much more sinusoidal variations and occupy the bluer $\sim 1/3$ of the HB (see Figure 1.1). RRLs can also pulsate simultaneously in the fundamental and first-overtone modes (RRd). RRd are just mentioned here for completeness, as they only comprise a few percent of the total RRL population.

Stars are not generally prone to pulsation, as stellar interior opacity tends to follow Kramer's law $\kappa \sim \rho/T^{3.5}$ where density increases upon compression of a stellar layer, causing the temperature to increase and opacity to decrease. With stars on the instability strip, a partial ionization zone of singly and doubly ionized helium lies at the ideal depth to drive oscillation. Upon compression of a partial ionization zone, density similarly increases but the extra energy from compression goes to zone ionization. Through this process, the temperature remains relatively constant. This mechanism increases opacity, causing heat and pressure to build behind this layer. Eventually, it will push the layers to expand outwards, where they will cool. At this point, recombination can occur, opacity can drop, and the layers can collapse back and restart the cycle. For stars just outside the instability strip, this partial ionization zone is either too close to the surface that there is not enough gas to effectively drive pulsation (for hotter stars) or too deep so that convection effectively stops pressure build-up (for cooler stars).

1.2   RR Lyrae as distance indicators

RRLs have historically been used to measure distances within the field of astronomy. This is because they are considered to be excellent standard candles – astronomical objects known to possess a specific absolute magnitude from which distance can be inferred by noting the observed apparent magnitude (Smith, 1995). In the optical, they are located within a relatively flat region of the HB on the HR diagram, meaning all RRLs possess an average absolute magnitude of $V \approx 0.5$mag. This relation has been further refined by addressing a small linear metallicity component in the HB and creating a $M_V - [\mathrm{Fe/H}]$ relation. This method is powerful, but has its limitations as it neglects any potential non-linearity with metallicity and assumes all stars are on the zero-age horizontal branch (ZAHB). Typical stellar evolution will result in a gradual redward

progression off the ZAHB, a decrease in surface gravity, and an increase in luminosity. These factors and intrinsic scatter limit the best accuracy to ∼0.1-0.25 mag (Bono et al., 2003). This error can be further compounded as the measurements are being performed in the optical where detailed knowledge of extinction is required.

Moving observations into the infrared could reduce more of the effects of extinction. Additionally, as the Planck function peaks at visible wavelengths for the effective temperatures of RRLs, when one observes at longer wavelengths, the measured monochromatic luminosity moves more toward the Rayleigh Jeans tail of the Planck function. There the temperature dependence is strongly decreased (e.g., V-band flux scales as $R^2 T_{eff}^4$ where K-band flux scales as $R^2 T_{eff}^{1.6}$ for RRLs, Catelan and Smith 2015) . Therefore, in the infrared RRLs become systematically brighter when moving from the blue to the red end of the HB. As there is already a dependence of shorter period RRLs being located more blue-ward, period becomes correlated with luminosity and [Fe/H], and a period-luminosity-[Fe/H] (PLZ) relation can be observed. Taking observations farther in the infrared also causes the slope in the HB to increase and the period dependence to increase, all contributing to a smaller dispersion in PLZ relations. Recent calibrations of this relation produce accuracy of ∼0.1 mag, where most of the error is still dominated by the uncertainty in parallax, even in the Gaia DR3 era (see Gilligan et al. 2021; Neeley et al. 2019).

The accuracy of distances derived from PLZ relations and the ease with which photometry can be readily obtained allow RRLs to be utilized for probing galactic structures beyond the distances provided by parallax measurements. Furthermore, distances to RRLs allow for a cosmological distance ladder based on Population II (older) stars. A distance ladder can be characterized as a succession of calibrations, where a specific type of standard candle is used to calibrate a different type of standard candle that can be found at an even further distance. This method repeats to ever-increasing distances. A revision of the distance ladder has assumed great relevance over the last decade due to the current distance ladder giving statistically different measured values of the Hubble constant (the expansion rate of the universe) when compared to methods based upon the cosmic microwave background radiation (see Riess et al. 2022). The currently utilized distance

ladder is primarily based upon Classical Cepheids, or younger intermediate-mass population I stars also on the instability strip, with their own PLZ relation. A distance ladder based upon RRLs would involve a different independent population of older stars for calibration.

1.3 Limitations to Spectroscopic Metallicity

Chemical abundances of RRLs are crucial to define the chemical enrichment of the older population of our galaxy but are also a necessity for accurate distance calibrations (see Section 1.2). These metallicities for RRLs are often derived through either high-resolution (HR, R $\geq$ 20,000) spectroscopy, yielding a typical metallicity error of ∼0.1 dex, or through medium-resolution (R $\sim$ 2,000) spectra, typically yielding a metallicity error of ∼0.2-0.3 dex. Metallicities extracted through HR spectra require labor-intensive techniques such as fitting to synthetic spectra (i.e., comparison to model atmospheres made by pre-selecting fundamental parameters). Metallicities through medium-resolution spectra can be obtained easier using the ΔS method, which only relies on the difference in equivalent widths between the Ca II K and three Balmer ($H\delta, \gamma, \beta$) lines for a calibration of [Fe/H]. These widely used methods result in accurate [Fe/H] estimates but possess limitations due to their reliance on spectra, as outlined below, that need to be overcome with alternative methods.

1.3.1 Problem A: Inhomogeneity of Metallicity Databases

Due to the large amount of telescope time and analysis time needed to derive accurate HR spectroscopic metallicities, previously available RRL metallicity catalogs tended to list abundances derived from heterogeneous methods and sources, often using different scales. For the creation of PLZ relations, careful consideration has had to be taken into account in the past to ensure the calibration introduces no systematic errors from the inhomogeneity of the source sample. To avoid undue bias, prior PLZ relations would often be derived with either a small selection of uniformly measured RRLs or RRLs belonging to clusters with very well-defined metallicity, assumed to be mono-metallic. When comparing different literature relations with their

own respectively derived PLZ coefficients, inhomogeneity of metallicity is a primary concern that could cause differences in fitting coefficients. Furthermore, in the use of PLZ relations, one must also be concerned that the metallicity utilized is properly scaled with the calibrator metallicities.

1.3.2 Problem B: Keeping Pace with Newly-Discovered RRL

The current era of large-area photometric time surveys has significantly increased the number of known RRL variables, with Gaia DR3 designating ∼270,000 candidate RRLs (Gaia Collaboration et al., 2022). However, the largest spectroscopic metallicity catalog to date covers only ∼ 3% of this sample. The upcoming Vera C. Rubin Observatory Legacy Survey of Space and Time (LSST, Ivezić et al., 2019) will further drastically increase the number of known RRLs as it repeatedly observes the southern night sky with a depth five magnitudes fainter than Gaia, up to ∼400 kpc for RRL (Ivezić et al., 2012). Limited spectroscopic surveys are available, and those present are solely low-resolution. The pace of discovery is so rapid that upcoming planned large-area spectroscopic surveys (such as 4MOST, de Jong et al., 2019) will be unable to keep up.

1.3.3 Problem C: Measurement at Large Distances

Measurements of chemical abundances for some discovered RRL will be unfeasible as spectroscopy becomes increasingly difficult at larger distances. In general, higher resolution spectra require longer exposure times to obtain a good signal-to-noise ratio (SNR). Due to the short pulsational period of RRL, there exists a rapidly changing atmosphere. Too long of exposures can cause smearing of spectral lines from the varying velocity of the atmospheric layers where the lines are formed. The development of large telescopes has lessened the need to consider this for bright nearby RRL, as you can obtain a good SNR in the span of minutes. As RRLs are discovered at ever-increasing distances, such as the outer halo with LSST, this will prove more of an issue. Techniques, such as stacking spectra, can mitigate this effect. Stacking spectra, however, requires a detailed understanding of the pulsational phase for same-phase measurements to take place. The atmosphere of RRLs can undergo temperature changes up to 1000K throughout its

period and be in completely different thermodynamic configurations affecting the profile and strength of the absorption line.

1.3.4   Problem D: Measurement in High-Extinction Environments

The spectroscopic metallicities obtained with the methods discussed above are measured in near-optical wavelengths, with spectra occasionally reaching out into the near-infrared. This wavelength regime poses a limitation as standard spectroscopic techniques cannot hope to probe into high-extinction environments that only mid-IR telescopes can reach. Any RRLs found in these regions with upcoming JWST and Roman (WFIRST) cannot have their abundance measured. As stated in Section 1.2, the intrinsic dispersion in PLZ relations decreases with longer wavelengths. A PLZ relation with luminosity measured in the mid-infrared would benefit if the metallicity could similarly be derived in the mid-infrared without need for optical spectra.

1.4   Motivation and Overview of This Work

To keep up with the pace of RRL discovery, we need a method for measuring metallicities requiring short observing and analysis time. It should also be capable of being measured at both larger distances and in high extinction environments, currently unfeasible for spectroscopic methods. Methods developed should work for both RRab and RRc pulsational modes and provide metallicities consistent with those derived from HR spectroscopic techniques. Whenever possible, an emphasis on homogeneity should be made, whether in the methods, parameters derived, or metallicities used for calibration. Any metallicities produced should be readily applicable and consistent with those used in calibrating a PLZ relation to ensure minimal concerns for bias. Chemical abundances and distances produced should be applied to real-world contexts. Prior to this work, no methods have addressed these needs in entirety.

This dissertation represents the culmination of three published peer-reviewed journal articles (Mullen et al. 2021, Mullen et al. 2022, and Mullen et al. 2023), in which I address all of these concerns. In deriving metallicity, this work relies on the principle that the shape of an RRLs'

light curve is inherently tied to both its period and [Fe/H]. By using readily available and obtainable photometry, the photometric properties of RRLs allow for an analytical relationship between period, light curve shape (i.e., a Fourier decomposition), and metallicity to be derived. The use of period-Fourier-[Fe/H] relations to determine metallicity was first quantified by Jurcsik and Kovacs (1996) in the optical. Since then, multiple relations have been published (see Chap 2 and 3) as each wavelength and pulsation mode have differently shaped light curves that require individual calibrations. The more one moves to longer wavelengths, the more challenging it is to derive meaningful/accurate Fourier parameters. The light curve shape becomes more sinusoidal in nature due to the measured flux lying more upon the Rayleigh Jeans tail where monochromatic luminosity is less temperature dependent (see Section 1.2).

In Chapter 2 (corresponding to Mullen et al. 2021), I present newly-calibrated period-Fourier-[Fe/H] relations for fundamental mode RRLs in the optical and, for the first time, mid-infrared. Throughout this work, homogeneity is emphasized. The calibration metallicities are taken from the largest, most homogeneous metallicity catalog of RRLs to date, comprising of both high and medium-resolution spectra for ∼9,000 RRLs (Crestani et al., 2021). I present novel automated python light curve fitting procedures for homogeneous stellar parameter extraction (including but not limited to period, mean magnitude, and Fourier parameters) that also account for noise and irregularity in time series observations. The precision of the infrared and optical relations are thoroughly assessed with HR spectroscopy and compared with previous optical period-Fourier-[Fe/H] relations found in the literature. I show that most prior optical literature relations possess some degree of systematic trends in derived photometric metallicity. This work explores various reasons behind this issue with alternative methods provided and exemplified by the calibrations of this work. The new period-Fourier-[Fe/H] relations are applied to measure the [Fe/H] abundance in a sample of galactic globular clusters.

Chapter 3 (corresponding to Mullen et al. 2022) builds upon the techniques presented to provide period-Fourier-[Fe/H] relations for first-overtone RRLs in the optical and, for the first time, mid-infrared. Additional validation and calibration techniques are introduced to deal with

further complexities inherent in our RRc sample. For example, a significantly smaller sample exists, as nearly 70-90% of field RRLs pulsate in the fundamental mode. Also, RRc stars possess a more sinusoidal-shaped light curve than RRab. This complicates accurate parameter extraction and introduces contamination, as other variable sources can be confused for RRc. All of the derived photometric calibrations are tested by measuring the metallicity of the Sculptor dSph and a sample of galactic globular clusters, rich in both RRc and RRab stars.

Finally, in Chapter 4 (corresponding to Mullen et al. 2023), I present new empirical PLZ relations (utilizing V, $W1$, and $W2$ bands) based on the latest Gaia EDR3 parallaxes. These relations are calibrated with the same extensive metallicity catalog utilized in the period-Fourier-[Fe/H] fit. This sample set ensures an accurate PLZ calibration (with a wide range of calibrators available for leverage) and the ability to have a straightforward and homogeneous application of photometric metallicities in the PLZ relations. The derived PLZ relations are tested to determine the distance to nearby LMC/MW globular clusters and dwarf galaxies to greater precision. The predicted distance moduli are compared to those in the literature. Through this comparison, I analyze how the RRL-based scale of our galaxy has gradually changed due to differences in PLZ calibrations.

The specific conclusions from these works are presented at the end of each chapter and also summarized in Chapter 5. This work concludes with a look at future opportunities available in using RRL photometric metallicities to analyze galactic chemical-structural evolutionary questions.

1.5   References

Belokurov, V., Deason, A.J., Erkal, D. et al (2019). The Pisces Plume and the Magellanic wake. *Monthly Notices of the Royal Astronomical Society*, 488(1):L47–L52.

Bono, G., Caputo, F., Castellani, V. et al (2003). A pulsational approach to near-infrared and visual magnitudes of RR Lyr stars. *Monthly Notices of the Royal Astronomical Society*, 344(4):1097–1106.

Catelan, M., Pritzl, B.J. and Smith, H.A. (2004). The RR Lyrae Period-Luminosity Relation. I. Theoretical Calibration. *The Astrophysical Journal Supplement Series*, 154(2):633–649.

Catelan, M. and Smith, H.A. (2015). *Pulsating Stars.*

Crestani, J., Fabrizio, M., Braga, V.F. et al (2021). On the Use of Field RR Lyrae as Galactic Probes. II. A New ΔS Calibration to Estimate Their Metallicity. *The Astrophysical Journal*, 908(1):20.

de Jong, R.S., Agertz, O., Berbel, A.A. et al (2019). 4MOST: Project overview and information for the First Call for Proposals. *The Messenger*, 175:3–11.

Gaia Collaboration, Vallenari, A., Brown, A.G.A. et al (2022). Gaia Data Release 3: Summary of the content and survey properties. *arXiv e-prints*, page arXiv:2208.00211.

Gilligan, C.K., Chaboyer, B., Marengo, M. et al (2021). Metallicities from high-resolution spectra of 49 RR Lyrae variables. *Monthly Notices of the Royal Astronomical Society*, 503(4):4719–4733.

Helmi, A. (2020). Streams, Substructures, and the Early History of the Milky Way. *Annual Review of Astronomy and Astrophysics*, 58:205–256.

Ivezić, Ž ., Beers, T.C. and Jurić, M. (2012). Galactic stellar populations in the era of the sloan digital sky survey and other large surveys. *Annual Review of Astronomy and Astrophysics*, 50(1):251–304.

Ivezić, Ž., Kahn, S.M., Tyson, J.A. et al (2019). LSST: From Science Drivers to Reference Design and Anticipated Data Products. *The Astrophysical Journal*, 873(2):111.

Jurcsik, J. and Kovacs, G. (1996). Determination of [Fe/H] from the light curves of RR Lyrae stars. *Astronomy and Astrophysics*, 312:111–120.

Koposov, S.E., Belokurov, V., Li, T.S. et al (2019). Piercing the Milky Way: an all-sky view of the Orphan Stream. *Monthly Notices of the Royal Astronomical Society*, 485(4):4726–4742.

Kuehn, C.A., Dame, K., Smith, H.A. et al (2013). Variable Stars in Large Magellanic Cloud Globular Clusters. III. Reticulum. *Astronomical Journal*, 145(6):160.

Monelli, M. and Fiorentino, G. (2022). RR Lyrae Stars and Anomalous Cepheids as Population Tracers in Local Group Galaxies. *Universe*, 8(3):191.

Mullen, J.P., Marengo, M., Martínez-Vázquez, C.E. et al (2022). Metallicity of Galactic RR Lyrae from Optical and Infrared Light Curves. II. Period-Fourier-Metallicity Relations for First Overtone RR Lyrae. *The Astrophysical Journal*, 931(2):131.

Mullen, J.P., Marengo, M., Martínez-Vázquez, C.E. et al (2023). RR Lyrae Mid-infrared Period-Luminosity-Metallicity and Period-Wesenheit-Metallicity Relations Based on Gaia DR3 Parallaxes. *The Astrophysical Journal*, 945(1):83.

Mullen, J.P., Marengo, M., Martínez-Vázquez, C.E. et al (2021). Metallicity of Galactic RR Lyrae from Optical and Infrared Light Curves. I. Period-Fourier-Metallicity Relations for Fundamental-mode RR Lyrae. *The Astrophysical Journal*, 912(2):144.

Neeley, J.R., Marengo, M., Freedman, W.L. et al (2019). Standard Galactic field RR Lyrae II: a Gaia DR2 calibration of the period-Wesenheit-metallicity relation. *Monthly Notices of the Royal Astronomical Society*, 490(3):4254–4270.

Riess, A.G., Breuval, L., Yuan, W. et al (2022). Cluster Cepheids with High Precision Gaia Parallaxes, Low Zeropoint Uncertainties, and Hubble Space Telescope Photometry. *arXiv e-prints*, page arXiv:2208.01045.

Smith, H.A. (1995). RR Lyrae stars. *Cambridge Astrophysics Series*, 27.

Torrealba, G., Belokurov, V., Koposov, S.E. et al (2019). The hidden giant: discovery of an enormous Galactic dwarf satellite in Gaia DR2. *Monthly Notices of the Royal Astronomical Society*, 488(2):2743–2766.

CHAPTER 2. METALLICITY OF GALACTIC RR LYRAE FROM OPTICAL AND INFRARED LIGHT CURVES: I. PERIOD-FOURIER-METALLICITY RELATIONS FOR FUNDAMENTAL MODE RR LYRAE

Authors

Joseph P. Mullen (1), Massimo Marengo (1), Clara E. Martínez-Vázquez (2), Jillian R. Neeley (3), Giuseppe Bono (4 and 5), Massimo Dall'Ora (6), Brian Chaboyer (7), Frédéric Thévenin (8), Vittorio F. Braga (5 and 9), Juliana Crestani (4, 5, and 10), Michele Fabrizio (5 and 9), Giuliana Fiorentino (5), Christina K. Gilligan (7), Matteo Monelli (11 and 12), Peter B. Stetson (13)

Affiliations

((1) Department of Physics and Astronomy, Iowa State University, Ames, IA, USA, (2) Cerro Tololo Inter-American Observatory, NSF's National Optical-Infrared Astronomy Research Laboratory, La Serena, Chile, (3) Department of Physics, Florida Atlantic University, Boca Raton, FL, USA, (4) Dipartimento di Fisica, Università di Roma Tor Vergata, Roma, Italy, (5) INAF-Osservatorio Astronomico di Roma, Monte Porzio Catone, Italy, (6) INAF-Osservatorio Astronomico di Capodimonte, Napoli, Italy, (7) Department of Physics and Astronomy, Dartmouth College, Hanover, USA, (8) Université de Nice Sophia-antipolis, CNRS, Observatoire de la Côte d'Azur, Laboratoire Lagrange, Nice, France, (9) Space Science Data Center, Roma, Italy, (10) Departamento de Astronomia, Universidade Federal do Rio Grande do Sul, Porto Alegre, Brazil, (11) Instituto de Astrofísica de Canarias, La Laguna, Tenerife, Spain, (12) Departmento de Astrofísica, Universidad de La Laguna, La Laguna, Tenerife, Spain, (13) Herzberg Astronomy and Astrophysics, National Research Council, Victoria, BC, Canada)

2.1 Abstract

We present newly-calibrated period-ϕ_{31}-[Fe/H] relations for fundamental mode RR Lyrae stars in the optical and, for the first time, mid-infrared. This work's calibration dataset provides the largest and most comprehensive span of parameter space to date with homogeneous metallicities from $-3 \lesssim$ [Fe/H] $\lesssim 0.4$ and accurate Fourier parameters derived from 1980 ASAS-SN (V-band) and 1083 WISE (NEOWISE extension, $W1$ and $W2$ bands) RR Lyrae stars with well-sampled light curves. We compare our optical period-ϕ_{31}-[Fe/H] with those available in the literature and demonstrate that our relation minimizes systematic trends in the lower and higher metallicity range. Moreover, a direct comparison shows that our optical photometric metallicities are consistent with both those from high-resolution spectroscopy and globular clusters, supporting the good performance of our relation. We found an intrinsic scatter in the photometric metallicities (0.41 dex in the V-band and 0.50 dex in the infrared) by utilizing large calibration datasets covering a broad metallicity range. This scatter becomes smaller when optical and infrared bands are used together (0.37 dex). Overall, the relations derived in this work have many potential applications, including large-area photometric surveys with JWST in the infrared and LSST in the optical.

2.2 Introduction

RR Lyrae stars (RRLs) are the most widely used tracers of old (age > 10 Gyr, Walker 1989) stellar populations in the Milky Way and Local Group galaxies (see e.g. Catelan and Smith 2015 for a review). They can also be used as standard candles thanks to a well defined M_V vs. iron abundance relation (Caputo, 1998; Sandage, 1990). The recent calibration of theoretical (Marconi et al., 2015; Neeley et al., 2017) and observational (Dambis et al., 2013; Muraveva et al., 2018; Neeley et al., 2019), period-Wesenheit and period-luminosity relations (in the optical and infrared, respectively) have revealed the true potential of these stars as high precision distance indicators. These same studies have highlighted the role of metallicity in determining the absolute brightness of these variables, hence requiring period-luminosity-metallicity (PLZ) and

period-Wesenheit-metallicity (PWZ) relations for a reliable estimate of their distances. Accurate measurements of RRL metal abundances, however, are hard to come by.

Nearly all currently available catalogs (see e.g. Dambis et al. 2013 for a recent large compilation) tend to list [Fe/H] abundances derived with heterogeneous methods and often calibrated with different scales. Metallicities derived from high-resolution spectra ($R \gtrsim 20{,}000$) offer the highest level of precision (~ 0.1 dex, e.g. Chadid et al. 2017; Clementini et al. 1995; Fernley and Barnes 1996; For et al. 2011; Gilligan et al. 2021; Govea et al. 2014; Lambert et al. 1996; Magurno et al. 2019, 2018; Nemec et al. 2013; Pancino et al. 2015), but require large amounts of telescope and analysis time, and therefore exist only for a small number of stars. Medium-resolution spectroscopic surveys ($R \sim 2{,}000$), however, are available for larger samples of RRLs. For example, over 2,300 sources found in the Sloan Extension for Galactic Understanding and Exploration (SEGUE) survey (Yanny et al., 2009), and another $\sim 3{,}000$ targets from the Large Scale Area Multi-Object Spectroscopic Telescope (LAMOST) DR2 survey (Deng et al., 2012; Liu et al., 2014), can also be leveraged to derive iron abundances. This is traditionally achieved with the ΔS method (Preston, 1959), which relies on ratios between the equivalent widths of Ca and H lines. Recent applications of this method are shown in both Liu et al. (2020), which is based on a fit of theoretical models and utilizes LAMOST data, and Crestani et al. (2020) (C21 hereafter), which is based upon empirical calibrators and is shown to be valid for both SEGUE and LAMOST data. These applications demonstrate the viability of the ΔS method in providing homogeneous [Fe/H] abundances with an uncertainty of 0.2-0.3 dex.

While the ΔS method allows a dramatic expansion to the sample of RRLs with known metallicity to thousands of sources, it still requires spectra. As such, it is not directly applicable to the much larger number of RRLs that will be discovered within the Milky Way and the other Local Group galaxies by upcoming large area photometric surveys such as the Rubin observatory Legacy Survey of Space and Time (LSST) (Ivezić et al., 2019) in the optical, and surveys that will be executed for the Roman telescope (Akeson et al., 2019) at near-infrared wavelength. A reliable and precise method to derive metallicities from photometric time series is necessary to enable an

expansion of such measurements to distances where taking spectra is not possible at all, or in high extinction environments that can only be probed photometrically by mid-infrared telescopes such as the James Webb Space Telescope (JWST) (Gardner et al., 2006).

Early work by Jurcsik and Kovacs (1996) (JK96 hereafter) has demonstrated that at optical wavelengths the shape of the light curve of fundamental mode RRLs (RRab) is related to their metallic abundance. In particular, they derived a linear relation connecting RRab's [Fe/H] abundance with period and low order parameters in the Fourier decomposition of the star's light curve in the V-band, with the phase parameter $\phi_{31} = \phi_3 - 3 \cdot \phi_1$ providing the most sensitive diagnostics. Further work by Nemec et al. (2013) (hereafter N13), Martínez-Vázquez et al. (2016) (hereafter MV16), Smolec (2005), Ngeow et al. (2016), and Iorio and Belokurov (2020) (hereafter IB20) extended this analysis, respectively, to well-sampled RRab light curves obtained with the Kepler space telescope (Koch et al., 2010), to include stars in globular clusters, to the Optical Gravitational Lensing Experiment (OGLE, Udalski et al. 1992) I-band, to the Palomar Transient Factory (PTF, Law et al. 2009) R-band, and by using Gaia DR2 (Clementini et al., 2019; Gaia Collaboration et al., 2018; Holl et al., 2018) G-band light curves.

In this work, we take advantage of both the large sample of homogeneous HR [Fe/H] abundances in C21 and apply the ΔS calibration of C21 to the full medium-resolution LAMOST DR6 and SDSS-SEGUE datasets to build an extensive HR+ΔS metallicity catalog. We have cross-matched the variables in the HR+ΔS metallicity catalog with well-sampled photometric time series in the All-Sky Automated Survey for Supernovae (ASAS-SN, Jayasinghe et al. 2018; Shappee et al. 2014) and the Near-Earth Objects reactivation mission (NEOWISE, Mainzer et al. 2011) of the Wide-field Infrared Survey Explorer (WISE, Wright et al. 2010). We have then derived novel period-ϕ_{31}-[Fe/H] relations in the optical (V-band) and, for the first time, mid-infrared ($W1$ and $W2$ bands). Our work shows that these relations can indeed be extended to the thermal infrared, where the light curves are mostly determined by the radius variation during the star's pulsation rather than the effective temperature changes that dominate in the

optical wavelengths. As mentioned above, this will be crucial to allow the determination of reliable metallicities in upcoming space infrared surveys.

This paper is structured as follows. In Section 2.3, we describe in detail the data sets we adopt for our work: the HR+ΔS metallicity catalog utilizing the work of C21, the ASAS-SN and WISE time-series catalogs, and the light curves for a sample of Galactic globular clusters with known metallicity that we will use to validate our relations. In Section 2.4, we explain how our period-ϕ_{31}-[Fe/H] relations are calibrated and validated. Our results are discussed in Section 2.5, where we assess the precision of the infrared and optical relations, compare our relations with previous ones found in literature, and apply our method to measure the [Fe/H] abundance in the sample of Galactic globular clusters. Our conclusions are presented in Section 2.6.

2.3 Field and Globular Cluster Fundamental RR Lyrae Datasets

In this section, we describe the properties of the sample of RRLs with known spectroscopic [Fe/H] abundances that we have adopted to calibrate our period-ϕ_{31}-metallicity relations. From this catalog, we have derived three *calibration samples*: one with V-band time-series (*ASAS-SN sample*), one with photometric data available in the thermal infrared (*WISE sample*), and one with data in both wavelengths (*joint sample*). The properties of these calibration samples are described in the following sections and listed in Table 2.1.

2.3.1 Calibration Sample

As mentioned before, the sources selected for this analysis are chosen from both the high-resolution metallicity catalog of C21 and the full medium-resolution LAMOST DR6 and SDSS-SEGUE datasets, from which the spectrum selection criteria and ΔS metallicity calibration of C21 have been applied. The resultant HR+ΔS metallicity catalog is comprised of 8660 fundamental mode field RRLs that have also been cross-matched with the Gaia EDR3 database

Table 2.1   Fundamental mode RR Lyrae calibration sample

	ASAS-SN	WISE		Joint sample
Bands	V	$W1$	$W2$	V, ($W1$ or $W2$)
RRab stars	1980	1083	707	967
Period in days (range)	0.36 - 0.89	0.36 - 0.85	0.36 - 0.85	0.36 - 0.85
Period in days (mean value)	0.57	0.57	0.57	0.57
[Fe/H] (range)	-3.06 - $(+0.36)$	-3.06 - $(+0.36)$	-3.06 - $(+0.36)$	-3.06 - $(+0.36)$
[Fe/H] (mean value)	-1.47	-1.46	-1.44	-1.45
Number of epochs (range)[1]	69 - 892	153 - 879	153 - 879	$\cdots$
Number of epochs (mean value)	270	231	233	$\cdots$
Magnitude (range)	9.55 - 17.41	7.85 - 14.76	7.87 - 14.11	$\cdots$

(Collaboration et al., 2020), as well as a number of other publicly available datasets, using an algorithm specifically developed for sparse catalogs (Marrese et al., 2019).

The HR+ΔS metallicity catalog provides both a homogenized sample of RRab iron abundances gathered from various sources in literature (170 of which are derived from high-resolution spectra) and similarly homogeneous new ΔS metallicity estimates, as the ΔS calibration of C21 is based in part on the metallicity of 111 of the aforementioned HR RRab stars. For a complete and detailed description of the HR metallicity catalog's demographics, the ΔS calibration, and the spectrum selection criterion, we refer the reader to the C21 paper.

All metallicities in this catalog are based upon the metallicity scale utilized by C21, which is based upon high-resolution spectroscopy, and the most updated iron line parameters, most of which have transition parameters derived in laboratory studies. This is the same scale utilized by For et al. (2011), Chadid et al. (2017), and Sneden et al. (2017), and will be the default scale used throughout this paper unless otherwise declared. Note, other literature field-RRL high-resolution works can be brought to the same metallicity scale with the addition of a simple offset. A full analysis of the offsets between various HR [Fe/H] scales is offered in C21. It is worth mentioning

---

[1]The distribution of epochs is recorded prior to removing any spurious photometric measurement, as described in Section 2.4.
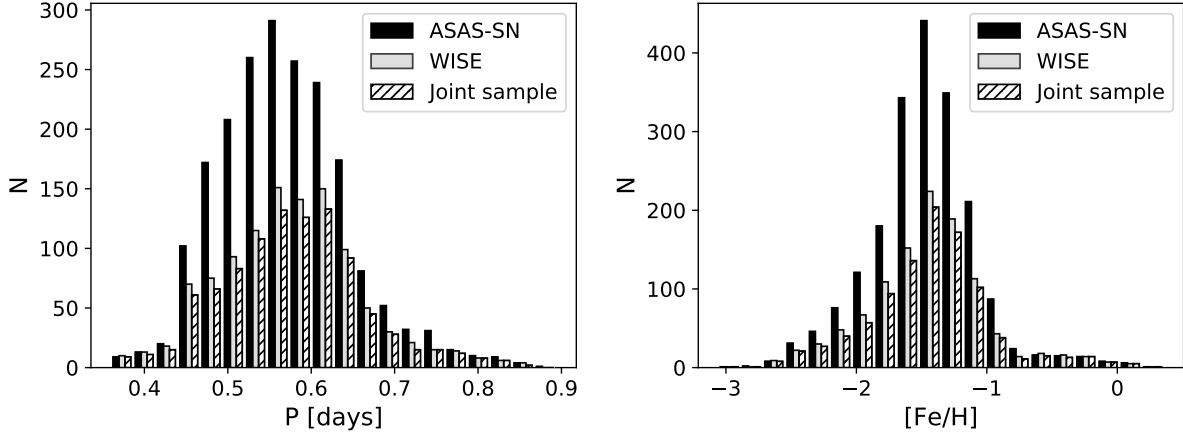
Figure 2.1   Period distribution (left) and spectroscopic [Fe/H] distribution (right) of the different calibration datasets. The histogram labeled "joint sample" (hatched) corresponds to those stars in common between the ASAS-SN (optical V-band, in black) and WISE (infrared $W1$, $W2$ bands, in grey) datasets.

here that the often used Carretta et al. (2009, C09) [Fe/H] scale can be converted to this works scale with the addition of a small rigid shift of 0.08 dex.

In this work, we focus on the stars in the HR+ΔS metallicity catalog that have a match in the ASAS-SN and WISE surveys. Figure 2.1 shows the distribution of period and metallicity for the subset of stars with available optical (ASAS-SN) or infrared (WISE) *good quality* light curves (i.e. passing the stringent photometric and Fourier decomposition criteria described in Section 2.4). The joint sample, also shown in the figure, comprises the smaller subset of RRLs with light curves available at both optical and infrared wavelengths. All samples cover the entire period range expected for RRab variables and are well representative of the metallicity of Galactic Halo RRLs, with a mean [Fe/H] abundance of ≈ -1.45 in both the ASAS-SN and WISE samples. Figure 2.1 also shows that all histograms retain both the low metallicity [Fe/H] $\lesssim -2.2$ and the high metallicity [Fe/H] $\gtrsim -0.7$ tail present in the C21 catalog. For a discussion of the significance of populations in the Galactic Halo, we refer to Fabrizio et al. (2019)(hereafter F19). Here, we want

to remark how the broad range in metallicity is an important feature of our samples, as it ensures broad leverage for accurate calibration of the metallicity slope in our period-ϕ_{31}-[Fe/H] relation.

2.3.2   Field RRLs Optical Data

The optical (V-band) time series data for this analysis have been extracted from the ASAS-SN survey. The first telescope of ASAS-SN came online in 2013, and telescopes have gradually been added for a total of 24 telescopes scattered across the world as of early 2020. At its current capacity, ASAS-SN can survey the entire sky every night, providing high cadence V-band photometry, ideally suited to acquire long term, densely populated light curves of RRLs.

Out of the 6079 variables in the HR+ΔS catalog with a match in ASAS-SN, we were able to extract good quality ASAS-SN light curves for 1980 stars using the procedure described in Section 2.4. Of these, 967 are in the joint sample, also having good quality light curves in the infrared. The left panel of Figure 2.2 shows the distribution of average V-band apparent magnitudes for both the entire optical dataset (solid black) and the stars in the joint sample (hatched). The cut-off at $V \simeq 17.4$ is due to the limiting magnitude of the ASAS-SN survey. The joint sample is instead truncated at $V \simeq 16$ due to the shallower photometric depth of the WISE survey. For a detailed description of the generation of the light curves from the ASAS-SN time-series, and calculation of average magnitudes for this dataset, we refer to Section 2.4.2.

2.3.3   Field RRLs Infrared Data

We obtained archival infrared photometric time-series from the WISE mission $W1$ and $W2$ bands (3.4 and 4.6 μm respectively). The primary WISE mission surveyed the entire sky in four infrared bands every six months from January 2010 to the end of the post cryogenic phase in February 2011. The spacecraft was then reactivated in September 2013 in just the $W1$ and $W2$ bands as the NEOWISE mission. Still having sensitivity similar to the full cryogenic phase, NEOWISE, as of early 2020, has yielded 12 additional full-sky survey epochs (having a minimum
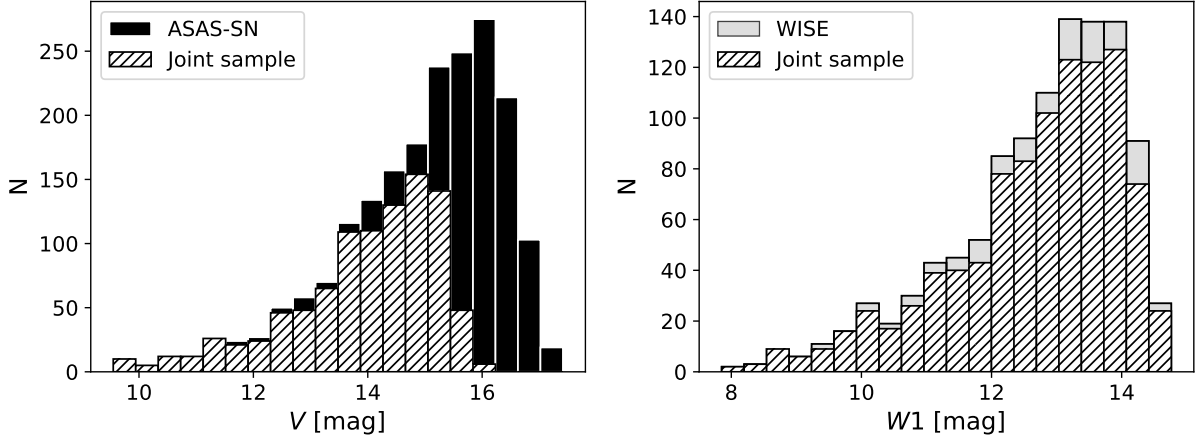
Figure 2.2   Distribution of the average V-band apparent magnitude (left) and the average $W1$-band apparent magnitude (right). Each panel shows both the entire calibration sample (solid fill) and the joint sample (hatched fill, subset of stars having both ASAS-SN and WISE data).

of 12 measurements per survey epoch). With a minimum of $\sim$156 individual epochs ($\sim$12 from WISE and 144 from NEOWISE) for each position in the sky, collected over a baseline of almost ten years, the combined WISE and NEOWISE photometry provide the most comprehensive full-sky catalog in the infrared. From hereafter in the paper, the combination of photometry from both the primary WISE and ongoing NEOWISE mission will be referred for brevity as WISE.

Out of 6264 sources in the HR+ΔS with a WISE catalog match, we were able to generate 1083 good quality light curves in at least one of the two adopted WISE bands (1083 and 707 stars in the $W1$ and $W2$ bands, respectively). Figure 2.2 (right panel) shows the WISE distribution of the average $W1$ apparent magnitude, for both the entire infrared dataset (solid grey) and those stars in the joint sample (hatched). Although the WISE sensitivity limit is ~ 16 mag in the two bands of interest, the figure shows a sharp drop at $W1 \simeq 14.7$; fainter RRLs, while detected in the WISE and NEOWISE catalogs, tend to have noisy light curves that are then rejected by the quality control procedures described in Section 2.4. The histogram for the $W2$-band is similar, although the cut-off in the magnitude distribution happens at $W2 \simeq 14.1$ due to the lower

sensitivity in this band, resulting in noisier light curves. The magnitude range and other characteristics in the joint sample subset of WISE bands are nearly the same as the complete infrared dataset due to the large overlap with available ASAS-SN data.

2.3.4   Globular Cluster Dataset

Lastly, we select a dataset separate from those used in deriving our period-ϕ_{31}-[Fe/H] relations to use as an independent check of this work (see Section 2.5.2). This dataset is comprised of eight globular clusters (GCs) homogeneously spread between [Fe/H] $= -1.1$ and -2.3 dex with a sizable number of RRab stars. These clusters are listed in Table 2.2. The GC dataset comes mainly from the homogeneous photometric database of P. B. Stetson[2] (hereafter, PBS), except for NGC 3201 data, which comes from Piersimoni et al. (2002). The data in the PBS database was collected from ground-based telescopes using archival data from 1984 to present. The main telescopes and cameras which contributed the most to the V-band data used in this work include the following: AAO LCOGT 1m (CCD), CTIO 0.9m (Tek2K), CTIO 1m (Y4KCam), CTIO 1.3m (ANDICAM), CTIO LCOGT 1m (CCD), Cerro Pachón SOAR 4.1m (SOI), La Silla NTT 3.6m (EMMI TK2048EB), La Silla ESO/MPI 2.2m (WFI), LCO Warsaw 1.3m (8k-MOSAIC), Maunakea CFHT 3.6m (CFH12K), ORM La Palma JKT 1m (EEV7), ORM La Palma INT 2.5m (WFC), SAAO LCOGT 1m (CCD). For further information about the summary of observing runs for each cluster, the bands observed, and the imagers and telescopes used, we direct the reader to the PBS database (previously mentioned).

The spectroscopic metallicities of these GCs (second column in Table 2.2) are listed in the scale of C09, and the third column of Table 2.2 shows the total number of fundamental mode RRLs in each GC according to Clement's catalog[3] (Clement et al., 2001). In parentheses, we list the number of RRab actually available in the PBS photometry. In addition, the average number of epochs per V-band light curve is shown in the fourth column.

---

[2]https://www.canfar.net/storage/list/STETSON/homogeneous
[3]http://www.astro.utoronto.ca/~cclement/read.html

Table 2.2   Globular cluster validation sample

Clusters	$[\mathrm{Fe/H}]_{C09}$	RRab stars[4]	Epochs
NGC 7078 (M15)	-2.33	64 (64)	223
NGC 4590 (M68)	-2.27	14 (13)	41
NGC 4833	-1.89	11 (11)	72
NGC 5286	-1.70	30 (25)	111
NGC 3201	-1.51	72 (50)	80
NGC 5272 (M3)	-1.50	177 (175)	167
NGC 5904 (M5)	-1.37	90 (67)	87
NGC 6362	-1.07	18 (18)	80

2.4   Calibration of Period-Fourier-Metallicity relation

Before folding the ASAS-SN and WISE time-series into phased light curves, we ensured that they had at least 30 available epochs, had a $S/N > 5$, and no quality or contamination flags in their original archive. Most time-series passed this check.

Figure 2.3 shows the V, $W1$, and $W2$ light curve typical for two of our stars with good-quality photometry and optimal phase sampling. While the V-band has the characteristic saw-tooth shape of RRab variables, with a sharp minimum and maximum connected by a quick rise, the infrared curves are more symmetric and sinusoidal, with a broad maximum, still retaining a sharp minimum. As mentioned above, this is a consequence of optical light curves being more sensitive to changes in the star's effective temperature, while the variations in radius are the determinant factor for the infrared light curves. We take advantage of these wavelength-dependent properties by deriving separate calibrations of the period-ϕ_{31}-[Fe/H] in the optical and infrared, allowing us to probe different aspects of RRLs stellar atmospheric physics.

This section describes the procedure we followed to fit and validate our relations: (a) we first refine the nominal period of each variable found in the literature by taking advantage of the large time-coverage of our ASAS-SN and WISE time series; (b) we then smooth the phased light curves

---

[4]The number of RRab listed in each GC is according to Clement's catalog (Clement et al., 2001), where the actual number of RRab available with the PBS photometry is in parentheses.

to prepare them for efficient Fourier analysis and perform quality control on the light curves to remove noisy data; (c) we calculate the Fourier decomposition and identify the parameters that are best correlated with metallicity and (d) we finally fit the period-ϕ_{31}-[Fe/H] relations.
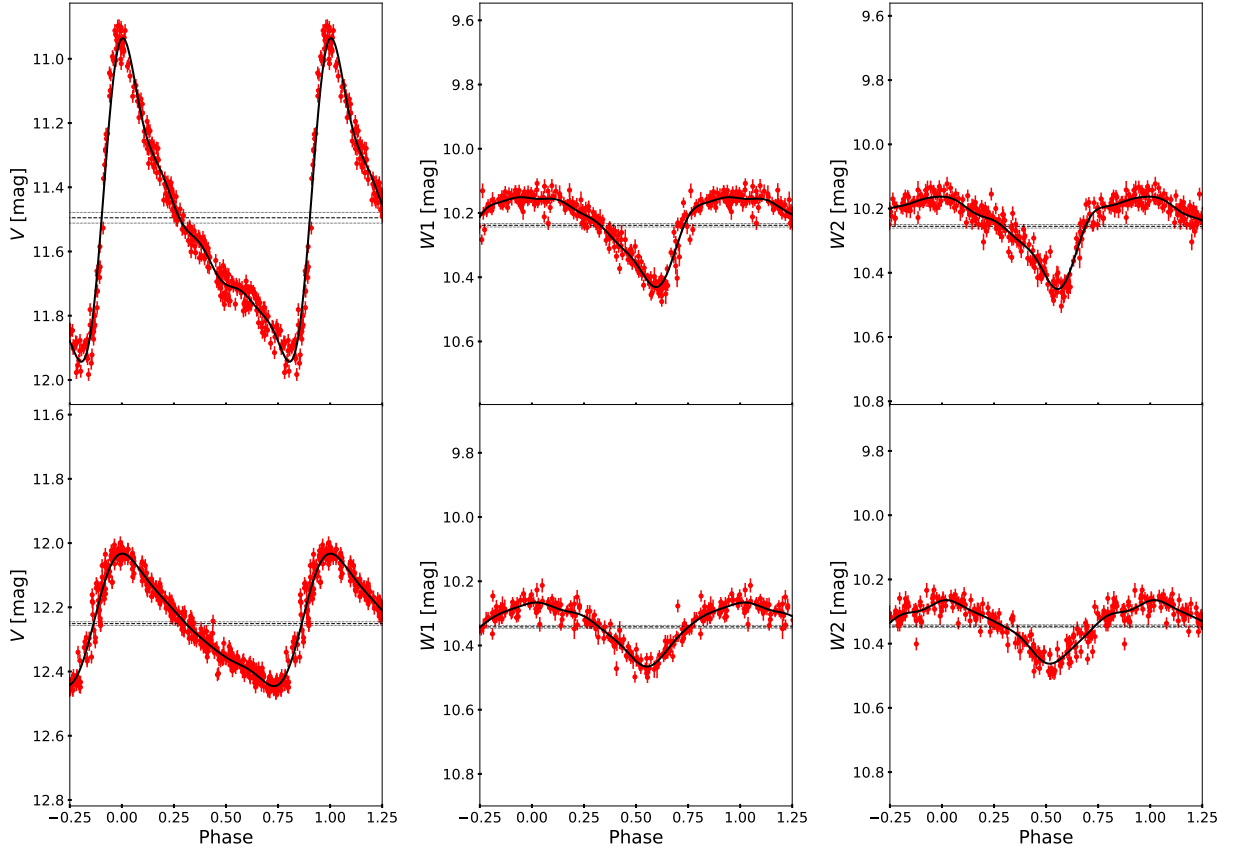
Figure 2.3   Multiple-band light curves for a typical short and long period star. The V (left), $W1$ (middle), and $W2$ bands (right) are shown for the star DM Cyg (Period = 0.419866 days) in the top row and NSVS 13688631 (Period = 0.737646 days) in the bottom row. The Fourier fit (black solid line) to the GLOESS light curve (see text) is plotted on top of the phased data (red). The average magnitude with its associated error are shown as horizontal black dotted lines. Points automatically rejected by the GLOESS fitting procedure have been removed.

2.4.1 Period Determination

The large temporal baseline of the ASAS-SN and WISE surveys makes our time-series very sensitive to even small errors in the nominal period of the stars. Even inaccuracies of 10^{-6} days, over the 10 years span of WISE and its extended mission, result in a $\sim 0.7\%$ phase shift when the photometric time series of a 0.55 day period of our typical RRab star is phased, readily detectable in our datasets. To avoid this issue, we have re-derived the periods of all our stars on the basis of their V and $W1$ band[5] photometry, using the Lomb-Scargle method (Lomb, 1976; Scargle, 1982) within a search window from 0.2 to 1.5 days.

Typical re-derived periods differ from the ones in the literature by 10^{-5} days or less. Light curves with period discrepancy larger than 10^{-5} days between the V and $W1$ datasets, or with the nominal period from literature, were inspected manually for further quality checks and possible rejection. Approximately 5% of derived periods fell in this category and required manual inspection. The inability to find a reliable period was also used as a rejection criterion for an individual light curve. Note that this quality assurance process causes the removal of some high amplitude Blazhko stars (Blažko, 1907), due to their naturally larger dispersion in the light curve causing a high "false alarm" probability in the period determination returned by the Lomb-Scargle routine. This removal is intended, as the photometric modulation of Blazhko stars can affect the Fourier decomposition of their light curves, complicating the dependence of [Fe/H] from period and ϕ_{31} (see e.g. Skarka 2014).

2.4.2 GLOESS Light Curve Smoothing and Quality Control

Rather than directly calculate the Fourier decomposition of the phased light curve, we elected to smooth it first to better deal with the uneven sampling of the observing epochs, and primarily to allow the removal of data points with excessive noise. The smoothing was performed using a Gaussian locally-weighted regression smoothing algorithm (GLOESS, Persson et al. 2004). This method places the phased light curve on an interpolated grid, to which a second-degree

---

[5]We did not use the $W2$-band for period determination due to its larger photometric error, often leading to less accurate periods.

polynomial is locally fit to the photometric data. Fitting weights depend on both the photometric error and the Gaussian distance of the phased photometry from the interpolation point. The procedure was repeated multiple times in order to apply an iterative sigma clipping rejection scheme, designed for noisy data point removal. Only time series with a minimum of 30 valid photometric data points after sigma clipping were retained for processing, with the rest excluded from further consideration. A full description of our implementation of the GLOESS method is available in Neeley et al. (2015).

Figure 2.3 shows example light curves of the phased data (red points) for both a typical short and long period RRL star (DM Cyg and NSVS 13688631, respectively). Data points automatically rejected by the GLOESS fitting procedure are removed. From the GLOESS light curve, we have measured the mean magnitude (calculated as the mean of the smoothed light curve in flux units, converted back to magnitude), the amplitude, and the epoch of maximum (separately in each band). The mean magnitude uncertainty was calculated as the sum in quadrature of the photometric uncertainty and the uncertainty in the fit (see Neeley et al. 2015 for details). The error associated with the amplitude was instead defined as the standard deviation of the data points residuals with respect to the smoothed light curve. Stars with an amplitude equal to less than three times the amplitude error were found to correspond to excessively noisy light curves and were excluded from further analysis. Note that this process also excluded large modulation Blazhko stars, which would appear as noisy light curves with large uncertainty in amplitude.

2.4.3 Fourier Decomposition

Fourier decomposition is a widely adopted tool to quantify the shape of a light curve, as the lower order terms in the expansion are usually sufficient to fully characterize its shape (see e.g. Simon and Lee 1981). As justified above, for this work we elected to perform Fourier expansion of the evenly spaced smoothed light curves, rather than the individual data points, in the form:

$$m(\Phi) = A_0 + \sum_{i=1}^{n} A_i \sin[2\pi i(\Phi + \Phi_0) + \phi_i] \tag{2.1}$$

where $m(\Phi)$ is the observed magnitude for either the ASAS-SN or WISE bands, A_0 is the mean magnitude, n is the order of the expansion, Φ is the phase from the GLOESS light curve varying from 0 to 1, Φ_0 is the phase that corresponds to the time of maximum light T_0, and the A_i's and ϕ_i's are the i-th order Fourier amplitude and phase coefficients, respectively.

We determined the Fourier coefficients with a weighted least-squares fit of Equation 2.1 to the smoothed GLOESS light curve and its locally calculated error. The locally calculated error was defined as the local photometric scatter around the smoothed light curve, estimated as the weighted standard deviation of the residual with the data convolved with the GLOESS smoothing kernel. We found that a fifth-order ($n = 5$) Fourier expansion was sufficient to reproduce the shape of the light curve in each band. Examples are shown in Figure 2.3 for two typical RRLs. The Fourier decomposition fit (black solid line) is plotted on top of the actual photometric data in red.

Simon and Lee (1981) first showed that certain combinations of Fourier coefficients were directly related to some physical parameters of pulsating stars. These coefficients are typically defined either as linear combinations of Fourier phases:

$$\phi_{ij} = j \cdot \phi_i - i \cdot \phi_j \tag{2.2}$$

where ϕ_{ij} is cyclic in nature and ranges from 0 to 2π, or as ratios of the Fourier amplitudes:

$$R_{ij} = \frac{A_i}{A_j} \tag{2.3}$$

In Appendix 2.8, we discuss the correlation between various combinations of Fourier parameters among themselves, and with period, and how they help discriminate sources with different metallicities. Our analysis confirms the conclusions of early studies such as JK96, suggesting that a relation between period and ϕ_{31} is a good indicator of metallicity in the V-band. We found this to be true also in the infrared. Uncertainties in the calculated ϕ_{31} values are several orders of magnitude less than our best uncertainties in metallicity and are therefore deemed negligible throughout the rest of this work.
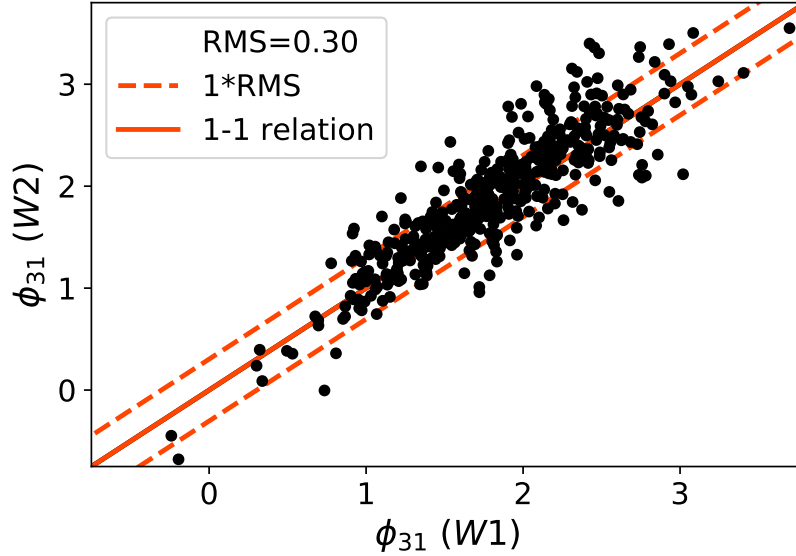
Figure 2.4   Comparison between $W1$ and $W2$ ϕ_{31} parameter. The dashed orange line shows the RMS between the two different ϕ_{31} values, or the typical scatter around the ideal 1-1 relation. The datapoints shown correspond to the subset of the WISE dataset with both $W1$ and $W2$ ϕ_{31} measurements available.

Figure 2.4 shows that the $W1$ and $W2$ bands produce indistinguishable values of ϕ_{31} due to the light curves in these bands being nearly identical. This is demonstrated quantitatively by Equation 2.4, which shows that the best-fit slope between $\phi_{31(W1)}$ and $\phi_{31(W2)}$ is within the errors close to unity, with a dispersion of 0.30.

$$\phi_{31(W2)} = (1.011 \pm 0.023) \cdot \phi_{31(W1)} + (0.066 \pm 0.043) \tag{2.4}$$

We take advantage of this strong correlation by averaging, whenever possible, the ϕ_{31} parameters calculated for the two bands, falling back on $\phi_{31(W1)}$ or $\phi_{31(W2)}$ when only one is available. This essentially doubles the signal of the WISE light curves by combining the data of independent measurements taken at different wavelengths.

2.4.4 Period-Fourier-[Fe/H] Fitting

The metallicity of each star in either our ASAS-SN or WISE datasets can be effectively represented by a plane in the period, ϕ_{31}, and [Fe/H] space, as is demonstrated in Appendix 2.9 by performing Principal Component Analysis (PCA) on each dataset. To determine the orientation of this plane, we adopted the Orthogonal Distance Regression (ODR) routine part of the SciPy package[6], which utilizes a modified trust-region Levenberg-Marquardt-type algorithm (Boggs and Rogers, 1990) to estimate the best fitting parameters. We chose ODR because it can be used similarly to PCA with both techniques minimizing the perpendicular distance to the fit with no differentiation between dependent and independent variables. This allows ODR to produce an optimal fit despite the correlation between variables we found in Appendix 2.9 (especially the well-known correlation between period and metallicity, see e.g. F19). These correlations, in the case of ordinary least-squares or similar fitting algorithms, would result in a trend of the fitted metallicity residuals with respect to the other variables.

We performed the ODR fit on both our ASAS-SN and WISE calibration sets using the equation:

$$[\text{Fe/H}] = a + b \cdot (P - P_0) + c \cdot (\phi_{31} - \phi_{31_0}) \tag{2.5}$$

where P_0 and ϕ_{31_0} are pivot offsets necessary to add an extra element of robustness in the fitting procedure and reduce the fitting parameter uncertainties. We chose the pivot offsets to be near the mean period and ϕ_{31} value of each dataset, equal to $P_0 = 0.58$ days for both datasets, and $\phi_{31_0} = 5.25$ and 1.90 radians for ASAS-SN and WISE, respectively. To ensure an accurate fit, two rounds of fitting were performed with an intermediate 4σ clipping between the fitted and calibration [Fe/H] (removing $\lesssim 1\%$ of the stars in each calibration dataset).

Our best fit period-ϕ_{31}-[Fe/H] relation based on the ASAS-SN V-band light curves is:

$$[\text{Fe/H}] = (-1.22 \pm 0.01) + (-7.60 \pm 0.24) \cdot (P - 0.58) + (1.42 \pm 0.05) \cdot (\phi_{31} - 5.25) \ ; \ \text{RMS} = 0.41 \tag{2.6}$$

---

[6] https://docs.scipy.org/doc/scipy/reference/odr.html

where, due to the 2π periodic ambiguity in the ϕ_{31} coefficient, some ϕ_{31} values required adding 2π to their phase in order to lie closer to the mean ϕ_{31} value, as suggested by JK96.

The period-ϕ_{31}-[Fe/H] relation, based on the average ϕ_{31} parameters of the WISE light curves (averaged when possible between the $W1$ and $W2$ bands, as described in Section 2.4.3), is instead:

$$[\text{Fe/H}] = (-1.47\pm0.02)+(-8.33\pm0.34)\cdot(P-0.58)+(0.92\pm0.05)\cdot(\phi_{31}-1.90) \;\; ; \;\; \text{RMS} = 0.50 \;\; (2.7)$$

Parameter uncertainties have been checked with bootstrap re-sampling and are consistent with those via ODR. The errors from bootstrap re-sampling are those listed in the above relations. The Root Mean Square (RMS) of the two relations (0.41 and 0.50 dex for the ASAS-SN and WISE samples, respectively) are similar, showing that indeed accurate photometric metallicities can be obtained from infrared light curves. The RMS values are also comparable to the dispersion that we found with a non-parametric regression scheme, based on the k-NN method, of the same data (0.33 and 0.40 dex respectively, see Appendix 2.10). This shows that our ODR fits provide an accurate description of the dependence of [Fe/H] from period and ϕ_{31}, with uncertainty only slightly larger than the data's intrinsic scatter. Table 2.3 shows the derived photometric properties for both the V-band and mid-IR (WISE) calibration datasets, including the period, ϕ_{31} value, and photometric metallicity in each band. Following the light curve fitting, quality control process, and the final plane fit described above, we were left with 1980 variables with good quality ASAS-SN light curves, and 1083 variables with good WISE (in at least one of the two $W1$ and $W2$ bands) light curves.

Figures 2.5 and 2.6 (for the ASAS-SN and WISE samples, respectively) demonstrate in graphical form the ability of our fits to provide photometric metallicities in agreement with the spectroscopic values in the HR+ΔS calibration sample. The top left panel shows the distribution of the sources in the ϕ_{31} vs. period plane, superimposed with the relations in Equation 2.6 and 2.7 calculated for fixed values of [Fe/H]. Both data and fit lines are color-binned by metallicity. Note the good agreement between the distribution of the spectroscopic metallicities of individual sources with the locus corresponding to the same metallicity bin defined by the spectroscopic

Table 2.3   Derived photometric properties of RRab sample: This table is published in its entirety in the machine-readable format. A portion is shown here for guidance regarding its form and content.

Gaia ID (DR3)	Period[7] (days)	ϕ_{31} (V) (radians)	$[Fe/H]_V$ (dex)	ϕ_{31} (W) (radians)	$[Fe/H]_W$ (dex)
507222753405440	0.6088826			1.65842	−1.93
4235220006525184	0.4664141			1.18099	−1.18
5355313117668352	0.4945746	4.90759	−1.06		
14233869512030080	0.6670034	4.96473	−2.29	1.62441	−2.44
15489408711727488	0.6511669	5.19695	−1.84	1.80280	−2.15
15891245851805568	0.5738989	5.04774	−1.46	1.51379	−1.77
18268974106572416	0.5541744	4.75948	−1.72	1.26200	−1.84
19606736160298112	0.5465583	5.01736	−1.30		
20161096179157248	0.6042955			2.31260	−1.29
20357148550791168	0.4853687	4.31030	−1.84		

relations. The histogram in the bottom left panel shows how the distribution of the photometric [Fe/H] from our fits closely reproduces the metallicity distribution, from spectroscopy, of the calibration sample. The two plots on the right instead show the distribution of the residuals between the photometric and spectroscopic metallicities: the top panel confirms that our choice of fitting the data with an ODR method indeed avoids residual trends, while the bottom panel shows a close-to-Gaussian distribution of the residuals.

---

[7]When both V-band and mid-IR (WISE) data is present, the period included was calculated from ASAS-SN (V-band) data as the period is usually more accurate due to the higher amplitude and steeper light curve.
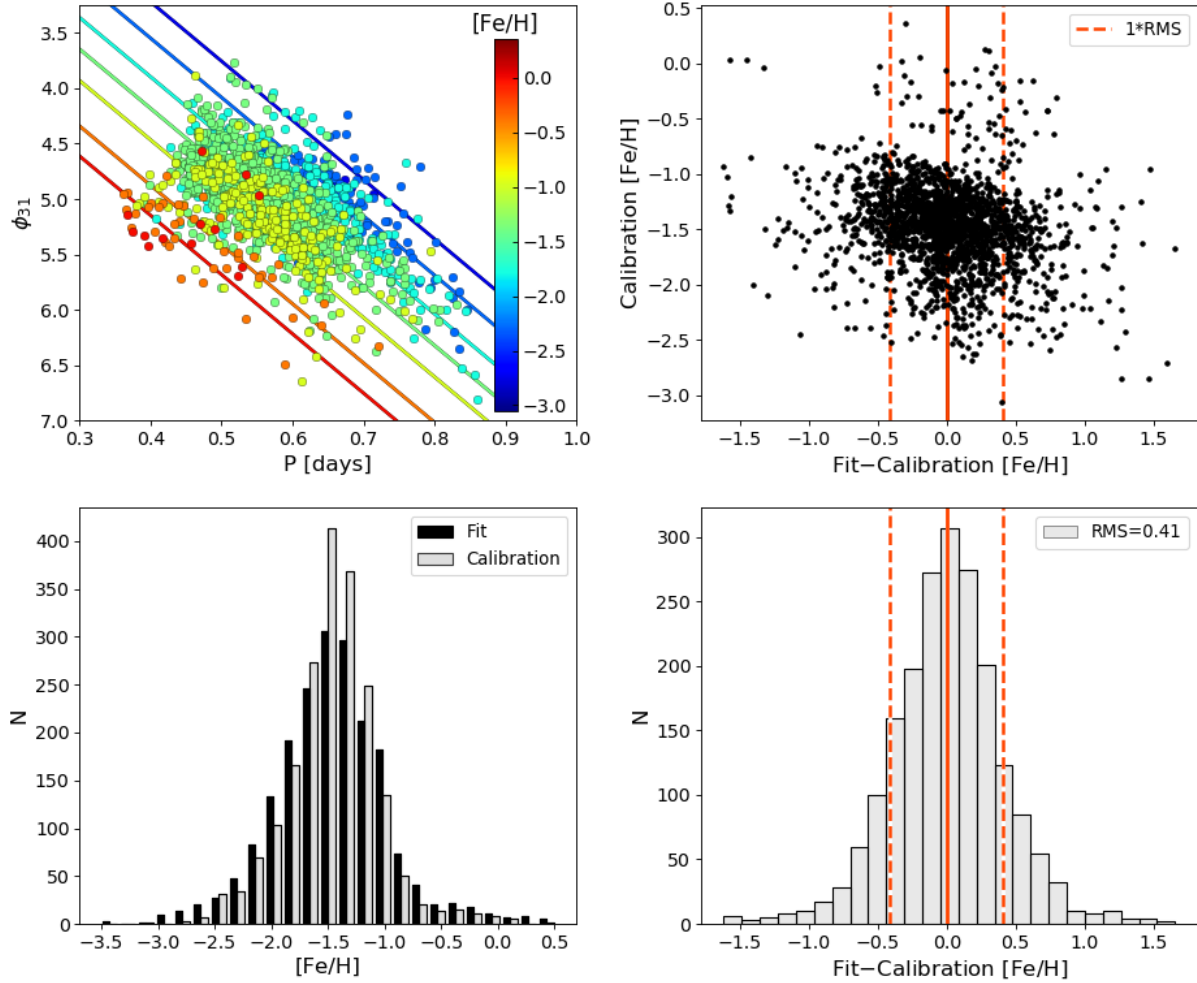
Figure 2.5   ASAS-SN V-band period-ϕ_{31}-[Fe/H] fit. *Top Left*: period versus ϕ_{31} plane with stars binned and color-coded based on their spectroscopic metallicity. Solid lines represent the best fit relation calculated for the average metallicity in each bin, from metal-rich in the bottom left (red) to metal-poor in the upper right (blue). *Bottom Left*: comparison of the spectroscopic calibration [Fe/H] with the best fit photometric metallicity. *Top Right*: spectroscopic [Fe/H] plotted as a function of the residuals of the photometric and spectroscopic metallicity. The dashed vertical lines represent the RMS error between the photometric and spectroscopic metallicity. *Bottom Right*: histogram of the difference between the photometric and spectroscopic [Fe/H]. Again, the vertical lines show the RMS dispersion of the data.

Figure 2.6   WISE W-band period-ϕ_{31}-[Fe/H] fit. *Top Left*: period versus ϕ_{31} plane with stars binned and color-coded based on their spectroscopic metallicity. Solid lines represent the best fit relation calculated for the average metallicity in each bin, from metal-rich in the bottom left (red) to metal-poor in the upper right (blue). *Bottom Left*: comparison of the spectroscopic calibration [Fe/H] with the best fit photometric metallicity. *Top Right*: spectroscopic [Fe/H] plotted as a function of the residuals of the photometric and spectroscopic metallicity. The dashed vertical lines represent the RMS error between the photometric and spectroscopic metallicity. *Bottom Right*: histogram of the difference between the photometric and spectroscopic [Fe/H]. Again, the vertical lines show the RMS dispersion of the data.

2.5   Discussion

2.5.1   Optical vs. Infrared Relations

The analysis in Section 2.4.4 shows that optical and infrared period-ϕ_{31}-[Fe/H] relations provide photometric metallicities of comparable accuracy. However, we still need to test if Equation 2.6 and 2.7 provide consistent values of [Fe/H] for individual stars. Figure 2.7 shows that this is indeed the case: we find an excellent agreement between the photometric metallicities derived at the two wavelengths ranges for the joint sample on a per-star basis. The dispersion between the two datasets, of 0.44 dex, is comparable with the RMS of the individual fits as well as with the dispersion of the residuals from the k-NN method in Appendix 2.10.
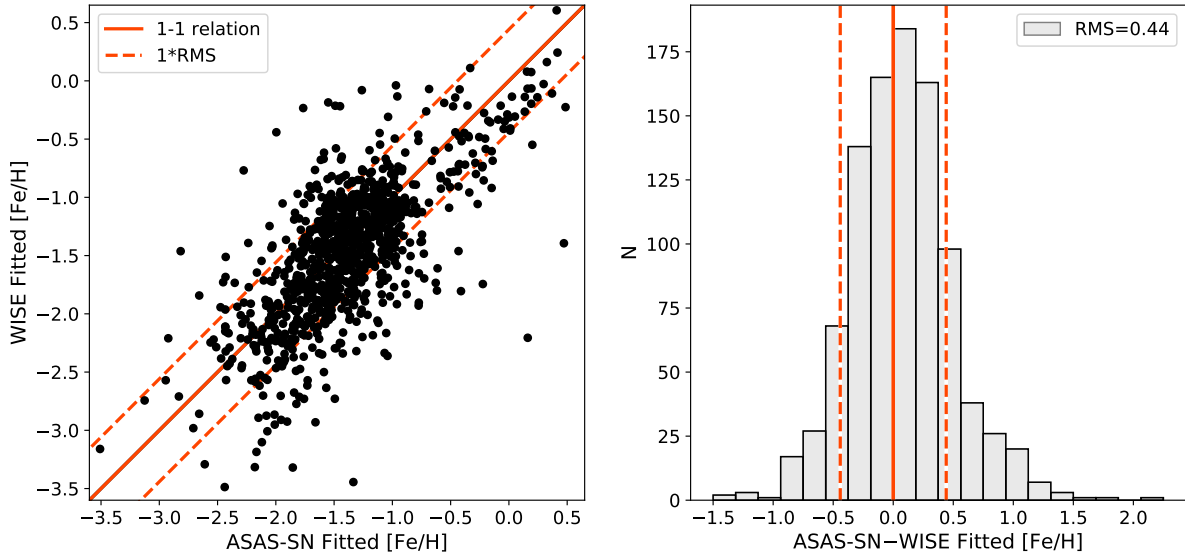
Figure 2.7   Comparison of the photometric [Fe/H] derived from ASAS-SN and WISE samples. The left panel directly compares the photometric metallicities derived for each star in the joint sample, while the right panel shows a histogram of the differences between these photometric metallicities. The dashed lines show the RMS between the two datasets [Fe/H].

This tight correlation between optical and infrared photometric metallicities, with no apparent trends, led us to consider whether averaging the two photometric metallicities would yield a value significantly closer to the spectroscopic metallicity from the HR+ΔS sample. Furthermore, besides the obvious advantage of increasing the statistics of the photometric measurements, by combining optical and infrared data we can probe the effects that different aspects of stellar atmospheres have on the RRL light curves acquired in these two separate wavelength ranges (the optical light curves are dominated by temperature, while infrared emission follows more closely radius variations).
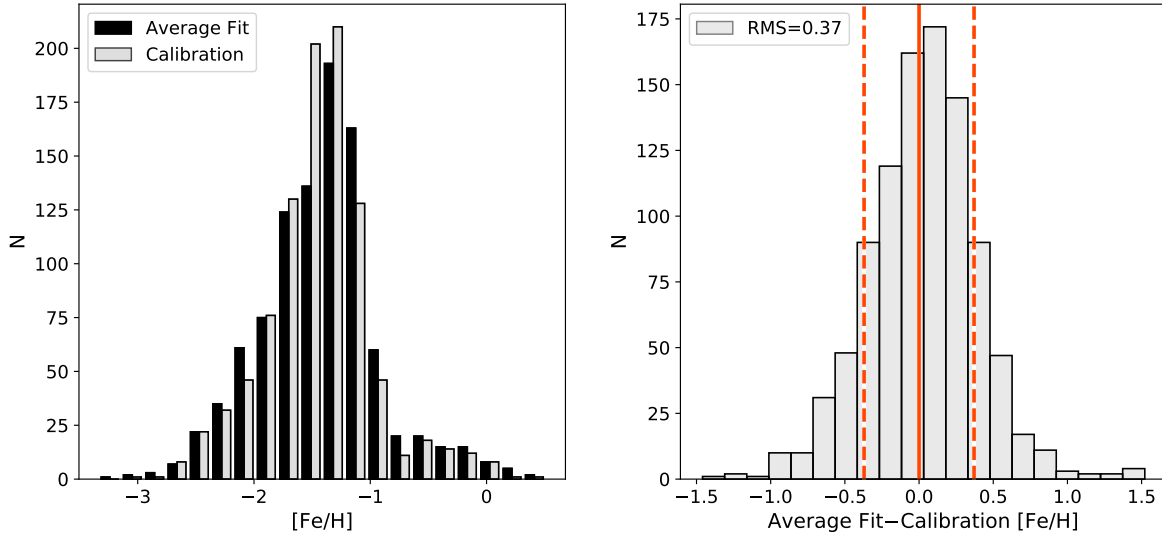
Figure 2.8   *Left*: Comparison of the distribution of the spectroscopic calibration metallicity (grey histogram) and the fitted photometric metallicity averaged from both the ASAS-SN and WISE $P - \phi_{31} - [Fe/H]$ fit (black histogram). *Right*: Histogram of the difference between the average photometric and spectroscopic metallicities. The vertical orange lines represent the RMS dispersion between the two metallicity values.

Based on these arguments, we average together the photometric metallicities derived from the optical and infrared relationships for each star in the joint sample. Figure 2.8 shows that the average photometric metallicity (black histogram in left panel) closely mirrors the spectroscopic

metallicity values from the HR+ΔS calibration sample (grey histogram) for the entire metallicity range. The right panel shows that the residuals between the average photometric [Fe/H] and the spectroscopic metallicities fall fairly symmetrically around zero.

The RMS dispersion between the two sets of values is $\sim$0.37 dex: smaller than the individual error in the optical ($\sim$0.41 dex) or infrared ($\sim$0.50 dex) sample alone. This RMS value is near the dispersion we found with the k-NN method in Appendix 2.10 (0.33 and 0.40 dex for the ASAS-SN and WISE datasets, respectively), which shows that combining these datasets allows one to approach the local scatter in the individual datasets.

2.5.2 Comparison with Globular Clusters Metallicity

In order to test the V-band relation obtained in Section 2.4.3 on an independent sample, we selected a list of eight Galactic GCs homogeneously spread between [Fe/H] $= -1.1$ and -2.3 dex. The selected GCs are described in Section 2.3.4 and listed in Table 2.2. For each cluster, we chose the RRab stars with the best sampled light curves in the V-band, avoiding those RRab stars that suffer the Blazhko effect because of the modulation of the amplitude and the shape of their light curves. A Fourier decomposition was performed on each light curve to obtain their ϕ_{31} parameter. The period-ϕ_{31}-[Fe/H] relation (Equation 2.6) was then applied to estimate the metallicity of each cluster star.

Figure 2.9 shows the spectroscopic [Fe/H] versus the mean photometric [Fe/H] values calculated for each GC with our relation. For consistency with the field RRLs described in Section 2.3.1, the spectroscopic metallicities of these GCs (second column in Table 2.2) from C09 were converted into the scale of this paper with the addition of an offset of 0.08 dex, as noted in C21 and described in Section 2.3.1. The error bars correspond to the spectroscopic and photometric metallicity uncertainties. The former comes from Carretta et al. (2009), while the latter was assessed as the standard error of the mean for star photometric metallicities in each cluster. The good performance obtained using the period-ϕ_{31}-[Fe/H] relation derived in this work is clearly noticeable in Figure 2.9. There are no signals of possible systematic effects, and the
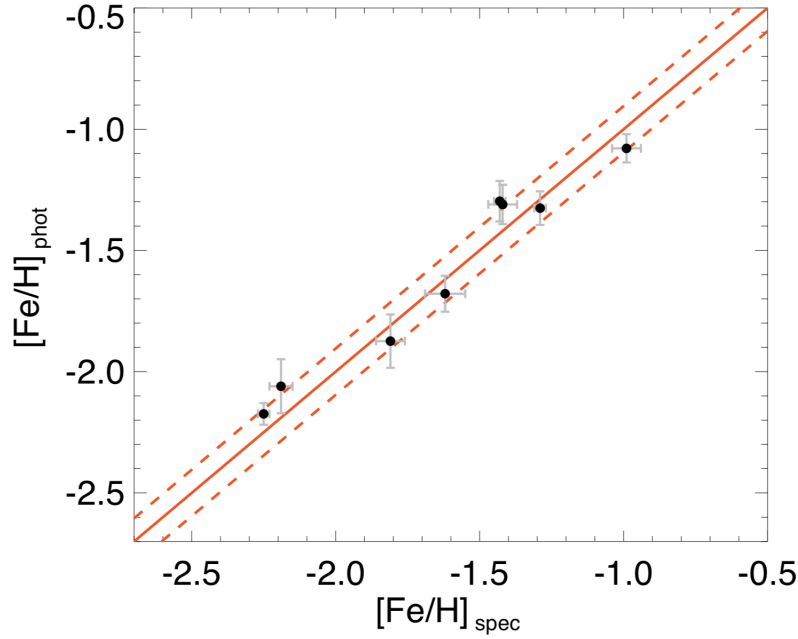
Figure 2.9   [Fe/H]$_{\text{spec}}$ versus [Fe/H]$_{\text{phot}}$ obtained by using Equation 2.6 on a sample of globular clusters. The solid orange line is the 1-1 relation, while the dashed orange lines show the standard deviation (±0.09 dex). Error bars correspond to the uncertainties in spectroscopic metallicity and the statistical error in the photometric metallicity.

predicted [Fe/H] using the period-ϕ_{31}-[Fe/H] relation obtained in this work is within ±0.09 dex of the spectroscopic [Fe/H]. In fact, this accuracy is similar to the metallicity uncertainties measured from the high-resolution spectroscopy on individual stars.

2.5.3   Comparison with Other Relations

In this section, we compare our optical period-ϕ_{31}-[Fe/H] relation (Equation 2.6) with previous relations found in the literature for similar wavelength ranges. In particular, we focus on the relations found in JK96, N13, MV16, and IB20. Note that a similar comparison for our mid-infrared relation (Equation 2.7) is not possible, since we could not find any previous work studying the relation between metallicity and Fourier parameters at wavelengths longer than the I-band (Smolec, 2005). The results are shown in Figure 2.10, which plots the [Fe/H] abundances
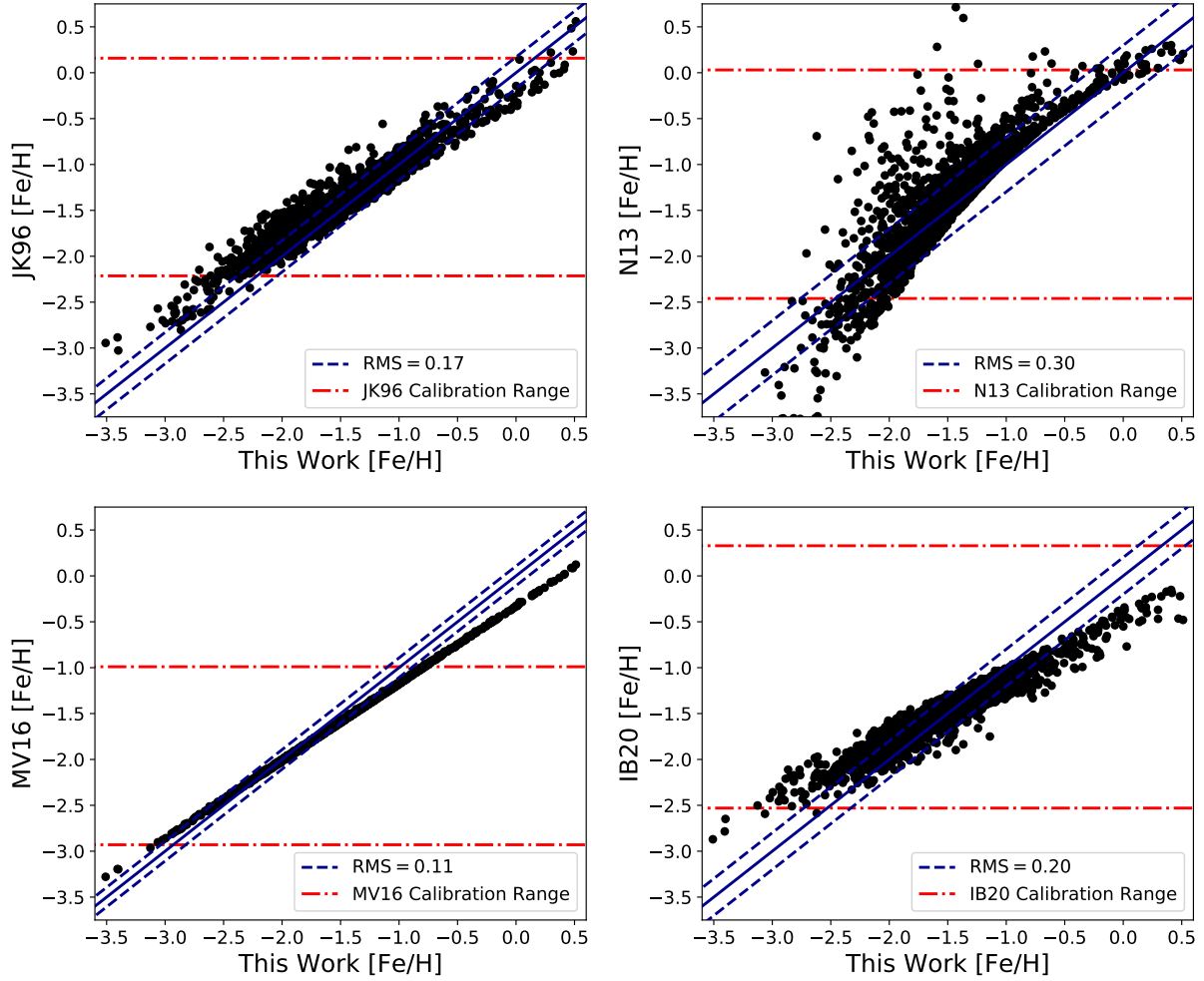
Figure 2.10 Comparison of the [Fe/H] derived with our V-band $P - \phi_{31} - $[Fe/H] relation versus that derived using the relationships of JK96 (top left), N13 (top right), MV16 (bottom left), and IB20 (bottom right), applied to the period and ϕ_{31} values derived in the ASAS-SN calibration dataset. The range of calibration metallicities used in each work to derive their respective relations is noted in each panel with the two red dash-dotted lines. The blue dashed lines around the 1:1 secant (solid line) represent the RMS dispersion between this works and the literature [Fe/H] abundance for the stars within the red dash-dotted calibration range. Note that in the top right panel, outside the calibration region of N13, the quadratic trend deviates significantly from this work for low metallicities (beyond the bounds of this panel).

calculated with the periods and ϕ_{31} parameters from the ASAS-SN sample, using our relation vs. the relations published in the literature.

The top left panel shows the comparison with the formula found in JK96 (their Equation 3). Their relation was derived using a total of 81 field RRab with V-band photometry from heterogeneous observations at various sites. Due to lack of phase coverage or excessive noise, a direct Fourier fit in JK96 was often not available, and individual polynomial fits or small parabolas were fit to light curve segments as needed. Since JK96 adopted metallicities based on the high-dispersion spectroscopy scale of Jurcsik (1995), for consistency, we first converted the metallicities derived with their relation to the C09 scale, using the relation from Kapakos et al. (2011): $[\mathrm{Fe/H}]_{\mathrm{C09}} = 1.001[\mathrm{Fe/H}]_{\mathrm{JK96}} - 0.112$. A scale offset of 0.08 was then added to transform the C09 scale to that adopted by this work's HR+ΔS calibration sample (see Section 2.3.1). We found agreement within the calibration range of JK96 (red horizontal lines), with an RMS value of 0.17 dex, which is smaller than the nominal uncertainty in the calculated [Fe/H] abundances, and only a mildly apparent trend.

N13 introduced a quadratic period-ϕ_{31}-[Fe/H] relation (their Equation 2), calibrated using stars observed in the Kepler photometric band during the first 970 days of the Kepler mission. Since Kepler, during its nominal mission, surveyed the same region of the sky nearly continuously, each star resulted in having $\sim$350,000 data points spread over $\sim$2,500 pulsation cycles, yielding the best sampled light curves (and Fourier decomposition) currently available for any sample of RRLs. However, due to the fixed field of view and shallow depth of Kepler's field, their calibration dataset only had a total of 26 RRab stars with accurate metallicity measurements, nine of which were Blazhko. In order to use the relation of N13, derived in the Kepler photometric system (Kp), with our data, we had to convert the V-band ϕ_{31} value to the Kepler system by adding the systematic offset derived by Nemec et al. (2011):

$$\phi_{31}(V) = \phi_{31}(Kp) - (0.151 \pm 0.026) \tag{2.8}$$

Furthermore, we converted the [Fe/H] abundances provided by N13 from their adopted metallicity scale C09 to this work scale, using the previously noted scale offset of 0.08 dex. The results are presented in the top right panel of Figure 2.10 and show an excellent agreement for higher metallicities in the N13 calibration range ($-1.5 \lesssim$ [Fe/H] ≤ 0.03 dex). For lower metallicities, however, the two relations rapidly diverge (RMS $\simeq 0.30$ dex if calculated over their entire calibration range), caused by the higher-order term in N13, and possibly due to the scarcity of calibrators in their samples for low [Fe/H] (they only have one RRL with [Fe/H] $\lesssim -2.0$ dex.

Next, we compare our relationship with the one derived by MV16 (end of Section 2 in their paper), calibrated using a sample of 381 RRLs in globular clusters binned by period, with the addition of 8 field RRLs chosen to extend the metallicity range of the sample. The C09 metallicity scale used by MV16 has also been converted to that of this work to allow a comparison with our sample. The result is presented in the bottom-right panel of Figure 2.10, showing a general agreement with our fit within the calibration range of MV16, albeit with a small slope with respect to our relation. Note that we set the lower limit of the calibration range plotted to [Fe/H] $\simeq -0.99$ since there was a discontinuity in the data beyond which only had two variable stars.

Finally, IB20 introduced a G-band period-ϕ_{31}-[Fe/H] relation (their equation 3), based on Gaia DR2 light curves. The relation was calibrated with a sample of 84 stars with known spectroscopic metallicity. To allow comparison with our metallicities, we had first to convert the V-band ϕ_{31} value of our dataset to the G-band system, using the relation derived by Clementini et al. 2016:

$$\phi_{31}(G) = (0.104 \pm 0.020) + (1.000 \pm 0.008)\phi_{31}(V); \text{ RMS} = 0.055 \tag{2.9}$$

Furthermore, an additional π offset had to be subtracted from ϕ_{31} to set the coefficient on the same scale as IB20. Metallicity abundances from IB20 were on the scale of Zinn and West (1984, ZW84) and were thus converted using the following equation from C09 with a subsequent scale conversion to that of this work: $[\text{Fe/H}]_{\text{C09}} = 1.105[\text{Fe/H}]_{\text{ZW84}} + 0.160$.

The results are shown in the bottom right panel of Figure 2.10 and exhibit a clear trend between the two relations for the entire range of metallicity. It should be noted that although the stars used for the calibration of the IB20 relation range from ($-2.53 \leq$ [Fe/H] ≤ 0.33), the fit lacks a significant number of calibrators at the low and high metallicity ends. In comparison to this work, their relation tends to overestimate the metallicity at the metal-poor end and underestimate the metallicity at the metal-rich end.

2.5.4 Comparison with High-Resolution Spectroscopic Metallicities

To assess the reliability of the period-ϕ_{31}-metallicity relations, both derived in this paper and from literature, in providing [Fe/H] abundances, we compare their predictions with metallicities measured from high-resolution spectroscopy in the HR+ΔS sample. The results are shown in Figure 2.11, plotting the difference between spectroscopic and photometric [Fe/H] abundance for each of the stars in C21 with metallicity from a high-resolution spectrum. The RMS scatter of each relation, calculated with respect to zero residuals over the entire spectroscopic metallicity range, is indicated for each photometric relation.

The figure shows that all relations have similar residuals (RMS $\simeq$ 0.3-0.4 dex). The scatter in our relations (top row), in particular, are consistent with the expected uncertainties of our photometric metallicities. There is marginal evidence for a systematic shift downwards in panels of Figure 2.11 that we attribute to the minor differences between the ΔS and HR metallicities as shown in Figure 9 of C21. All relations from literature show a trend of the residuals with high-resolution spectroscopic metallicity due to their tendency to overestimate [Fe/H] abundances at the low-metallicity range and underestimate high-metallicities, with the exception of N13 that shows a significantly larger scatter (RMS $\simeq$ 0.57 dex). This apparent trend may result from an inadequate sampling of the metal-rich and metal-poor tails or possibly non-LTE effects in each of the calibration datasets' metallicities that are not fully taken into account. More investigation is needed in order to clarify the mechanisms behind this trend. This trend is largest in the IB20, which underestimates the metallicity of all stars with [Fe/H] $\lesssim -2.0$ and overestimates the
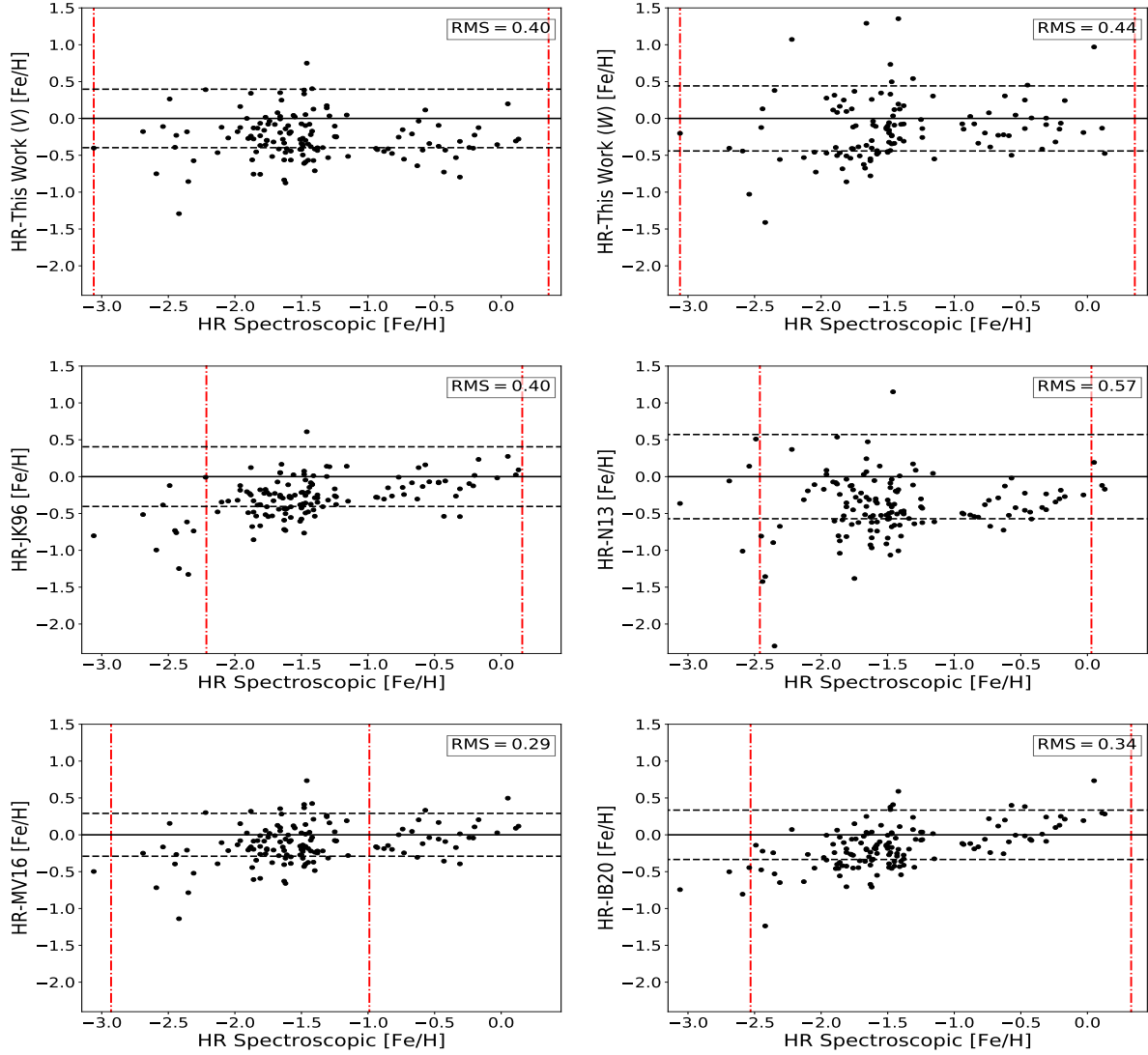
Figure 2.11   Comparison of the difference between the high-resolution (HR) spectroscopic
[Fe/H] and that derived with the photometric relations discussed in Sec-
tion 2.5.3. The black dashed lines around the zero residual solid line represent
the RMS dispersion between the respective work's [Fe/H] abundance and the
spectroscopic metallicities from high-resolution data. The range of calibration
metallicities used in each work to derive their respective relations is noted in
each panel with the two red dash-dotted lines. Note, the mid-infrared com-
parison (top-right panel) can only be shown for a smaller subset of HR stars
for which the WISE light curve is available.

metallicity for [Fe/H] $\gtrsim 0.7$ dex, which was already partially noted by IB20 within their calibration range.

It is worth noting that the RMS values presented in Figure 2.11 are generally larger than those quoted inside these respective works of literature. The RMS values quoted in other papers are a measure of their fit's dispersion with respect to their calibration dataset and should not be construed as a measurement of accuracy between two relations. A comparison between works needs to be made on an identical validation dataset (as was done in this section). We attribute the larger dispersion in our relations as denoting a more realistic representation of the intrinsic scatter found in the period-ϕ_{31}-[Fe/H] relation, which is not apparent in smaller calibration samples, usually covering a smaller metallicity range. Our calibration sample is 76$\times$ larger than N13 (26 RRab) and 24$\times$ larger than JK96 (81 RRab). We could decrease the dispersion of this works' relations by artificially cutting the tails of the metallicity distribution (very metal-poor/metal-rich). However, this approach would introduce severe systematic drifts in the metallicity estimates — i.e. the same problem affecting other current calibrations — which is what we have strived to resolve in this work.

2.6   Conclusions

In this work, we have calibrated a new relation to provide RRab photometric metallicities based on the ϕ_{31} Fourier parameter of optical and, for the first time, infrared light curves. Our relations are based on a set of homogeneous spectroscopic [Fe/H] abundances derived by using the ΔS method of C21 and validated with a sample of [Fe/H] metallicities from high-resolution spectra. The photometric time series of our calibration stars were extracted from the ASAS-SN (V band) and WISE (NEOWISE extension, $W1$ and $W2$ bands) surveys, providing well-sampled light curves that allow for reliable Fourier expansions and accurate determination of the RRL pulsation periods (better than 10^{-6} days).

Comparisons with other optical photometric metallicity relations available in the literature show that our relation provides reliable [Fe/H] abundances without noticeable trends over the

broadest metallicity range (from [Fe/H] $\lesssim -3$ to solar). We have also shown that there is an intrinsic scatter in the period-ϕ_{31}-[Fe/H] plane that becomes apparent with large calibration datasets covering a broad metallicity range. Our V-band relation (Equation 2.6) is consistent within $\simeq 0.40$ dex with [Fe/H] abundances from high-resolution spectroscopy over the entire metallicity range. This relation allows for a quick determination of reliable metallicities for large photometric samples of RRLs that will be observed in upcoming optical wide-area time-domain surveys. It offers a good compromise between efficiency and accuracy, with uncertainties only 2 or 3 times larger than metallicities from labor-intensive line-fitting high-resolution spectroscopy. Our relation can also be applied to existing datasets of well-sampled optical light curves obtained by Kepler and Gaia, by converting the ϕ_{31} parameters from their respective K_P and G bands, using transformations available in the literature. Finally, we show that our V-band relation, applied to ensembles of RRLs in Galactic globular clusters, provide estimates of the clusters' metallicity with accuracy comparable to high-resolution spectroscopy measurements (within ± 0.09 dex).

In addition, we have obtained for the first time a mid-infrared period-ϕ_{31}-[Fe/H] relation using WISE W1 and W2 bands (Equation 2.7). Despite having a smaller number of RRLs to derive this relation, the RMS obtained was similar to that we obtained in the optical. While our infrared relations are slightly less accurate (RMS $\simeq 0.50$ dex), they can still be used to obtain statistically representative metallicities for large ensembles of RRLs. This will be crucial with the advent of sensitive telescopes in the mid-infrared (such as JWST), which will allow observations of extragalactic RRLs across the Local Group of galaxies, for which spectral observations will not be feasible. Further new large optical (WEAVE[8], 4MOST[9]) and near-infrared (MOONS[10] at VLT) spectroscopic surveys will provide the unique opportunity to improve the current calibration of the period-Fourier-metallicity relations using both medium and high-resolution spectra. However, by combining optical and infrared photometric metallicities, we have shown it is possible to

---

[8]https://ingconfluence.ing.iac.es:8444/confluence//display/WEAV/The+WEAVE+Project
[9]https://www.4most.eu/cms/facility/overview/
[10]https://www.eso.org/sci/facilities/develop/instruments/MOONS.html

further improve the measurements' reliability. will allow observations of extragalactic RRLs across theLocal Group of galaxies, for which spectral observations will not be feasible

Having a larger sample size of RRLs with known metallicity will enable a more in-depth study of the metallicity distributions of RRLs (tracers of older stellar populations) in our local neighborhood.

2.7 References

Akeson, R., Armus, L., Bachelet, E. et al (2019). The Wide Field Infrared Survey Telescope: 100 Hubbles for the 2020s. *arXiv e-prints*, page arXiv:1902.05569.

Ball, N.M., Brunner, R.J., Myers, A.D. et al (2007). Robust Machine Learning Applied to Astronomical Data Sets. II. Quantifying Photometric Redshifts for Quasars Using Instance-based Learning. *The Astrophysical Journal*, 663(2):774–780.

Blažko, S. (1907). Mitteilung über veränderliche Sterne. *Astronomische Nachrichten*, 175:325.

Boggs, P. and Rogers, J. (1990). Orthogonal distance regression. *Contemporary Mathematics*, 112:183–194.

Caputo, F. (1998). Evolution of Population II stars. *Astronomy and Astrophysics Reviews*, 9(1-2):33–61.

Carretta, E., Bragaglia, A., Gratton, R. et al (2009). Intrinsic iron spread and a new metallicity scale for globular clusters. *Astronomy and Astrophysics*, 508(2):695–706.

Catelan, M. and Smith, H.A. (2015). *Pulsating Stars*.

Chadid, M., Sneden, C. and Preston, G.W. (2017). Spectroscopic Comparison of Metal-rich RRab Stars of the Galactic Field with their Metal-poor Counterparts. *The Astrophysical Journal*, 835(2):187.

Clement, C.M., Muzzin, A., Dufton, Q. et al (2001). Variable Stars in Galactic Globular Clusters. *Astronomical Journal*, 122(5):2587–2599.

Clementini, G., Carretta, E., Gratton, R. et al (1995). The Composition of HB Stars: RR Lyrae Variables. *Astronomical Journal*, 110:2319.

Clementini, G., Ripepi, V., Leccia, S. et al (2016). Gaia Data Release 1. The Cepheid and RR Lyrae star pipeline and its application to the south ecliptic pole region. *Astronomy and Astrophysics*, 595:A133.

Clementini, G., Ripepi, V., Molinaro, R. et al (2019). Gaia Data Release 2. Specific characterisation and validation of all-sky Cepheids and RR Lyrae stars. *Astronomy and Astrophysics*, 622:A60.

Collaboration, G., Brown, A.G.A., Vallenari, A. et al (2020). Gaia early data release 3: Summary of the contents and survey properties.

Cover, T. and Hart, P. (1967). Nearest neighbor pattern classification. *IEEE Transactions on Information Theory*, 13(1):21–27.

Crestani, J., Fabrizio, M., Braga, V.F. et al (2020). On the Use of Field RR Lyrae as Galactic Probes. II. A new ΔS calibration to estimate their metallicity. *arXiv e-prints*, page arXiv:2012.02284.

Dambis, A.K., Berdnikov, L.N., Kniazev, A.Y. et al (2013). RR Lyrae variables: visual and infrared luminosities, intrinsic colours and kinematics. *Monthly Notices of the Royal Astronomical Society*, 435(4):3206–3220.

Deng, L.C., Newberg, H.J., Liu, C. et al (2012). LAMOST Experiment for Galactic Understanding and Exploration (LEGUE) — The survey's science plan. *Research in Astronomy and Astrophysics*, 12(7):735–754.

Fabrizio, M., Bono, G., Braga, V.F. et al (2019). On the Use of Field RR Lyrae as Galactic Probes. I. The Oosterhoff Dichotomy Based on Fundamental Variables. *The Astrophysical Journal*, 882(2):169.

Fernley, J. and Barnes, T.G. (1996). Metal abundances of field RR Lyraes. *Astronomy and Astrophysics*, 312:957–965.

For, B.Q., Sneden, C. and Preston, G.W. (2011). The Chemical Compositions of Variable Field Horizontal-branch Stars: RR Lyrae Stars. *The Astrophysical Journal Supplement Series*, 197(2):29.

Gaia Collaboration, Brown, A.G.A., Vallenari, A. et al (2018). Gaia Data Release 2. Summary of the contents and survey properties. *Astronomy and Astrophysics*, 616:A1.

Gardner, J.P., Mather, J.C., Clampin, M. et al (2006). The James Webb Space Telescope. *Space Science Reviews*, 123(4):485–606.

Gilligan, C.K., Chaboyer, B., Marengo, M. et al (2021). Metallicities from high-resolution spectra of 49 RR Lyrae variables. *Monthly Notices of the Royal Astronomical Society*, 503(4):4719–4733.

Govea, J., Gomez, T., Preston, G.W. et al (2014). The Chemical Compositions of RR Lyrae Type C Variable Stars. *The Astrophysical Journal*, 782(2):59.

Holl, B., Audard, M., Nienartowicz, K. et al (2018). Gaia Data Release 2. Summary of the variability processing and analysis results. *Astronomy and Astrophysics*, 618:A30.

Iorio, G. and Belokurov, V. (2020). Chemo-kinematics of the *Gaia* RR Lyrae: the halo and the disc. *arXiv e-prints*, page arXiv:2008.02280.

Ivezić, Ž., Kahn, S.M., Tyson, J.A. et al (2019). LSST: From Science Drivers to Reference Design and Anticipated Data Products. *The Astrophysical Journal*, 873(2):111.

Jayasinghe, T., Kochanek, C.S., Stanek, K.Z. et al (2018). The ASAS-SN catalogue of variable stars I: The Serendipitous Survey. *Monthly Notices of the Royal Astronomical Society*, 477(3):3145–3163.

Jurcsik, J. (1995). Revision of the [Fe/H] Scales Used for Globular Clusters and RR Lyrae Variables. *Acta Astronomica*, 45:653–660.

Jurcsik, J. and Kovacs, G. (1996). Determination of [Fe/H] from the light curves of RR Lyrae stars. *Astronomy and Astrophysics*, 312:111–120.

Kapakos, E., Hatzidimitriou, D. and Soszyński, I. (2011). RR Lyrae variables in the Small Magellanic Cloud - I. The central region. *Monthly Notices of the Royal Astronomical Society*, 415(2):1366–1380.

Koch, D.G., Borucki, W.J., Basri, G. et al (2010). Kepler Mission Design, Realized Photometric Performance, and Early Science. *The Astrophysical Journal Letters*, 713(2):L79–L86.

Lambert, D.L., Heath, J.E., Lemke, M. et al (1996). The Chemical Composition of Field RR Lyrae Stars. I. Iron and Calcium. *The Astrophysical Journal Supplement Series*, 103:183.

Law, N.M., Kulkarni, S.R., Dekany, R.G. et al (2009). The Palomar Transient Factory: System Overview, Performance, and First Results. *Publications of the ASP*, 121(886):1395.

Liu, G.C., Huang, Y., Zhang, H.W. et al (2020). Probing the Galactic Halo with RR Lyrae Stars. I. The Catalog. *The Astrophysical Journal Supplement Series*, 247(2):68.

Liu, X.W., Yuan, H.B., Huo, Z.Y. et al (2014). LSS-GAC - A LAMOST Spectroscopic Survey of the Galactic Anti-center. In Feltzing, S., Zhao, G., Walton, N.A. et al, editors, *Setting the scene for Gaia and LAMOST*, volume 298 of *IAU Symposium*, pages 310–321.

Lomb, N.R. (1976). Least-Squares Frequency Analysis of Unequally Spaced Data. *Astrophysics and Space Science*, 39(2):447–462.

Magurno, D., Sneden, C., Bono, G. et al (2019). Chemical Compositions of Field and Globular Cluster RR Lyrae Stars. II. ω Centauri. *The Astrophysical Journal*, 881(2):104.

Magurno, D., Sneden, C., Braga, V.F. et al (2018). Chemical Compositions of Field and Globular Cluster RR Lyrae Stars. I. NGC 3201. *The Astrophysical Journal*, 864(1):57.

Mainzer, A., Bauer, J., Grav, T. et al (2011). Preliminary Results from NEOWISE: An Enhancement to the Wide-field Infrared Survey Explorer for Solar System Science. *The Astrophysical Journal*, 731(1):53.

Marconi, M., Coppola, G., Bono, G. et al (2015). On a New Theoretical Framework for RR Lyrae Stars. I. The Metallicity Dependence. *The Astrophysical Journal*, 808(1):50.

Marengo, M. and Sanchez, M.C. (2009). A k-NN Method to Classify Rare Astronomical Sources: Photometric Search of Brown Dwarfs with Spitzer/IRAC. *Astronomical Journal*, 138(1):63–75.

Marrese, P.M., Marinoni, S., Fabrizio, M. et al (2019). Gaia Data Release 2. Cross-match with external catalogues: algorithms and results. *Astronomy and Astrophysics*, 621:A144.

Martínez-Vázquez, C.E., Monelli, M., Bono, G. et al (2016). A new Phi_31-period-metallicity relation for RR Lyrae stars. *Commmunications of the Konkoly Observatory Hungary*, 105:53–56.

Muraveva, T., Delgado, H.E., Clementini, G. et al (2018). RR Lyrae stars as standard candles in the Gaia Data Release 2 Era. *Monthly Notices of the Royal Astronomical Society*, 481(1):1195–1211.

Neeley, J.R., Marengo, M., Bono, G. et al (2017). On a New Theoretical Framework for RR Lyrae Stars. II. Mid-infrared Period-Luminosity-Metallicity Relations. *The Astrophysical Journal*, 841(2):84.

Neeley, J.R., Marengo, M., Bono, G. et al (2015). On the Distance of the Globular Cluster M4 (NGC 6121) Using RR Lyrae Stars. II. Mid-infrared Period-luminosity Relations. *The Astrophysical Journal*, 808(1):11.

Neeley, J.R., Marengo, M., Freedman, W.L. et al (2019). Standard Galactic field RR Lyrae II: a Gaia DR2 calibration of the period-Wesenheit-metallicity relation. *Monthly Notices of the Royal Astronomical Society*, 490(3):4254–4270.

Nemec, J.M., Cohen, J.G., Ripepi, V. et al (2013). Metal Abundances, Radial Velocities, and Other Physical Characteristics for the RR Lyrae Stars in The Kepler Field. *The Astrophysical Journal*, 773(2):181.

Nemec, J.M., Smolec, R., Benkő, J.M. et al (2011). Fourier analysis of non-Blazhko ab-type RR Lyrae stars observed with the Kepler space telescope. *Monthly Notices of the Royal Astronomical Society*, 417(2):1022–1053.

Ngeow, C.C., Yu, P.C., Bellm, E. et al (2016). The Palomar Transient Factory and RR Lyrae: The Metallicity-Light Curve Relation Based on ab-type RR Lyrae in the Kepler Field. *The Astrophysical Journal Supplement Series*, 227(2):30.

Pancino, E., Britavskiy, N., Romano, D. et al (2015). Chemical abundances of solar neighbourhood RR Lyrae stars. *Monthly Notices of the Royal Astronomical Society*, 447(3):2404–2419.

Persson, S.E., Madore, B.F., Krzemiński, W. et al (2004). New Cepheid Period-Luminosity Relations for the Large Magellanic Cloud: 92 Near-Infrared Light Curves. *Astronomical Journal*, 128(5):2239–2264.

Piersimoni, A.M., Bono, G. and Ripepi, V. (2002). BVI Time-Series Data of the Galactic Globular Cluster NGC 3201. I. RR Lyrae Stars. *Astronomical Journal*, 124(3):1528–1554.

Preston, G.W. (1959). A Spectroscopic Study of the RR Lyrae Stars. *The Astrophysical Journal*, 130:507.

Sandage, A. (1990). The Vertical Height of the Horizontal Branch: The Range in the Absolute Magnitudes of RR Lyrae Stars in a Given Globular Cluster. *The Astrophysical Journal*, 350:603.

Scargle, J.D. (1982). Studies in astronomical time series analysis. II. Statistical aspects of spectral analysis of unevenly spaced data. *The Astrophysical Journal*, 263:835–853.

Shappee, B.J., Prieto, J.L., Grupe, D. et al (2014). The Man behind the Curtain: X-Rays Drive the UV through NIR Variability in the 2013 Active Galactic Nucleus Outburst in NGC 2617. *The Astrophysical Journal*, 788(1):48.

Shlens, J. (2014). A tutorial on principal component analysis. *CoRR*, abs/1404.1100.

Simon, N.R. and Lee, A.S. (1981). The structural properties of cepheid light curves. *The Astrophysical Journal*, 248:291–297.

Skarka, M. (2014). Bright Blazhko RRab Lyrae stars observed by ASAS and the SuperWASP surveys. *Astronomy and Astrophysics*, 562:A90.

Smolec, R. (2005). Metallicity Dependence of the Blazhko Effect. *Acta Astronomica*, 55:59–84.

Sneden, C., Preston, G.W., Chadid, M. et al (2017). The RRc stars: Chemical abundances and envelope kinematics. *The Astrophysical Journal*, 848(1):68.

Udalski, A., Szymanski, M., Kaluzny, J. et al (1992). The Optical Gravitational Lensing Experiment. *Acta Astronomica*, 42:253–284.

Walker, A.R. (1989). A Survey for RR Lyrae Variables in Five Small Magellanic Cloud Clusters. *Publications of the ASP*, 101:570.

Wright, E.L., Eisenhardt, P.R.M., Mainzer, A.K. et al (2010). The Wide-field Infrared Survey Explorer (WISE): Mission Description and Initial On-orbit Performance. *Astronomical Journal*, 140(6):1868–1881.

Yanny, B., Rockosi, C., Newberg, H.J. et al (2009). SEGUE: A Spectroscopic Survey of 240,000 Stars with g = 14-20. *Astronomical Journal*, 137(5):4377–4399.

Zinn, R. and West, M.J. (1984). The globular cluster system of the Galaxy. III. Measurements of radial velocity and metallicity for 60 clusters and a compilation of metallicities for 121 clusters. *The Astrophysical Journal Supplement Series*, 55:45–66.

2.8 Appendix A: Fourier Parameters

To visualize if the shape of an infrared RRL light curve retains information about the star's metallicity (as is the case in the optical), we have analyzed several low order Fourier parameters, plotted one against the other, or vs. the period. Figures 2.12 and 2.13 plot individual RRLs, color-coded on their [Fe/H], on the basis of R_{21}, R_{31}, ϕ_{21}, ϕ_{31}, and period for the V and $W1$ bands respectively. In all panels where a Fourier parameter is plotted as a function of period, we can readily see a gradient in the [Fe/H] distribution of the stars.

The stronger separation is apparent in the ϕ_{21} and ϕ_{31} vs. period plots, as already discussed in JK96 for V-band light curves. We found that the same is true in the WISE $W1$ and $W2$ bands. In accordance with previous literature, and based on the observation that the ϕ_{31} parameter provides a tighter relation with period and metallicity at both optical and infrared wavelengths, we have adopted ϕ_{31} as the parameter of choice for the analysis presented in Section 2.4.3.

2.9 Appendix B: Principal Component Analysis

Previous works have successfully determined linear relations between period, ϕ_{31}, and [Fe/H] abundance in RRab stars (except for N13, which preferred a quadratic form for the relation). In the case of uncorrelated variables, coefficients of such relations can be estimated with a simple
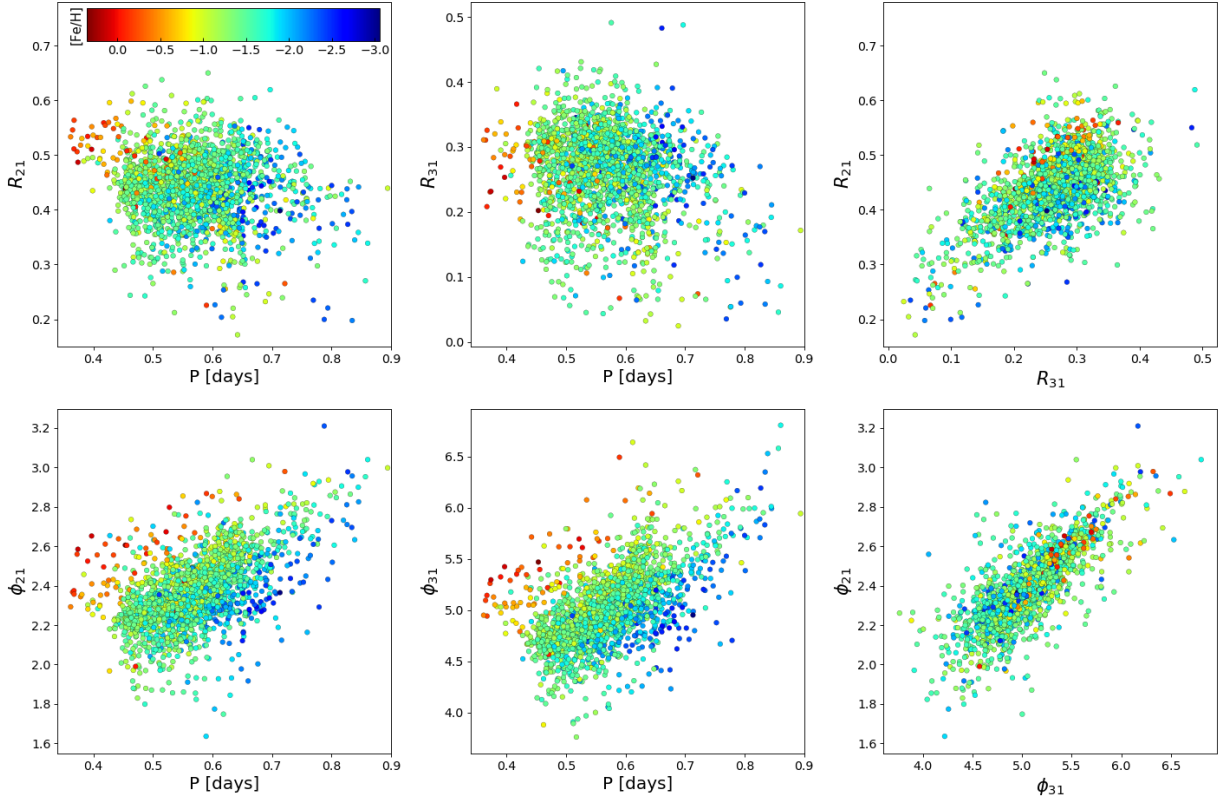
Figure 2.12   ASAS-SN V-band Fourier amplitude parameter ratios (top row) and linear phase parameter combinations (bottom row). RRLs are color-coded based on their spectroscopic calibration metallicities. In the center and left panels, [Fe/H] generally goes from metal-rich in the left (red) to metal-poor in the right (blue).

least-squares fit of the available data. It is well known, however, that there exists a correlation between period and metallicity in RRab stars (see e.g. Equation 14 in F19). To explore this correlation and test if the distribution of metallicity can be effectively described with a plane in period and ϕ_{31} not just at optical wavelengths, but also in the infrared, we have performed a Principal Component Analysis (PCA) to these three dimensions of our data.

PCA (see e.g. Shlens 2014) is a machine learning algorithm often utilized for reducing the number of variables needed to describe a data set. Given a data set with p-different variables, PCA finds a vector (principal component) in this p-dimensional space that can explain the most
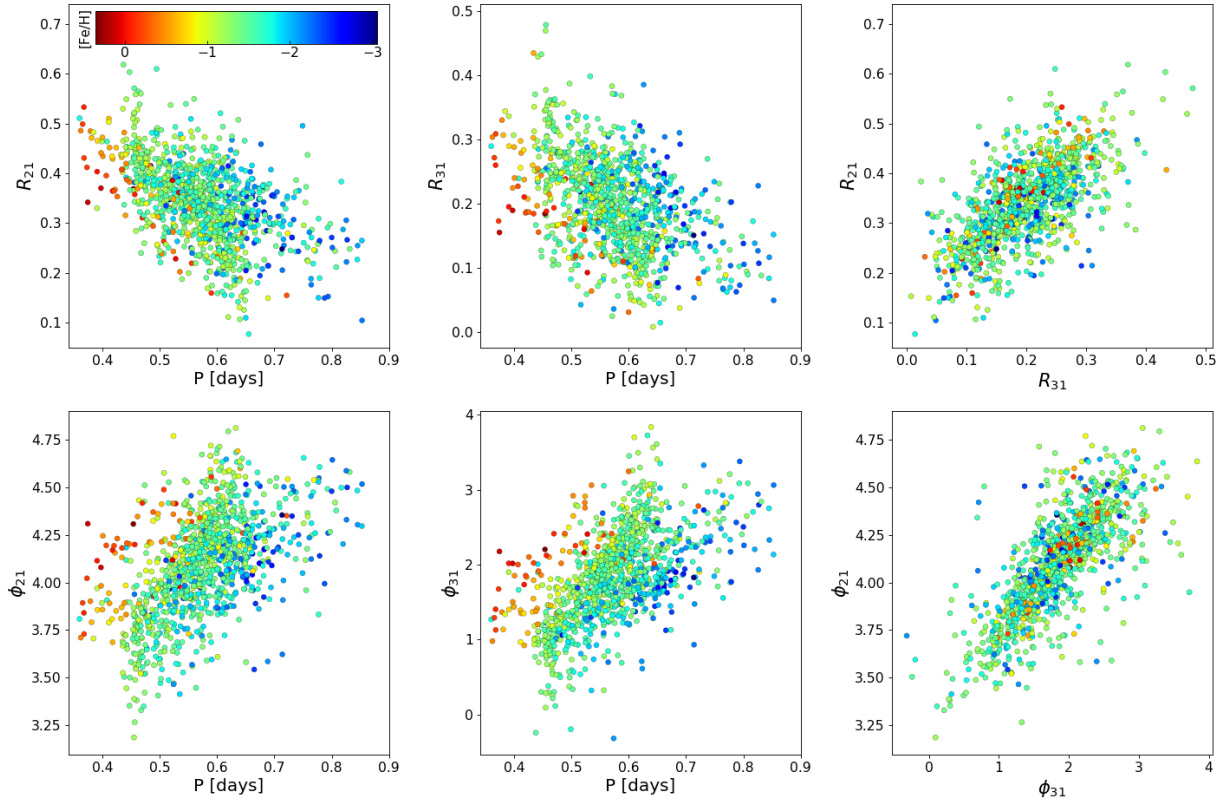
Figure 2.13   Same as Figure 2.12, but for our WISE sample.

variance. Subsequent components are found orthogonal to the prior components in a direction that explains the next highest amount of variance. The percent variance of each of these components quantifies their relative importance. In other words, PCA gives the ability to locate an n-dimensional hyperplane in the p-dimensional variable space ($n < p$, with the smallest possible n) that characterizes the largest amount of variance in the data.

The first step for PCA analysis is to re-normalize each variable (period, ϕ_{31}, and [Fe/H] abundance) in both samples (optical and infrared) so that they have zero mean and unitary variance. This avoids common issues in PCA when different variables range in scale. The

principal components were then found by utilizing the PCA decomposition subroutine from Python's scikit-learn package[11].

Table 2.4   Variance attributed to each Principal Component axis

Principal Component	ASAS-SN	WISE
Axis 1	54.23%	56.51%
Axis 2	38.67%	35.40%
Axis 3	7.10%	8.09%

Table 2.4 shows the PCA variance for each of the ASAS-SN and WISE datasets. It is clear that both samples can be effectively described with just the first two axes, with very little scatter associated to the third component, orthogonal to the plane described by axis 1 and 2. This shows that our data can be efficiently represented by a plane. For both datasets, the first axis is well aligned with the period of the stars, while the second axis is an almost equally weighted combination of ϕ_{31} and [Fe/H]. Based on this result, we feel confident that our dataset can be represented by a linear fit of period, ϕ_{31}, and [Fe/H]. We determine the exact coefficients using the ODR method described in Section 2.4.4. This method still provides rotated axes for the fit, but it allows us to do so while including uncertainties in the fitting variables and data.

2.10   Appendix C: K-Nearest Neighbor Analysis

In this work, we chose to represent the relation between [Fe/H], period, and ϕ_{31} of RRab stars using a linear function of these three variables (see Section 2.4.4). An alternative approach consists of adopting non-parametric techniques that could provide a similar result without assumptions about the functional form of the relation to fit. One such technique is the k-Nearest Neighbors (k-NN) method (Cover and Hart, 1967).

While traditionally used in machine learning classification problems (see e.g. Marengo and Sanchez 2009 for an application in astronomy), the k-NN method also serves as a powerful

---

[11]https://scikit-learn.org/stable/modules/generated/sklearn.decomposition.PCA.html

non-parametric regression technique to estimate the value of a given variable based on the values of the closest neighbors, in a properly defined n-dimensional space. In this work, the location on the period-ϕ_{31} plane is used as a predictor for [Fe/H]. Following Ball et al. (2007), we calculate the Euclidean distance, in the period-ϕ_{31} plane, of each star from every other star in the sample. We then estimate the k-NN metallicity of each star as the [Fe/H] weighted average of its nearest k neighbors, where k is a suitable integer number. The weights used are proportional to the inverse distance in the period-ϕ_{31} plane from the test star so that nearer stars contribute more to the average than the farthest sources.

The number of nearest neighbors k is chosen in order to balance the need of averaging-out the natural scatter in the neighbor's [Fe/H], while at the same time still preserving predictive power at the sparse edges of the samples' distribution in the period-ϕ_{31} plane. Since our goal is to capture the global trend over the entire range of values, and not only the highest density region, we chose $k = 5$ as the optimum number of near neighbors for both our samples.
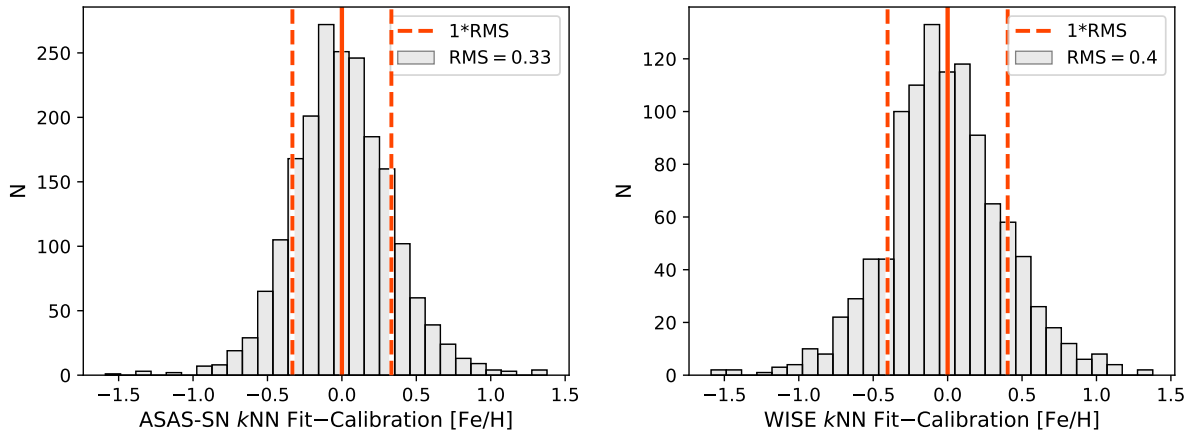
Figure 2.14   Difference in the [Fe/H] predicted by the k-NN method to the metallicity of the calibration sample for ASAS-SN dataset (left) and WISE dataset (right). The root mean square error between the k-NN and calibration metallicity is listed in the top right corners and shown by the vertical dashed lines.

Figure 2.14 shows the difference between the metallicity derived with the k-NN method and the spectroscopic [Fe/H] for our optical and infrared samples. The Root Mean Square (RMS) [Fe/H] error of the residuals is 0.33 dex and 0.40 dex for the ASAS-SN and WISE samples, respectively. Since the k-NN method, in contrast to parametric fits, does not rely upon any particular functional form, we can assume that the quoted RMS errors are representative of the best possible overall [Fe/H] uncertainty (averaged over the entire range of metallicity) that a specific fit could achieve with the available data.

CHAPTER 3.   METALLICITY OF GALACTIC RR LYRAE FROM OPTICAL AND INFRARED LIGHT CURVES: II. PERIOD-FOURIER-METALLICITY RELATIONS FOR FIRST OVERTONE RR LYRAE

Authors

Joseph P. Mullen (1), Massimo Marengo (1), Clara E. Martínez-Vázquez (2 and 3), Giuseppe Bono (4 and 5), Vittorio F. Braga (5 and 6), Brian Chaboyer (7), Juliana Crestani (4, 5, and 8), Massimo Dall'Ora (9), Michele Fabrizio (5 and 6), Giuliana Fiorentino (5), Matteo Monelli (10 and 11), Jillian R. Neeley (12), Peter B. Stetson (13), Frédéric Thévenin (14)

Affiliations

((1) Department of Physics and Astronomy, Iowa State University, Ames, IA, USA, (2) Gemini Observatory, NSF's National Optical-Infrared Astronomy Research Laboratory, Hilo, HI, USA, (3) Cerro Tololo Inter-American Observatory, NSF's National Optical-Infrared Astronomy Research Laboratory, La Serena, Chile, (4) Dipartimento di Fisica, Università di Roma Tor Vergata, Roma, Italy, (5) INAF-Osservatorio Astronomico di Roma, Monte Porzio Catone, Italy, (6) Space Science Data Center, Roma, Italy, (7) Department of Physics and Astronomy, Dartmouth College, Hanover, NH, USA, (8) Departamento de Astronomia, Universidade Federal do Rio Grande do Sul, Porto Alegre, Brazil, (9) INAF-Osservatorio Astronomico di Capodimonte, Napoli, Italy, (10) Instituto de Astrofísica de Canarias, La Laguna, Tenerife, Spain, (11) Departmento de Astrofísica, Universidad de La Laguna, La Laguna, Tenerife, Spain, (12) Department of Physics, Florida Atlantic University, Boca Raton, FL, USA, (13) Herzberg Astronomy and Astrophysics, National Research Council, Victoria, BC, Canada, (14) Université de Nice Sophia-antipolis, CNRS, Observatoire de la Côte d'Azur, Laboratoire Lagrange, Nice, France)

3.1 Abstract

We present new period-ϕ_{31}-[Fe/H] relations for first overtone RRL stars (RRc), calibrated over a broad range of metallicities ($-2.5 \lesssim$ [Fe/H] $\lesssim 0.0$) utilizing the largest currently available set of Galactic halo field RRL with homogeneous spectroscopic metallicities. Our relations are defined in the optical (ASAS-SN V-band) and, inaugurally, in the infrared (WISE $W1$ and $W2$ bands). Our V-band relation can reproduce individual RRc spectroscopic metallicities with a dispersion of 0.30 dex over the entire metallicity range of our calibrator sample (an RMS smaller than what we found for other relations in literature including non-linear terms). Our infrared relation has a similar dispersion in the low and intermediate metallicity range ([Fe/H] $\lesssim -0.5$) but tends to underestimate the [Fe/H] abundance around solar metallicity. We tested our relations by measuring both the metallicity of the Sculptor dSph and a sample of Galactic globular clusters, rich in both RRc and RRab stars. The average metallicity we obtain for the combined RRL sample in each cluster is within ± 0.08 dex of their spectroscopic metallicities. The infrared and optical relations presented in this work will enable deriving reliable photometric RRL metallicities in conditions where spectroscopic measurements are not feasible; e.g., in distant galaxies or reddened regions (observed with upcoming Extremely Large Telescopes and the James Webb Space Telescope), or in the large sample of new RRL that will be discovered in large-area time-domain photometric surveys (such as LSST and the Roman space telescope).

3.2 Introduction

RR Lyrae stars (RRL hereafter) are a ubiquitous and widely used tracer of old (age > 10 Gyr, Savino et al. 2020; Walker 1989) stellar populations in the Milky Way (MW) and Local Group (LG) galaxies (see e.g., MW: Matteucci (2021), Carina: Coppola et al. (2015); Sculptor: Martínez-Vázquez et al. (2016b); M31 dwarf satellites: Martínez-Vázquez et al. (2017); Monelli et al. (2017); Isolated LG dwarfs: Bernard et al. (2010, 2009, 2013)). Their relevance has become even more important in the current age of large area photometric time surveys (e.g., ASAS-SN (Jayasinghe et al., 2018; Shappee et al., 2014), Catalina Sky Survey (Drake et al., 2009),

PanSTARRS (Chambers et al., 2016), DES (Abbott et al., 2018), Gaia (Clementini et al., 2016, 2019), TESS (Ricker et al., 2015)), which have significantly increased the number of known RRL variables. An even larger number of these variables is expected to be discovered as the product of upcoming next-generation surveys, such as the Vera C. Rubin Observatory Legacy Survey of Space and Time (LSST, Ivezić et al., 2019) in the optical, and surveys that will be executed for the Nancy Grace Roman telescope (Akeson et al., 2019) at near-infrared wavelength.

The importance of RRL as tracers is related to their role as distance indicators. Period-Wesenheit-Metallicity relations (PWZ) in the optical and Period-Luminosity-Metallicity relations (PLZ) in the infrared (theoretical: Marconi et al. (2015); Neeley et al. (2017) and observational: Dambis et al. (2013); Gilligan et al. (2021); Muraveva et al. (2018); Neeley et al. (2019)) now provide individual RRL distances with an accuracy approaching other traditional stellar standard candles that can be characterized by a Leavitt Law (Leavitt, 1908; Leavitt and Pickering, 1912), such as Cepheids.

In the case of Classical (Population I) Cepheids, the metallicity dependence on luminosity may, in most cases, be ignored (but see e.g., Breuval et al. 2021); however, the much larger spread in metallicity for RRL (Population II stars) requires reliable measurements of their [Fe/H] abundance to provide accurate distances. Having metallicity measurements available can be a challenge since they are traditionally derived with spectroscopic methods, and spectra cannot be expected to be readily available for the large sample of variables being discovered in large-area surveys. This can be due to logistical constraints based upon telescope time or physical limitations for taking spectra such as extreme distances or high extinction in environments that can only be probed photometrically by mid-infrared cameras. A reliable and precise method to extract physical parameters based solely on photometric time series is necessary to keep pace with this expansion.

Simon and Lee (1981) first showed for variable stars that specific physical parameters, such as metallicity, could be directly related to a light curve's shape (characterized through its Fourier decomposition). Jurcsik and Kovacs (1996) quantified this relationship by finding a bi-linear

relation between period and a low order Fourier phase parameter ($\phi_{31} = \phi_3 - 3 \cdot \phi_1$) derived in the optical, for RRLs pulsating in the fundamental mode (also know as RRab). Additional works have analyzed and revised this relation for RRab (Iorio and Belokurov 2020; Martínez-Vázquez et al. 2016; Mullen et al. 2021; Nemec et al. 2013; Ngeow et al. 2016; Smolec 2005) using more modern datasets in a variety of wavelengths. In particular, Mullen et al. 2021 (hereafter Paper I) obtained a new relation in the V-band based on the largest RRab calibration dataset to date. In Paper I, we showed that accurate RRab photometric metallicities could be extended to both lower and higher metallicity regimes than in previous works. Furthermore, for the first time we showed that a photometric metallicity relation for RRab variables could be extended into the mid-infrared. This paper aims to now derive similar relations for RRL pulsating in the first overtone (RRc variables).

The study of RRc variables possesses additional challenges with respect to RRab. An important issue is the sample size, as the number of RRc is only $\sim 1/3$ of all field RRL (the ratio of RRc to the total number of RRL is intimately tied to how [Fe/H] affects horizontal branch morphology; Fabrizio et al. 2021). Furthermore, extracting accurate periods and Fourier parameters for RRc often takes an extra layer of scrutiny stemming from their inherent smaller amplitudes and quasi-sinusoidal light curves, when compared to the characteristic high-amplitude saw-toothed shape RRab which are more strongly dependent on atmospheric abundances. Due in part to these issues, it was not until Morgan et al. (2007) (hereafter M07) that it was shown that similar period-ϕ_{31}-[Fe/H] equations could be made for RRc in the V-band. Further work by Nemec et al. (2013) (hereafter N13), Morgan (2014) (hereafter M14), and Iorio and Belokurov (2020) (hereafter IB20) extended this analysis, respectively, to well-sampled RRc light curves obtained with the Kepler space telescope (Koch et al., 2010), to a revised sample of globular clusters (GC) with V-band photometry, and by using Gaia DR2 (Clementini et al., 2019; Gaia Collaboration et al., 2018; Holl et al., 2018) G-band light curves.

Due to the scarcity of accurate high-resolution ($R \gtrsim 20{,}000$) spectroscopic metallicity measurements (capable of providing accuracy of ~ 0.1 dex in [Fe/H]) for individual RRc, these

relations have all been predominantly based on RRc residing in globular clusters (GCs) with well-studied cluster metallicity. In this work, we leverage newly determined RRc high-resolution (HR) metallicities from Crestani et al. (2021b) (C21 hereafter). We combine these measurements with a large sample of metallicities derived with medium-resolution spectroscopic surveys ($R \sim 2{,}000$). This new set of medium-resolution metallicities has been derived with the updated C21 calibration of the ΔS method (Preston, 1959), which relies on ratios between the equivalent widths of Ca and H lines. While not as accurate as HR metallicities, this method can nevertheless provide reliable [Fe/H] abundances with a typical uncertainty of 0.2-0.3 dex.

This work directly follows the analysis presented in Paper I for the calibration of period-ϕ_{31}-[Fe/H] relations for RRab field stars. We take advantage of an extensive catalog of field RRc [Fe/H] abundances from C21 HR spectral measurements, combined with ΔS metallicities estimated from large publicly available medium-resolution spectral datasets. We then cross-correlate this extensive HR+ΔS metallicity catalog with well-sampled archival light curves in order to derive novel period-ϕ_{31}-[Fe/H] relations for RRc in the optical (V-band) and, for the first time, mid-infrared ($W1$ and $W2$ bands). Our work shows these relations can indeed be extended to the thermal infrared, where the light curves are determined mainly by the radius variation during the star's pulsation rather than the effective temperature changes that dominate in the optical wavelengths. This will be crucial to allow the determination of reliable metallicities in upcoming space infrared surveys, such as the James Webb Space Telescope (JWST, Gardner et al., 2006).

This paper is structured as follows. In Section 3.3, we describe the data sets we adopt for our work: the HR+ΔS metallicity catalog utilizing the work of C21 and the optical and infrared time-series catalogs from which we derived the RRc light curves. In Section 3.4, we explain how our period-ϕ_{31}-[Fe/H] relations are calibrated. We then validate our sample to remove contaminants such as eclipsing contact binaries which possess similar light curves to RRc and can often be missclassified. Our results are discussed in Section 3.5, where we assess the precision of the optical and infrared relations, compare our relations with previous ones found in literature,

and apply our method to measure the [Fe/H] abundance in a sample of globular clusters. Lastly, we derive the metallicity distribution of the Milky Way's dwarf spheroidal (dSph) satellite Sculptor and compare it to the metallicities available using other solely photometric methods. Our conclusions are presented in Section 3.6.

3.3   First Overtone RR Lyrae Datasets

Our sample of RRLs is derived from an extensive catalog of 3057 field RRc, for which we have either [Fe/H] abundances derived from HR spectra (40 sources) or an estimate of their metallicity based on the ΔS method (3017 sources). In order to ensure a homogeneous metallicity scale for our entire sample, both HR and ΔS metallicities are based on the calibration provided in C21 (in turn consistent with the Carretta et al. 2009 metallicity scale). The RRc stars for which we obtained ΔS metallicities were extracted from both the full Large Scale Area Multi-Object Spectroscopic Telescope (LAMOST) DR2 survey (Deng et al., 2012; Liu et al., 2014) and the Sloan Extension for Galactic Understanding and Exploration (SEGUE, Yanny et al., 2009) survey datasets. For a complete and detailed description of the metallicity scale, the HR metallicity catalog's demographics, the ΔS calibration, and the spectrum selection criteria, we refer the reader to the C21 paper.

We have then cross-matched the variables in our HR+ΔS metallicity catalog with well-sampled photometric time series in the All-Sky Automated Survey for Supernovae (ASAS-SN, Jayasinghe et al. 2018; Shappee et al. 2014) and the Near-Earth Objects reactivation mission (NEOWISE, Mainzer et al. 2011) of the Wide-field Infrared Survey Explorer (WISE, Wright et al. 2010). From the ASAS-SN survey, we extracted 594 good quality ASAS-SN RRc light curves in the V-band. Similarly, from the WISE/NEOWISE missions we obtained 106 good quality infrared light curves in at least one of the available bands. Individually, the $W1$ (3.4 μm) and $W2$ (4.6 μm) bands had 106 and 71 good quality RRc stellar light curves respectively. From hereafter in the paper, the combination of photometry from both the primary WISE and ongoing NEOWISE mission will be referred to for brevity as WISE. Table 3.1 lists the properties of the

Table 3.1   First overtone mode RR Lyrae calibration sample

	ASAS-SN	WISE		Joint Sample
	V	$W1$	$W2$	V, ($W1$ or $W2$)
Bands	V	$W1$	$W2$	V, ($W1$ or $W2$)
RRc stars	594	106	71	83
Period in days (range)	0.21 - 0.43	0.23 - 0.41	0.24 - 0.41	0.23 - 0.41
Period in days (median value)	0.32	0.32	0.32	0.33
[Fe/H] (range)	-2.54 - (-0.16)	-2.54 - ($+0.55$)	-2.54 - ($+0.06$)	-2.54 - (-0.16)
[Fe/H] (median value)	-1.60	-1.64	-1.65	-1.66
Number of epochs (range)[1]	118 - 835	159 - 2942	159 - 2942	$\cdots$
Number of epochs (median value)	230	205	212	$\cdots$
Magnitude (range)	9.12 - 16.63	8.10 - 13.01	8.12 - 12.75	$\cdots$

RRc in our calibration samples that have passed the stringent photometric and Fourier decomposition criteria described in Section 3.4. The *Joint Sample* column denotes the subset of 83 RRc for which both optical and infrared light curves are available.

Figure 3.1 shows the distribution of period and metallicity for the optical (ASAS-SN) and infrared (WISE) calibration samples and the stars in common (joint). All samples cover the entire period range expected for RRc variables and are representative of the metallicity of Galactic Halo RRLs, with a median [Fe/H] abundance of ≈ -1.6 in both the ASAS-SN and WISE samples. The broad range of metallicities apparent in Figure 3.1 ensures ample leverage for calibrating our period-ϕ_{31}-[Fe/H] relations.

The apparent magnitude distribution of the calibration datasets is shown in Figure 3.2 for the V-band (left panel) and $W1$-band (right). The histogram for the $W2$-band is similar, although fewer in stars due to the lower sensitivity in this band, resulting in generally noisier light curves. The joint sample (hatched in both panels) is noticeably truncated at $V \sim 14$ mag due to the WISE survey's shallower photometric depth.

---

[1] The number of epochs is recorded prior to removing any spurious photometric measurement (see Section 3.4.1).
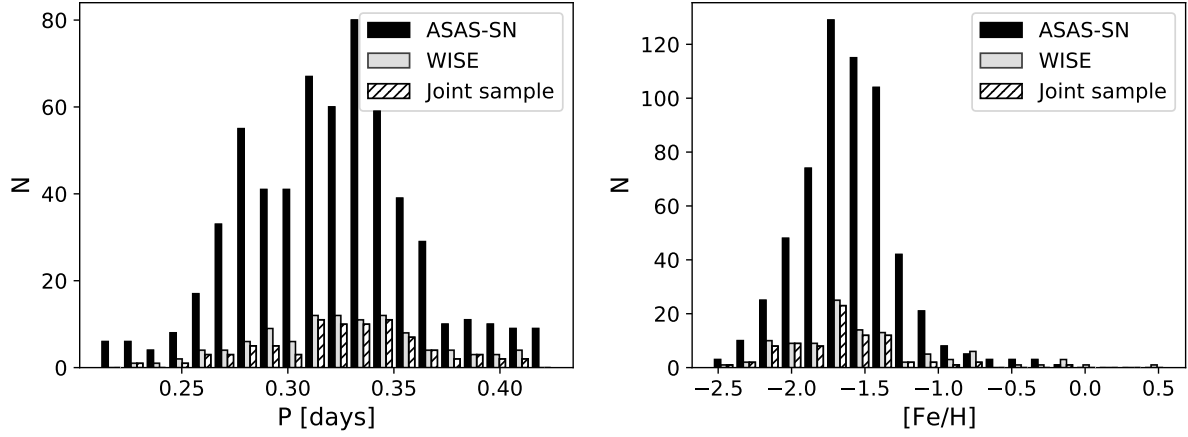
Figure 3.1   Period distribution (left) and spectroscopic [Fe/H] distribution (right) of the different calibration datasets. The histogram labeled "Joint sample" (hatched) corresponds to those stars in common between the ASAS-SN (optical V-band, in black) and WISE (infrared $W1$ and/or $W2$ bands, in grey) datasets.
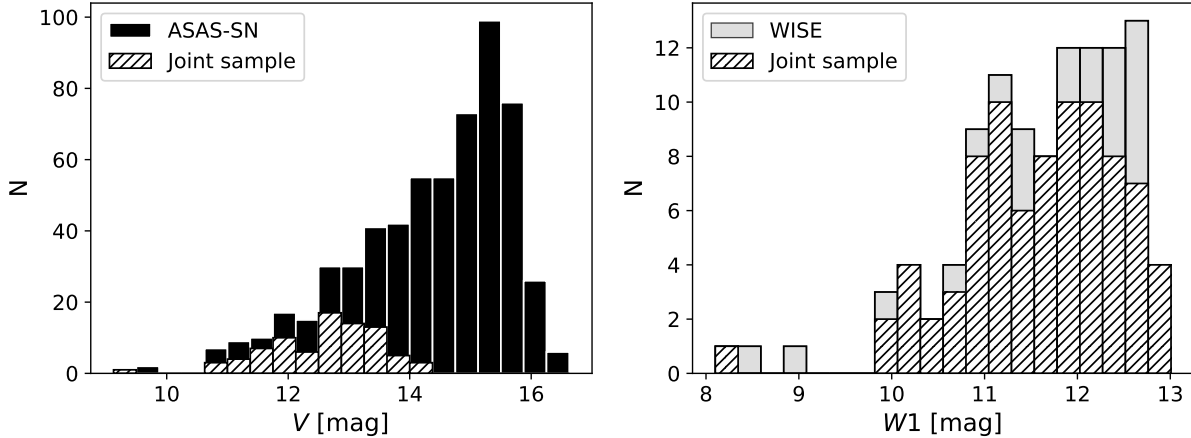
Figure 3.2   Distribution of the average V-band apparent magnitude (left) and the average $W1$-band apparent magnitude (right). Each panel shows both the entire calibration sample (solid fill) and the joint sample (hatched fill, subset of stars having both ASAS-SN and WISE data).

3.4   Calibration of Period-Fourier-Metallicity relation

3.4.1   Data Processing

The extraction of period and Fourier parameters directly follows the procedure outlined in Paper I, Section 3, and is summarized below. We first refine the period of each variable with the Lomb-Scargle method (Lomb, 1976; Scargle, 1982), applied to the large temporal baseline (> 8 years) of the ASAS-SN and WISE time series data. A Gaussian locally-weighted regression smoothing algorithm (GLOESS, Persson et al. 2004) is then applied to the phased data in order to smooth over unevenly sampled data and exclude outliers. A Fourier sine or cosine decomposition is finally executed on each GLOESS light curve by applying a weighted least-squares fit of the following equation (in the case of the sine decomposition):

$$m(\Phi) = A_0 + \sum_{i=1}^{n} A_i \sin[2\pi i(\Phi + \Phi_0) + \phi_i] \tag{3.1}$$

where $m(\Phi)$ is the observed magnitude for either the ASAS-SN or WISE bands, A_0 is the mean magnitude, n is the order of the expansion, Φ is the phase from the GLOESS light curve varying from 0 to 1, Φ_0 is the phase that corresponds to the time of maximum light T_0, A_i and ϕ_i are the i-th order Fourier amplitude and phase coefficients, respectively. A similar equation can be written to represent the equivalent cosine decomposition. For RRc n is often less than five; however, we advise the reader to carefully choose the optimal number of terms for their dataset (see Deb and Singh 2009; Petersen 1986) as the addition of higher-order terms may cause inconsistencies in the value of low order Fourier parameters. For this work, we note that by using an intermediate GLOESS step to eliminate noise factors, the Fourier parameters are consistent between 3, 4, or fifth order decompositions, with the exclusion of a small amount of $\gg 3\sigma$ outliers ($\sim 4\%$ of total RRc for ASAS-SN and $\sim 8\%$ for WISE). This small subset of outliers has been excluded in our processing to make our result invariant between different decomposition orders used. However, it is worth noting that with the robust fitting procedure outlined in Section 3.4.3, the results of this paper remain unaltered with the inclusion/exclusion of these sources.

Figure 3.3 shows a typical V, $W1$, and $W2$ light curve from our RRc calibration stars where the Fourier decomposition fit (solid black line) is plotted on top of the actual photometric data in red.
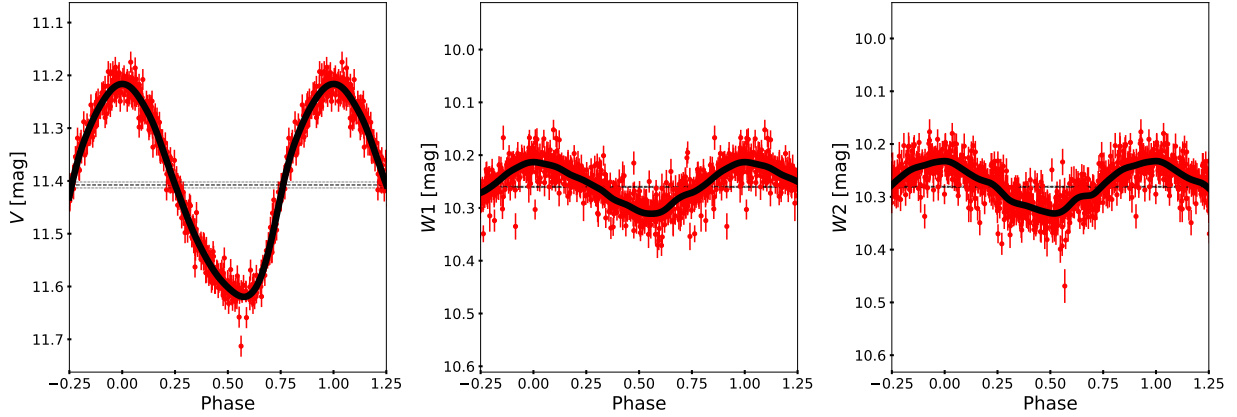
Figure 3.3   Multiple-band light curves for a typical RRc star. The V (left), $W1$ (middle), and $W2$ bands (right) are shown for the star XX Dor (Period = 0.32894 days). The Fourier fit (black solid line) to the GLOESS light curve (see text) is plotted on top of the phased data (red). The average magnitude with its associated error are shown as horizontal black dotted lines. Points automatically rejected by the GLOESS fitting procedure have been removed.

As in Paper I, we explore the link between metallicity and Fourier coefficients through either the ratios of Fourier amplitudes $R_{ij} = A_i/A_j$, or the linear combinations of the phase coefficients $\phi_{ij} = j \cdot \phi_i - i \cdot \phi_j$, where ϕ_{ij} is cyclic in nature and ranges from 0 to 2π. This is shown in Figure 3.4, where several low-order Fourier parameters of individual RRc stars are plotted against period and color-coded based on their [Fe/H]. In the case of the RRc V-band ϕ_{31} values (top-right), it is advantageous to represent the phase parameter as a product of a cosine decomposition rather than sine to avoid the rollover of the ϕ_{31} parameter across the 2π boundary. This can be achieved by either adopting the cosine form of equation 3.1 or using the simple transformation $\phi_{31}^c = \phi_{31}^s - \pi$ between the sine (s superscript) and cosine (c superscript) form of this parameter.

In all V-band panels, we can readily see a gradient in the [Fe/H] distribution of the stars. We found the most distinct separation to be in the ϕ_{31}^c vs. period plot, confirming earlier studies,
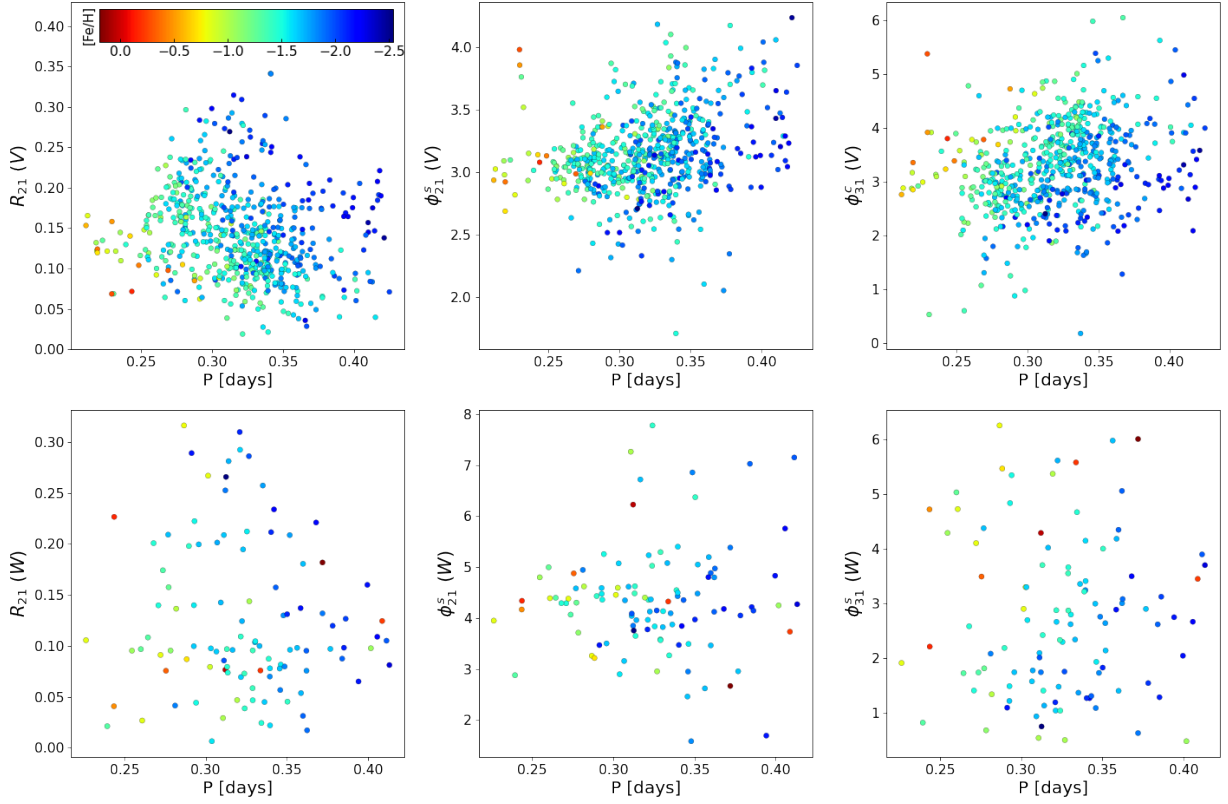
Figure 3.4 ASAS-SN V-band (top row) and $W1$-band (bottom row) Fourier parameters as functions of the period. RRLs are color-coded based on their spectroscopic calibration metallicities. In the rightmost column (ϕ_{31}), [Fe/H] generally goes from metal-rich in the left (red) to metal-poor in the right (blue). All parameters have been derived with a sine Fourier decomposition (indicated with a s superscript), except for the top-right panel ($\phi_{31}^c(V)$ values) where the Fourier phase parameters have been converted to a cosine decomposition (see text). Average errors for each of the parameters plotted are smaller than the size of the data points.

such as M07, which suggests a relation between period and ϕ_{31}^c to be a good indicator of metallicity for the V-band RRc. We similarly found that the ϕ_{31}^s vs. period plot for WISE (bottom-right panel) showed the most distinct trend with metallicity. However, the general metallicity trends in the WISE bands are less apparent than in the optical due to both the smaller sample size and the larger intrinsic dispersion of ϕ_{31} values, covering almost the entire 2π range. As in the case of the RRab stars, we take advantage of the nearly identical shape of the light curves in the $W1$ and $W2$ bands (see e.g., Figure 3.3) to improve the signal in the WISE Fourier parameters, by averaging the $\phi_{31}^s(W1)$ and $\phi_{31}^s(W2)$ values for stars with both light curves available. See Paper I, Section 3.2 for a quantitative discussion demonstrating the validity of this approach for the RRab stars; we have verified this result still holds for our RRc sample.

3.4.2 Eclipsing Contact Binary Contamination

Upon initial creation of our ΔS metallicity sample, we found a significant population of stars that were previously marked as RRc in literature but, on further analysis, were found to be likely eclipsing contact binaries known as W Ursae Majoris (W UMa). Those binaries have sinusoidal light curves similar to RRc variables, and can be confused with first overtone RRL stars if they happen to have similar period and amplitude. If the noise is high enough in a W UMa light curve, it can prevent detecting a characteristic secondary eclipse.

Indeed, we found that for our sample of W UMa, most combinations of Fourier parameters show some degree of degeneracy with regions typical of RRc. In particular, Figure 3.5 shows that some W UMa binaries largely overlap with RRc variables in the optical Bailey diagram, although their amplitude tends to be *smaller*. The overlap is partially mitigated in the infrared ($W1$, shown in figure, or $W2$ diagrams), in which case the same W UMa tends to have *larger* amplitudes than RRc with a similar period. This opposite trend of amplitudes with wavelengths provided us with a simple criterion to automatically identify and reject the W UMa binaries from our sample in the case both bands are available (as in our joint sample): as shown in the left panel of Figure 3.5 the A_{W1}/A_V ratio provides a clear separation between RRc stars and the potential binaries.
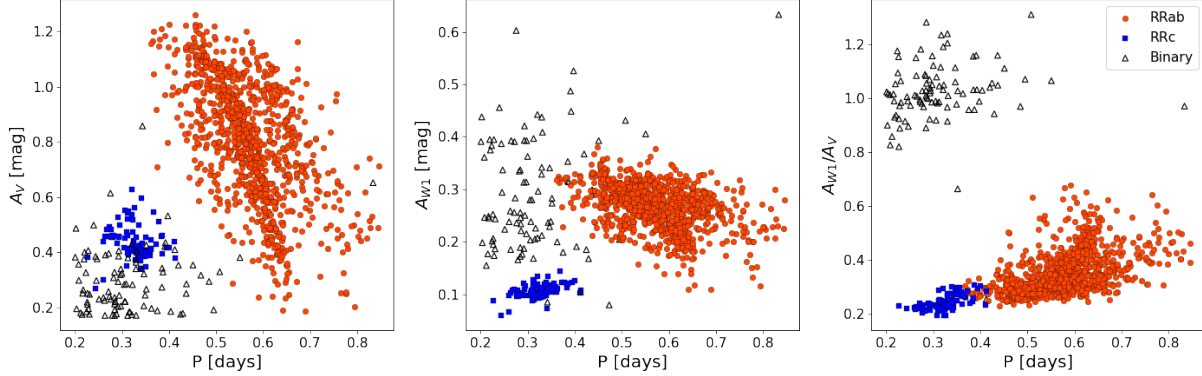
Figure 3.5 Period versus amplitude diagram for the ASAS-SN V-band (left) and the WISE $W1$-band (middle). The right panel shows the ratio of the $W1$ to V amplitudes. Data plotted represents the subset of stars where both optical and infrared are available, i.e. the RRc joint sample discussed in Section 3.3 (blue squares), the RRab joint sample (red circles) from Paper I, and eclipsing contact binary contaminants selected as explained in Section 3.4.2 (empty triangles).

For all sources with only one available light curve (either in the optical or infrared), we resorted to less reliable criteria and manual inspection of the light curves. These criteria were developed for individual bands by analyzing an initial sample of the potential W UMa that have been identified with their amplitude ratio between infrared and optical. If only the V-band photometry was available, we flagged as potential W UMa all sources with $A_V \lessapprox 0.15$ or $\phi_{21}^s(V) > 4.25$. For stars only having infrared data, we instead flagged all stars with $A_W > 0.15$ (in either the $W1$ or $W2$ bands, depending on availability). We then visually examined the phased light curve in the one available band, searching for a secondary light curve minimum, which could have been missed in previous work based on less detailed photometry. We then rejected all sources showing evidence of such secondary eclipses.

The analysis presented in this paper (including Table 3.1) focuses solely on this sample that has been cleaned of W UMa. We provide this final cautionary note that certain W UMa as shown can be easily misconstrued as RRc, and anyone using the relations published in this work should take extreme care in the validity of their RRc sample.

3.4.3   Period-Fourier-[Fe/H] Fitting

As discussed in Section 3.2, RRc photometric metallicities based on a Fourier decomposition of optical light curves are available for different literature relations (see e.g. M07, N13, M14, and IB20). These relations are either linear in both period and ϕ_{31} or use higher-order combinations of these two parameters. Our tests show that, for our sample, higher-order and non-linear terms in the period, ϕ_{31}, or other Fourier parameters result in minimal benefits at the expense of complexity and decreased robustness in the fitting results. For these reasons, we decided to proceed using a simple linear relation in period and ϕ_{31}, similarly to what we did in Paper I for the RRab stars.

To validate this choice of a period-ϕ_{31} plane-fit, we followed the methodology described in Appendix B of Paper I. Principal component analysis showed that 91.30% of the variance in the V-band RRc data could be attributed to just two principal axes (i.e., a plane). This is comparable to the 92.9% value we found for RRab stars in Paper I, which we interpreted as suggesting that a third fit parameter was not needed. A similar analysis for the infrared RRc data set showed that 85.17% of the variance could be attributed to two dimensions (6.74% less than what we found for the RRab in the WISE bands). We attribute this larger variance to a larger relative scatter in the WISE dataset itself (seen in the bottom-right panel of Figure 3.4) due to the smaller amplitude of the pulsations, higher intrinsic photometric noise in the data, and smaller size of the sample. Search for a third observable parameter and/or higher-order fitting functions did not result in a better fit, leading us to adopt a period-ϕ_{31} plane-fit also for the infrared dataset.

We initially attempted to fit an RRc period-ϕ_{31}-[Fe/H] relation adopting the same procedure described in Paper I. We quickly discovered that the smaller size of the RRc sample (by a factor of 3 and 10, compared to the RRab, in the ASAS-SN and WISE bands, respectively) resulted in a fit which was highly dependent upon the exact calibration sample utilized. Bootstrap analysis (Efron and Tibshirani, 1986) highlighted that this instability in the fitting results was due to a combination of higher susceptibility to individual outliers and a stronger correlation between the period and ϕ_{31} slopes. We, however, found that when utilizing different bootstrap samples, the

range of period slopes we were obtaining for the best fit RRc relation was consistent with the value we derived in Paper I for the RRab relation. Based on these considerations, we decided to freeze the period slope of the RRc period-ϕ_{31}-[Fe/H] relation to the RRab value, effectively reducing the RRc fit to a two-parameter fit in the metallicity zero point a and the ϕ_{31} slope c:

$$[\text{Fe/H}] = a + b_F \cdot (P_F - P_0) + c \cdot (\phi_{31} - \phi_{31_0}) \tag{3.2}$$

where b_F is the period slope from the fit of RRab stars in Paper I, equal to -7.60 ± 0.24 dex/day for the ASAS-SN V-band, and -8.33 ± 0.34 dex/day for the WISE bands. Note that, for this choice of values to be appropriate, the period of the RRc variables needs first to be "fundamentalized", or transformed into its equivalent fundamental period by using the equation $\log P_F = \log P_{FO} + 0.127$ (Cox et al., 1983; Iben and Huchra, 1971; Rood, 1973). Fundamentalizing the period of overtone pulsators is a common technique when deriving PLZ and PWZ relations of Cepheids and RRL variables (see, e.g, Groenewegen 2018, Marconi et al. 2015, Neeley et al. 2015) when their smaller number and narrower period range makes it prohibitive to fit them alone. It is worth noting that fundamentalization does have a minor dependence upon metallicity (Bragaglia et al. 2001; Soszyński et al. 2014); however, the effect is so small that no matter the relation tried (e.g., Coppola et al. 2015), the results of this paper remain unchanged. Finally, as in Paper I, we have included the pivot offsets P_0 and ϕ_{31_0} to add further robustness to the fitting procedure; each value is close to the median of the period and [Fe/H] distribution for the RRc sample.

We fit the two remaining free parameters of Equation 3.2, and their uncertainties, using an Orthogonal Distance Regression (ODR) routine combined with Bootstrap re-sampling. The analysis we presented in Paper I for RRab stars showed that ODR tends to minimize trends along all fitted dimensions as no differentiation is made between dependent and independent variables. The ODR fit was run multiple times using bootstrap re-sampling, where in each run all the parameters of each individual calibrator star (period, ϕ_{31}, and [Fe/H]) are randomly replaced with all the corresponding parameters from any singular star in the same calibration dataset.

Namely, we are sampling with replacement our entire calibration dataset before fitting our relation, and ensuring each re-sampled calibration dataset is the same size as our initial sample. Note, all the stars in our calibration sample are fitted with equal weight, as the uncertainties in the fit are dominated by the intrinsic scatter we observe in the period-ϕ_{31}-[Fe/H] plane (see Figure 3.4), in comparison to the small uncertainties in period and the ϕ_{31} parameter (on average $\sim 10^{-6}$ days and ~ 0.02 radians respectively).
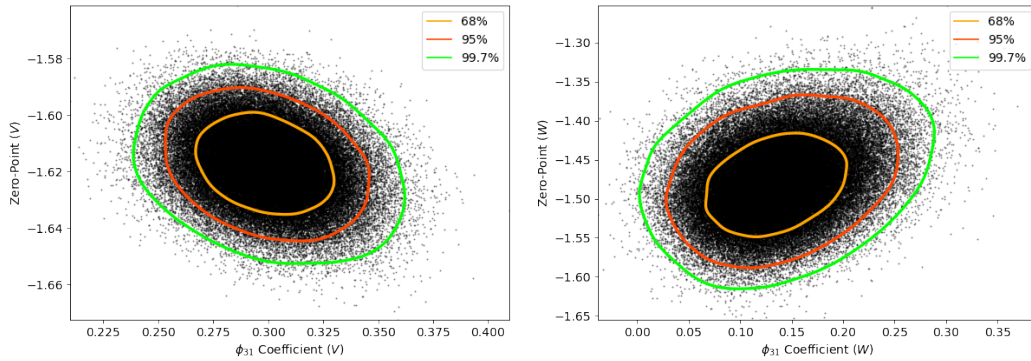
Figure 3.6   Fitting parameters from the bootstrap re-sampled ODR method applied to the ASAS-SN (V) sample left and WISE (W) sample right. Contours shown denote regions containing 68% (orange), 95% (red), and 99.7% (green) of sampled parameters.

Figure 3.6 shows the "cloud" of best fit values obtained with the process described above in the optical and infrared fit. The contours enclose the regions with 68%, 95%, and 99.7% of the ODR best fit values obtained with 100,000 bootstrap re-sampled datasets. The contours provide a visual representation of the robustness of the fitting parameters with respect to outliers and are significantly larger than the corresponding 1, 2 and 3σ error ellipses of the best-fit parameters of individual ODR fits. For this reason, we adopted the mean values and standard deviations of the bootstrap re-sampled ODR fits as solutions and uncertainties for our RRc period-ϕ_{31}-[Fe/H] relations:

$$[\text{Fe/H}]_V = (-1.62 \pm 0.01) + (-7.60) \cdot (P_F - 0.43) + (0.30 \pm 0.02) \cdot (\phi_{31}^c - 3.20) \quad (3.3)$$

$$[\text{Fe/H}]_W = (-1.48 \pm 0.05) + (-8.33) \cdot (P_F - 0.43) + (0.14 \pm 0.05) \cdot (\phi_{31}^s - 2.70) \quad (3.4)$$

where Equations 3.3 and 3.4 provide photometric metallicities for the ASAS-SN V-band and WISE $W1$ and $W2$ infrared bands (averaged when possible, see Section 3.4.1). Note again how the V-band metallicities are expressed as a function of the cosine decomposition of the optical lightcurves (i.e. they depend on ϕ_{31}^c), while the WISE formula is a function of the sine decomposition parameter ϕ_{31}^s.

Figure 3.6 and the uncertainties quoted in Equations 3.3 and 3.4 show that the sampled coefficients occupy a much smaller region of the parameter space in the V-band than the W-band. The larger uncertainties in the infrared coefficients are a reflection of the larger intrinsic scatter we noted in the W-band period-ϕ_{31}-[Fe/H] plane (Figure 3.4) as well as a consequence of the smaller size of the infrared calibrator sample. A detailed analysis of the performance of these relations is provided in Section 3.5. Table 3.2 lists the derived photometric properties for both the V-band and infrared datasets, including the period, ϕ_{31} value, and photometric metallicity derived in each band with Equations 3.3 and 3.4.

3.5   Discussion

3.5.1   Comparison with Globular Clusters Metallicity

In order to test the V-band relation obtained in Section 3.4.3 on an independent sample, we selected a list of ten GCs with metallicity homogeneously spread between $[\text{Fe/H}] = -1.0$ and -2.3 dex. The clusters sampled are the same as in Paper I with two additional GCs: Reticulum (a Large Magellanic Cloud GC) and NGC 6171. Photometry of the clusters comes from

Table 3.2   Derived photometric properties of RRc sample: This table is published in its entirety in machine-readable format. A portion is shown here for guidance regarding its form and content.

Gaia ID (DR3)	Period[2] (day)	ϕ_{31}^c (V) (radian)	$\sigma_{\phi_{31}}$ (V) (radian)	$[\mathrm{Fe/H}]_V$ (dex)	ϕ_{31}^s (W) (radian)	$\sigma_{\phi_{31}}$ (W) (radian)	$[\mathrm{Fe/H}]_W$ (dex)
6914532141197318784	0.334879	5.002	0.017	−1.22			
6913110953698726912	0.324371	3.180	0.008	−1.66			
6910854717182648448	0.323513	4.150	0.013	−1.36			
6897117354482002688	0.322392	3.418	0.007	−1.57			
6731321171497007488	0.223019	2.917	0.005	−0.71			
6688916306549500800	0.339563	3.588	0.004	−1.69	3.244	0.041	−1.61
6340460627660385920	0.285073	2.725	0.004	−1.39			
6340096929829777152	0.384128	4.077	0.011	−2.00	2.619	0.007	−2.19
6307501113055775232	0.339337	3.149	0.009	−1.82			
6299550445690958080	0.296671	3.944	0.004	−1.15			

Piersimoni et al. 2002 (NGC 3201), Kuehn et al. 2013 (Reticulum), M14 (NGC 6171), and the homogeneous data set of P. B. Stetson[3] (hereafter PBS) for the remaining majority.

The general properties of the clusters are listed in Table 3.3, which includes their spectroscopic metallicities (in the scale of C09) and the number of RRL with good-quality well-sampled light curves available in each cluster. The spectroscopic metallicity of the Galactic GCs are obtained from C09, while the metallicity of Reticulum is from Mackey and Gilmore (2004) and converted from the [Fe/H] scale of Zinn and West (1984, ZW84) to C09. A Fourier decomposition was performed on each light curve to obtain their ϕ_{31} parameters, with the exception of the stars in NGC 6171 and NGC 3201 for which the Fourier parameters were taken directly from their respective photometric catalogs. The period-ϕ_{31}-[Fe/H] relations for RRc (Equation 3.3) and RRab (Equation 6 from Paper I with [Fe/H]'s shifted to the scale of C09) were then applied to estimate the metallicity of each RRL star in the clusters. Note, no

---

[2]When both V-band and infrared (WISE) data is present, the period included was calculated from ASAS-SN (V-band) data as the period is usually more accurate due to the higher amplitude and steeper light curve. Period accuracies are quoted to an accuracy on the order of 10^{-6} days, corresponding to a readily detectable $\sim 1\%$ shift in phase for a typical 0.32 day period RRc star when phased over the large temporal (> 8 years) baseline of our datasets.

[3]https://www.canfar.net/storage/list/STETSON/homogeneous

Table 3.3   Photometric metallicities of globular cluster sample

Clusters	$[Fe/H]_{C09}$	RRc stars	$[Fe/H]_{RRc}$	RRab Stars	$[Fe/H]_{RRab}$
NGC 7078 (M15)	-2.33 ± 0.02	36	-2.29 ± 0.06	64	-2.25 ± 0.04
NGC 4590 (M68)	-2.27 ± 0.04	9	-2.23 ± 0.13	13	-2.14 ± 0.11
NGC 4833	-1.89 ± 0.05	3	-1.92 ± 0.40	11	-1.95 ± 0.11
NGC 5286	-1.70 ± 0.07	8	-1.69 ± 0.21	25	-1.76 ± 0.07
Reticulum	-1.67 ± 0.12	4	-1.74 ± 0.05	22	-1.58 ± 0.03
NGC 3201	-1.51 ± 0.02	2	-1.64 ± 0.40	50	-1.38 ± 0.08
NGC 5272 (M3)	-1.50 ± 0.05	28	-1.54 ± 0.12	175	-1.39 ± 0.08
NGC 5904 (M5)	-1.33 ± 0.02	21	-1.37 ± 0.08	67	-1.41 ± 0.07
NGC 6362	-1.07 ± 0.05	13	-1.22 ± 0.08	18	-1.16 ± 0.06
NGC 6171 (M107)	-1.03 ± 0.02	8	-1.20 ± 0.04	15	-0.81 ± 0.13

metallicity scale corrections are needed between that of C09 and the RRc relations presented in this work. The average [Fe/H] abundance of the RRc and RRab variables in each cluster, with their standard deviation, are listed in the 4th and 6th columns of Table 3.3, respectively.

Figure 3.7 shows the spectroscopic [Fe/H] versus the mean photometric [Fe/H] values, calculated for each GC with our relations. Each RRab and RRc stellar photometric metallicity measurement contributes equal weight to the mean photometric [Fe/H] for a given GC. The figure, as well as the individual values listed in Table 3.3, demonstrates the good performance of our formulae (including the new relations for RRc variables) to provide reliable [Fe/H] abundances. The combination of the photometric RRab metallicities (from Paper I) with the new photometric RRc metallicities is in good agreement with the spectroscopic metallicities of the clusters: overall ± 0.08 dex, well within the respective uncertainties.

3.5.2   Comparison with Literature Relations

In this section, we compare photometric metallicities derived using a variety of period-ϕ_{31}-[Fe/H] relations, including the ones found in this work (Equations 3.3 and 3.4), as well as the fits provided by M07, M14, N13, and IB20. Figure 3.8 shows the photometric metallicities for all the RRc in our calibration sample, plotted as a function of their spectroscopic [Fe/H]
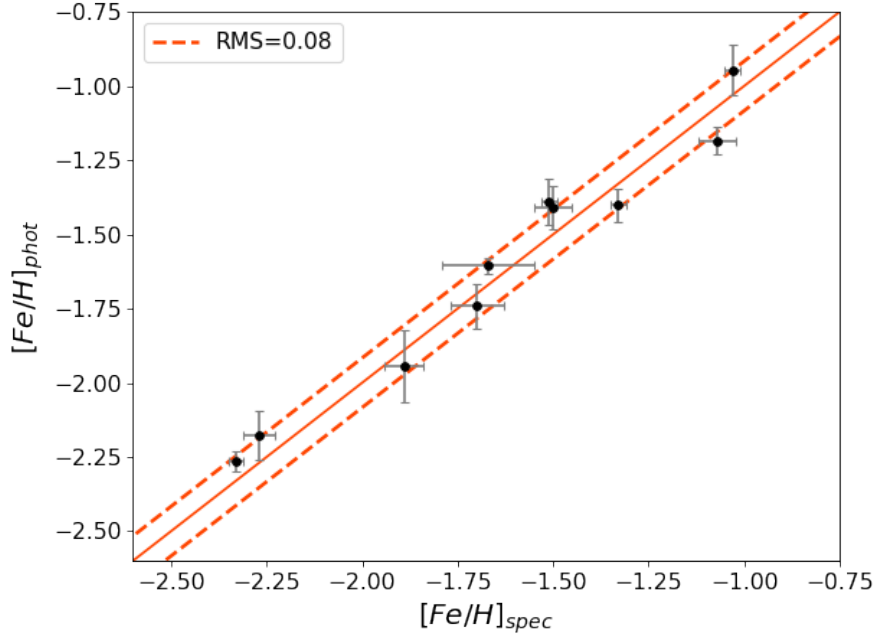
Figure 3.7   [Fe/H]$_{\text{spec}}$ versus [Fe/H]$_{\text{phot}}$ obtained by using Equation 3.3 (this work) for RRc variables, and Equation 6 of Paper I (shifted to the scale of C09) for the RRab, in a sample of 10 GCs. The solid orange line is the 1-1 relation, while the dashed orange lines show the standard deviation (± 0.08 dex). Error bars correspond to the uncertainties in spectroscopic metallicity (from C09 and Mackey and Gilmore 2004) and the statistical error in the photometric metallicity calculated as standard deviation of the metallicity of the individual RRL in the cluster.

abundances. The RMS scatter of each relation, calculated with respect to the ideal one-to-one relationship over the entire spectroscopic metallicity range within which each relation has been calibrated, is indicated in each case.

The top row shows the analysis of our fits in the optical (ASAS-SN, left) and infrared (WISE, right) bands. Since we are directly comparing to the same sample used to derive these relations, the figure allows us to check for remaining trends in the residuals with respect to the ideal one-to-one relation to ensure that our relations provide a consistent estimate of each stars' [Fe/H] over the entire metallicity range of our calibration sample. For the case of the V-band ASAS-SN dataset, we show nearly symmetric residuals (with an RMS ≈ 0.30 dex) over the entire range of
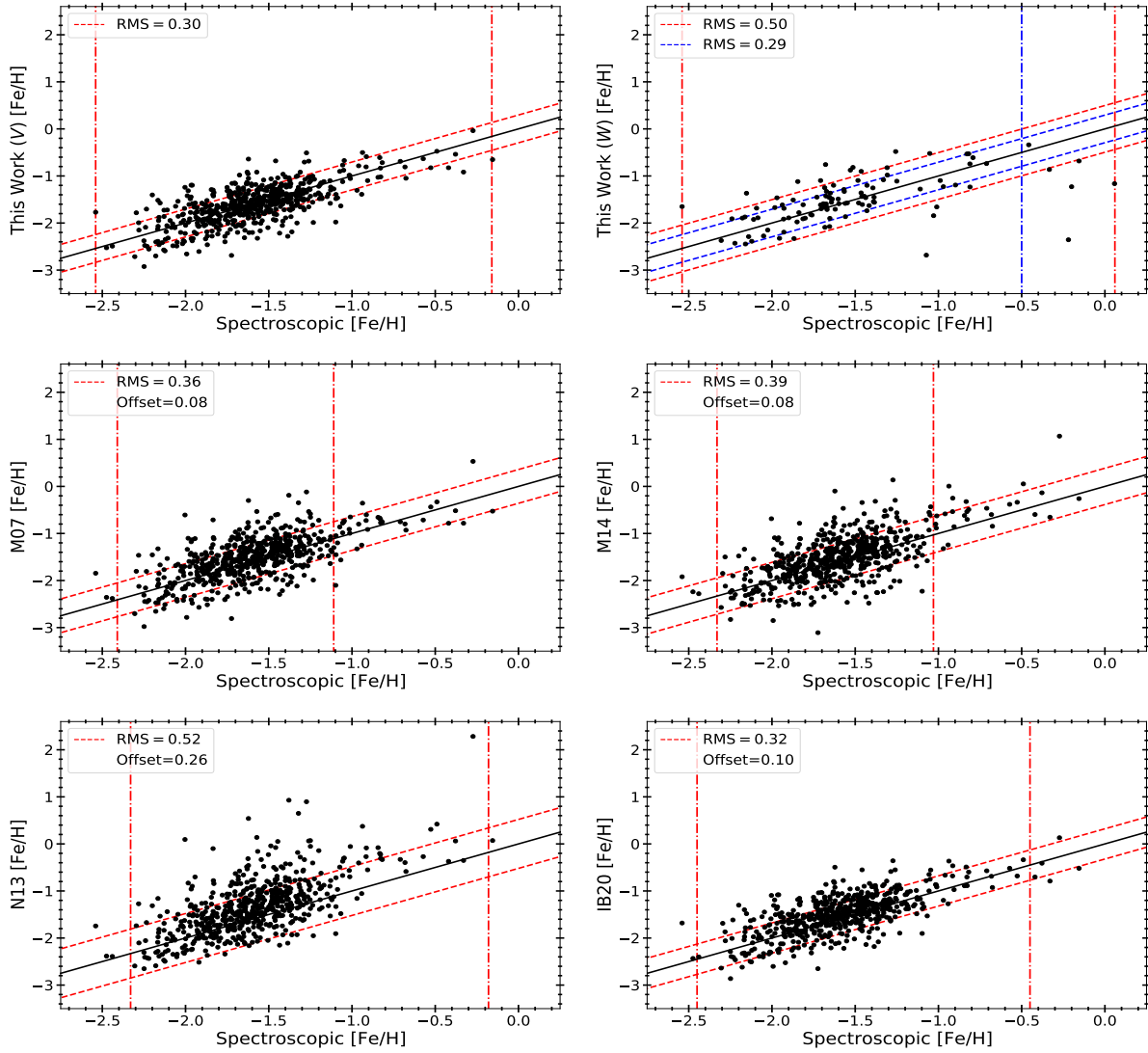
Figure 3.8   Comparison of the spectroscopic [Fe/H] abundances of our calibration sample and those derived with a variety of photometric metallicities, such as the ones presented in Section 3.4.1 (top row), M07 and M14 (middle row), N13 and IB20 (bottom row). The diagonal dashed lines represent the RMS dispersion about the ideal one-to-one relation. The metallicity range used to calibrate each relation is indicated by the two vertical red dash-dotted lines. An additional RMS is shown for WISE band relation (top-right panel, blue dashed lines), calculated using only the stars with [Fe/H] $\lesssim -0.5$ (vertical blue dash-dotted line).

metallicities with only a minor deviation at higher metallicities, still well within the error of our relation. The WISE bands' residuals, however, show some larger divergence at high metallicity ([Fe/H] $\gtrsim$ -0.5), where Equation 3.4 systematically under-predicts the spectroscopic metallicities. The overall residual RMS is also significantly larger (0.50 dex) than the one we obtained in the V-band. Due to the small number of the high metallicity RRc stars, we cannot determine if this is due to non-linearity of the period-ϕ_{31}-[Fe/H] in this metallicity regime, or rather a reflection of less accurate spectroscopic metallicities for the stars in our calibration sample that approach solar [Fe/H] abundance. Indeed, Crestani et al. (2021a) found that the RRL that have been used to calibrate the ΔS method in Crestani et al. (2021b), which in turn we use as the basis for our own relation, show a broad dispersion in α-elements measured through high resolution spectroscopy. Since the ΔS method is based on the strength of a Ca line, while our Fourier-ϕ_{31}-metallicity method aims to measure [Fe/H] metallicities, a spread in α-element abundances can potentially lead to the observed deviations at the ends of the metallicity scale. If we restrict our WISE bands analysis to [Fe/H] $\lesssim$ -0.5, we obtain a best fit relation that is virtually indistinguishable from Equation 3.4 (because of the much larger number of low metallicity RRc, and due to the robustness of our bootstrap fit), but with residual RMS equal to 0.29 dex, nearly identical to the one we found for the V-band (calculated over the entire metallicity range). By directly comparing the V-band (Equation 3.3) and infrared (Equation 3.4) photometric metallicities for the RRc in the joint sample, we note that the two sets of metallicities are consistent with each other, within their respective uncertainties.

The middle-left panel shows the residuals found with the higher-order nonlinear period-ϕ_{31}-[Fe/H] relation of M07 (their equation 4). Note that M07 published two equations: one based on the [Fe/H] scale of ZW84 and one based on that of Carretta and Gratton (1997). We choose to analyze the latter due to its smaller quoted dispersion and simpler functional form. Their relation was based on 106 RRc stars from 12 GCs with V-band Fourier parameters gathered from heterogeneous publications. In order to consistently compare with the HR+ΔS spectroscopic metallicities, we converted the metallicities derived from the M07 relation to that of

C09 using the relation $[\text{Fe/H}]_{\text{C09}} = (1.137 \pm 0.060)[\text{Fe/H}]_{\text{CG97}} - 0.003$ (provided by C09). A few years later, M14 published an updated version of their V-band M07 fit, using the same base of RRc extended to include a total of 163 stars gathered from 19 GCs, with a metallicity scale updated to that of C09. Although they found a slightly different nonlinear period-ϕ_{31}-[Fe/H] functional form, the metallicities predicted by M14 (center-right panel in Figure 3.8) appear to be roughly the same as those provided by M07. Both relations do not appear to have a trend or bias with respect to the spectroscopic metallicities, but they do have a larger RMS (0.36 and 0.39 dex. respectively) than our ASAS-SN relation.

N13 provided a nonlinear period-ϕ_{31}-[Fe/H] for the Kepler Space Telescope's Kp band (their Equation 4). Due to the small field-of-view (relatively to large-area surveys) of Kepler's primary mission, this relation is calibrated by augmenting the sample of 3 RRc obtained in Kepler's field with the Fourier parameters of 98 GC RRc from M07, converted to the Kp system using the relation $\phi_{31}(V) = \phi_{31}(Kp) - (0.151 \pm 0.026)$, from Nemec et al. 2011. We use this same relation to convert the V-band ϕ_{31} parameters of our spectroscopic sample to the Kp photometric system in order to generate the bottom-left panel of Figure 3.8. The plot shows that the N13 largely predicts the [Fe/H] metallicities without noticeable trends even outside their [Fe/H] calibration range, albeit with a small negative bias (the average metallicity predicted by N13 is 0.26 dex lower than the spectroscopic values), and a larger scatter (RMS = 0.52 dex) than all other relations here evaluated.

Finally, IB20 used a sample of 50 GC RRc stars extracted from the Gaia DR2 database to derive a bi-linear period-ϕ_{31}-[Fe/H] relation (Equation 4 in their paper) with the same functional form of our Equations 3.3 and 3.4. In order to apply this relation to our dataset, we had to perform two transformations: (1) we converted the V-band ϕ_{31} value of our ASAS-SN sample to the G-band system, using the relation $\phi_{31}(G) = (0.104 \pm 0.020) + (1.000 \pm 0.008)\phi_{31}(V)$ from Clementini et al. (2016), and (2) we transformed the metallicity provided by the IB20 relation (in the ZW84 scale) into the Carretta scale using the $[\text{Fe/H}]_{\text{C09}} = 1.105[\text{Fe/H}]_{\text{ZW84}} + 0.160$ relation from C09. The results are shown in the bottom-right panel of Figure 3.8. Again, no obvious trend

or offset is found, and the RMS dispersion (0.32 dex) is among the smallest of the relations assessed in this Section, comparable to the RMS we measure in the V-band with our Equation 3.3.

Overall, M07, M14, and N13 share the majority of their photometric calibration dataset but differ in their functional form by adding slightly different combinations of nonlinear terms. Figure 3.8 shows that, with respect to optical *linear* relations (IB20 and Equation 3.3 in this work), these non-linear relations tend to have larger residual dispersion for our large sample of spectroscopic metallicities. With the exception of the infrared WISE band (where we observe a possible departure at solar metallicities), our dataset does not support the need for the addition of non-linear terms in photometric metallicities relations based on Fourier parameters of RRc optical lightcurves.

3.5.3 Comparison with Sculptor dSph Metallicity

In this section, we test our V-band period-ϕ_{31}-[Fe/H] relations with RRL stars in the Milky Way's dSph satellite Sculptor. We compare our photometric Fourier metallicities to those derived by Martínez-Vázquez et al. (2016a) (hereafter MV16b) by inverting the theoretical PLZ relation from Marconi et al. (2015). Being a relatively nearby local group galaxy ($\mu_0 = 19.62$ mag; Martínez-Vázquez et al. 2015), Sculptor has been extensively studied as a probe for galaxy evolution, and detailed studies are available of its variable star content with photometry stretching back over two decades (for a thorough review see Martínez-Vázquez et al. 2016b, hereafter MV16a). We specifically chose Sculptor as a test case for our Fourier-metallicity relations as this dwarf galaxy has been shown to have an early history of chemical enrichment, resulting in an older stellar population (including RRL stars) with a broad range of metallicity ($\gtrsim 1$ dex, see Clementini et al. 2005; Martínez-Vázquez et al. 2015, 2016a). By studying Sculptor, we show that the relations provided in this work are widely applicable to complex stellar populations, beyond RRLs in the field or GCs.

Sculptor photometry is available from the PBS database in both the I-band (utilized by MV16b in their work) and the V-band. We refer to MV16a for the exact details of the observing

runs, bands observed, instruments and telescopes used to collect the Sculptor photometry in PBS. Out of 536 known RRLs (289 RRab, 197 RRc, and 50 RRd; MV16a), MV16b derived photometric metallicities for 276 RRab and 195 RRc stars. However, only 277 of these stars (126 RRab and 148 RRc)have good quality V-band light curves (according to the criteria outlines in Paper I, Section 3). For these stars we have extracted their V-band Fourier parameters, following the procedures described in Section 3.4.1. We have then estimated their photometric [Fe/H] abundances, using our Fourier-metallicity relations for RRab (Equation 6 from Paper I with [Fe/H]'s shifted to the scale of C09) and RRc (Equation 3 from section 3.4.3) stars respectively.

The results of this analysis are shown in Figure 3.9. The top-left panel shows the Fourier metallicity distributions of Sculptor's RRab and RRc stars. The two histograms have a similar mean (-1.88 dex and -1.83 dex for the RRab and RRc, respectively) and dispersion ($\sigma_{RRab} = 0.48$ dex and $\sigma_{RRc} = 0.36$ dex). The remaining panels of Figure 3.9 compare the metallicity distribution obtained with our Fourier method with the [Fe/H] abundance derived via PLZ inversion by MV16b. We find a remarkable agreement between the metallicities derived with these two methods. In the overall sample (RRab and RRc together, top-right panel) we measured a mean metallicity [Fe/H] $\simeq -1.85$ dex, matching the value of [Fe/H] $\simeq -1.90$ dex found by MV16b. The dispersion and shape of the two [Fe/H] distributions is also very similar, with both methods suggesting a spread of metallicities in the Sculptor RRL population of ~ 2 dex. Note that while the Fourier metallicities derived in this work suggest the presence of a small high-metallicity tail (with a few stars having [Fe/H] between -1.0 and -0.5 dex, not seen in MV16b), this excess may be an artifact originating in the calibration of our relation, as noted in section 3.5.2. Comparison of the Fourier and PLZ metallicities derived for RRab and RRc separately (bottom row in Figure 3.9) leads to similar conclusions.

These results are also consistent with Sculptor's spectroscopic metallicities. Clementini et al. (2005) found a [Fe/H] peaking at ~ -1.8 dex via the ΔS spectroscopic method applied to a sample of 107 RRL. Achieving such a consistent mean metallicity and distribution validates both of these photometric approaches, especially since the two photometric relations are completely
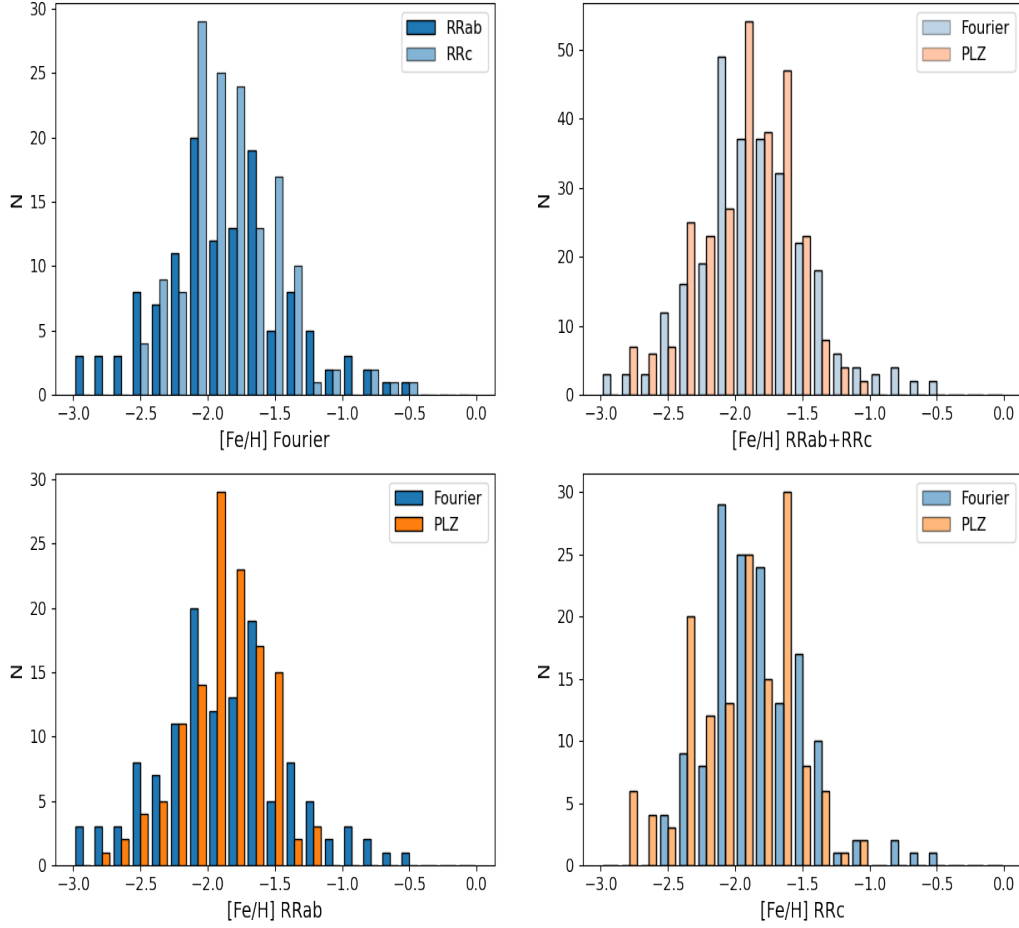
Figure 3.9 Comparison of derived [Fe/H] distributions of Sculptor dSph variables. *Top Left*: Histogram of the [Fe/H] obtained by using the Fourier V-band ϕ_{31} applied to Equation 3.3 (this work) for RRc variables, and Equation 6 of Paper I (shifted to the scale of C09) for the RRab. Remaining panels compare the Fourier ϕ_{31} derived [Fe/H] to those derived in MV16b (through inversion of an I-band PLZ relation, see text) for the entire RRab+RRc sample (*Top Right*), and solely RRab or RRc variables (*Bottom Left* and *Bottom Right*, respectively).

independent of one another both in methodology (shape of the light curve as opposed to inversion of the PLZ relation) and in the dataset used (V band vs. I band, and light curves with different sampling and coverage).

3.6   Conclusions

In this work, we provide new relations to derive photometric metallicities based on the ϕ_{31} Fourier parameter of optical and, for the first time, infrared light curves of RRc variables. Our relations are calibrated using a large sample ($\sim 4\times$ larger than anything used prior at optical wavelengths) of field RRc variables for which homogeneous spectroscopic abundances are available and cover a broad range of metallicities ($-2.5 \lesssim [\mathrm{Fe/H}] \lesssim 0.0$) derived from HR spectra and the ΔS method, using techniques developed by C21. The photometric time series of our calibration stars were extracted from the ASAS-SN (V band) and the WISE (NEOWISE extension, $W1$ and $W2$ bands) surveys, providing well-sampled light curves that allow for reliable Fourier expansions.

Comparisons with other optical photometric metallicity relations for RRc variables show that our formula provides reliable [Fe/H] abundances without noticeable trends over the entire metallicity range found in the Milky Way halo. Our V-band relation (Equation 3.3) reproduces spectroscopic metallicities with a residual standard deviation of $\simeq 0.30$ dex, smaller than the higher-order relations found in the literature. We tested our V-band relation on RRLs in GCs and shown that we can accurately estimate the average clusters' metallicity with an overall accuracy of ~ 0.08 dex. Additionally, we have shown this relation can reproduce the [Fe/H] distribution of systems with a more complicated history of chemical enrichment, such as the Sculptor dSph, consistent with the predictions of both spectroscopy and other photometric relations.

For the first time, We have also obtained a mid-infrared period-ϕ_{31}-[Fe/H] relation in the WISE $W1$ and $W2$ bands (Equation 3.4). Despite having a calibration sample five times smaller than the V-band sample, our mid-infrared relation has similar accuracy ($\simeq 0.29$ dex) in the low and moderate metallicity range ($[\mathrm{Fe/H}] \lesssim -0.5$ dex). In the high metallicity range, our relation appears to under-predict the [Fe/H] abundance expected from spectroscopy; further analysis

(relying on a larger sample of solar-metallicity RRc calibrators) is needed to understand the root cause of this deviation.

This work complements the analysis we presented in Paper I, where we derived similar relations for field RRab variables using the same techniques described here (and a calibration catalog with spectroscopic metallicities derived with the same methods). Section 3.5.1 shows that, for stellar populations where both RRab and RRc variables are found (e.g., many Galactic GCs), combining spectroscopic metallicities from RRL in both pulsation modes further improves the [Fe/H] reliability, with an accuracy of the population average metallicity approaching high-resolution spectroscopic measurements.

Whether in the mid-infrared or optical, for the RRab or RRc, the relations presented here will be crucial to facilitate the quick determination of reliable RRL metallicities for the many upcoming wide-area time-domain surveys and ELTs (such as LSST at the Vera C. Rubin Observatory). Our mid-infrared relation will allow future telescopes (such as JWST and the Roman telescope) to reach RRLs across the Local Group of galaxies, where spectral observations will not be feasible. Finally, by providing a method to obtain reliable metallicities of individual RRL, Paper I and this work will be crucial in determining accurate distances with PLZ and PWZ relations.

3.7 References

Abbott, T.M.C., Abdalla, F.B., Allam, S. et al (2018). The Dark Energy Survey: Data Release 1. *The Astrophysical Journal Supplement Series*, 239(2):18.

Akeson, R., Armus, L., Bachelet, E. et al (2019). The Wide Field Infrared Survey Telescope: 100 Hubbles for the 2020s. *arXiv e-prints*, page arXiv:1902.05569.

Bernard, E.J., Monelli, M., Gallart, C. et al (2010). The ACS LCID Project. II. Faint Variable Stars in the Isolated Dwarf Irregular Galaxy IC 1613. *The Astrophysical Journal*, 712(2):1259–1276.

Bernard, E.J., Monelli, M., Gallart, C. et al (2009). The ACS LCID Project. I. Short-Period Variables in the Isolated Dwarf Spheroidal Galaxies Cetus and Tucana. *The Astrophysical Journal*, 699(2):1742–1764.

Bernard, E.J., Monelli, M., Gallart, C. et al (2013). The ACS LCID Project - VIII. The short-period Cepheids of Leo A. *Monthly Notices of the Royal Astronomical Society*, 432(4):3047–3061.

Bragaglia, A., Gratton, R.G., Carretta, E. et al (2001). Metallicities for Double-Mode RR Lyrae Stars in the Large Magellanic Cloud. *Astronomical Journal*, 122(1):207–219.

Breuval, L., Kervella, P., Wielgórski, P. et al (2021). The Influence of Metallicity on the Leavitt Law from Geometrical Distances of Milky Way and Magellanic Cloud Cepheids. *The Astrophysical Journal*, 913(1):38.

Carretta, E., Bragaglia, A., Gratton, R. et al (2009). Intrinsic iron spread and a new metallicity scale for globular clusters. *Astronomy and Astrophysics*, 508(2):695–706.

Carretta, E. and Gratton, R.G. (1997). Abundances for globular cluster giants. I. Homogeneous metallicities for 24 clusters. *Astronomy and Astrophysics, Supplement*, 121:95–112.

Chambers, K.C., Magnier, E.A., Metcalfe, N. et al (2016). The Pan-STARRS1 Surveys. *arXiv e-prints*, page arXiv:1612.05560.

Clementini, G., Ripepi, V., Bragaglia, A. et al (2005). The metal abundance distribution of the oldest stellar component in the Sculptor dwarf spheroidal galaxy*. *Monthly Notices of the Royal Astronomical Society*, 363(3):734–748.

Clementini, G., Ripepi, V., Leccia, S. et al (2016). Gaia Data Release 1. The Cepheid and RR Lyrae star pipeline and its application to the south ecliptic pole region. *Astronomy and Astrophysics*, 595:A133.

Clementini, G., Ripepi, V., Molinaro, R. et al (2019). Gaia Data Release 2. Specific characterisation and validation of all-sky Cepheids and RR Lyrae stars. *Astronomy and Astrophysics*, 622:A60.

Coppola, G., Marconi, M., Stetson, P.B. et al (2015). The Carina Project IX: On Hydrogen and Helium Burning Variables. *The Astrophysical Journal*, 814(1):71.

Cox, A.N., Hodson, S.W. and Clancy, S.P. (1983). Double-mode RR Lyrae variables in M15. *The Astrophysical Journal*, 266:94–104.

Crestani, J., Braga, V.F., Fabrizio, M. et al (2021a). On the Use of Field RR Lyrae as Galactic Probes. III. The α-element Abundances. *The Astrophysical Journal*, 914(1):10.

Crestani, J., Fabrizio, M., Braga, V.F. et al (2021b). On the Use of Field RR Lyrae as Galactic Probes. II. A New ΔS Calibration to Estimate Their Metallicity. *The Astrophysical Journal*, 908(1):20.

Dambis, A.K., Berdnikov, L.N., Kniazev, A.Y. et al (2013). RR Lyrae variables: visual and infrared luminosities, intrinsic colours and kinematics. *Monthly Notices of the Royal Astronomical Society*, 435(4):3206–3220.

Deb, S. and Singh, H.P. (2009). Light curve analysis of variable stars using Fourier decomposition and principal component analysis. *Astronomy and Astrophysics*, 507(3):1729–1737.

Deng, L.C., Newberg, H.J., Liu, C. et al (2012). LAMOST Experiment for Galactic Understanding and Exploration (LEGUE) — The survey's science plan. *Research in Astronomy and Astrophysics*, 12(7):735–754.

Drake, A.J., Djorgovski, S.G., Mahabal, A. et al (2009). First Results from the Catalina Real-Time Transient Survey. *The Astrophysical Journal*, 696(1):870–884.

Efron, B. and Tibshirani, R. (1986). Bootstrap Methods for Standard Errors, Confidence Intervals, and Other Measures of Statistical Accuracy. *Statistical Science*, 1(1):54 – 75.

Fabrizio, M., Braga, V.F., Crestani, J. et al (2021). On the use of field RR Lyrae as Galactic probes: IV. New insights into and around the Oosterhoff dichotomy. *arXiv e-prints*, page arXiv:2107.00919.

Gaia Collaboration, Brown, A.G.A., Vallenari, A. et al (2018). Gaia Data Release 2. Summary of the contents and survey properties. *Astronomy and Astrophysics*, 616:A1.

Gardner, J.P., Mather, J.C., Clampin, M. et al (2006). The James Webb Space Telescope. *Space Science Reviews*, 123(4):485–606.

Gilligan, C.K., Chaboyer, B., Marengo, M. et al (2021). Metallicities from high-resolution spectra of 49 RR Lyrae variables. *Monthly Notices of the Royal Astronomical Society*, 503(4):4719–4733.

Groenewegen, M.A.T. (2018). The Cepheid period-luminosity-metallicity relation based on Gaia DR2 data. *Astronomy and Astrophysics*, 619:A8.

Holl, B., Audard, M., Nienartowicz, K. et al (2018). Gaia Data Release 2. Summary of the variability processing and analysis results. *Astronomy and Astrophysics*, 618:A30.

Iben, I., J. and Huchra, J. (1971). Comments on the Instability Strip for Halo Population Variables. *Astronomy and Astrophysics*, 14:293.

Iorio, G. and Belokurov, V. (2020). Chemo-kinematics of the *Gaia* RR Lyrae: the halo and the disc. *arXiv e-prints*, page arXiv:2008.02280.

Ivezić, Ž., Kahn, S.M., Tyson, J.A. et al (2019). LSST: From Science Drivers to Reference Design and Anticipated Data Products. *The Astrophysical Journal*, 873(2):111.

Jayasinghe, T., Kochanek, C.S., Stanek, K.Z. et al (2018). The ASAS-SN catalogue of variable stars I: The Serendipitous Survey. *Monthly Notices of the Royal Astronomical Society*, 477(3):3145–3163.

Jurcsik, J. and Kovacs, G. (1996). Determination of [Fe/H] from the light curves of RR Lyrae stars. *Astronomy and Astrophysics*, 312:111–120.

Koch, D.G., Borucki, W.J., Basri, G. et al (2010). Kepler Mission Design, Realized Photometric Performance, and Early Science. *The Astrophysical Journal Letters*, 713(2):L79–L86.

Kuehn, C.A., Dame, K., Smith, H.A. et al (2013). Variable Stars in Large Magellanic Cloud Globular Clusters. III. Reticulum. *Astronomical Journal*, 145(6):160.

Leavitt, H.S. (1908). 1777 variables in the Magellanic Clouds. *Annals of Harvard College Observatory*, 60:87–108.3.

Leavitt, H.S. and Pickering, E.C. (1912). Periods of 25 Variable Stars in the Small Magellanic Cloud. *Harvard College Observatory Circular*, 173:1–3.

Liu, X.W., Yuan, H.B., Huo, Z.Y. et al (2014). LSS-GAC - A LAMOST Spectroscopic Survey of the Galactic Anti-center. In Feltzing, S., Zhao, G., Walton, N.A. et al, editors, *Setting the scene for Gaia and LAMOST*, volume 298 of *IAU Symposium*, pages 310–321.

Lomb, N.R. (1976). Least-Squares Frequency Analysis of Unequally Spaced Data. *Astrophysics and Space Science*, 39(2):447–462.

Mackey, A.D. and Gilmore, G.F. (2004). Comparing the properties of local globular cluster systems: implications for the formation of the Galactic halo. *Monthly Notices of the Royal Astronomical Society*, 355(2):504–534.

Mainzer, A., Bauer, J., Grav, T. et al (2011). Preliminary Results from NEOWISE: An Enhancement to the Wide-field Infrared Survey Explorer for Solar System Science. *The Astrophysical Journal*, 731(1):53.

Marconi, M., Coppola, G., Bono, G. et al (2015). On a New Theoretical Framework for RR Lyrae Stars. I. The Metallicity Dependence. *The Astrophysical Journal*, 808(1):50.

Martínez-Vázquez, C.E., Monelli, M., Bernard, E.J. et al (2017). The ISLAnds Project. III. Variable Stars in Six Andromeda Dwarf Spheroidal Galaxies. *The Astrophysical Journal*, 850(2):137.

Martínez-Vázquez, C.E., Monelli, M., Bono, G. et al (2015). Variable stars in Local Group Galaxies - I. Tracing the early chemical enrichment and radial gradients in the Sculptor dSph with RR Lyrae stars. *Monthly Notices of the Royal Astronomical Society*, 454(2):1509–1516.

Martínez-Vázquez, C.E., Monelli, M., Bono, G. et al (2016). A new Phi_31-period-metallicity relation for RR Lyrae stars. *Commmunications of the Konkoly Observatory Hungary*, 105:53–56.

Martínez-Vázquez, C.E., Monelli, M., Gallart, C. et al (2016a). Probing the early chemical evolution of the Sculptor dSph with purely old stellar tracers. *Monthly Notices of the Royal Astronomical Society*, 461(1):L41–L45.

Martínez-Vázquez, C.E., Stetson, P.B., Monelli, M. et al (2016b). Variable stars in Local Group Galaxies - II. Sculptor dSph. *Monthly Notices of the Royal Astronomical Society*, 462(4):4349–4370.

Matteucci, F. (2021). Modelling the chemical evolution of the Milky Way. *arXiv e-prints*, page arXiv:2106.13145.

Monelli, M., Fiorentino, G., Bernard, E.J. et al (2017). Variable Stars in Local Group Galaxies. III. And VII, NGC 147, and NGC 185: Insight into the Building Blocks of the M31 Halo. *The Astrophysical Journal*, 842(1):60.

Morgan, S. (2014). Revision of the [Fe/H] - φ_{31} - P relationship for RRc variables. In Guzik, J.A., Chaplin, W.J., Handler, G. et al, editors, *Precision Asteroseismology*, volume 301, pages 461–462.

Morgan, S.M., Wahl, J.N. and Wieckhorst, R.M. (2007). [Fe/H] relations for c-type RR Lyrae variables based upon Fourier coefficients. *Monthly Notices of the Royal Astronomical Society*, 374(4):1421–1426.

Mullen, J.P., Marengo, M., Martínez-Vázquez, C.E. et al (2021). Metallicity of Galactic RR Lyrae from Optical and Infrared Light Curves. I. Period-Fourier-Metallicity Relations for Fundamental-mode RR Lyrae. *The Astrophysical Journal*, 912(2):144.

Muraveva, T., Delgado, H.E., Clementini, G. et al (2018). RR Lyrae stars as standard candles in the Gaia Data Release 2 Era. *Monthly Notices of the Royal Astronomical Society*, 481(1):1195–1211.

Neeley, J.R., Marengo, M., Bono, G. et al (2017). On a New Theoretical Framework for RR Lyrae Stars. II. Mid-infrared Period-Luminosity-Metallicity Relations. *The Astrophysical Journal*, 841(2):84.

Neeley, J.R., Marengo, M., Bono, G. et al (2015). On the Distance of the Globular Cluster M4 (NGC 6121) Using RR Lyrae Stars. II. Mid-infrared Period-luminosity Relations. *The Astrophysical Journal*, 808(1):11.

Neeley, J.R., Marengo, M., Freedman, W.L. et al (2019). Standard Galactic field RR Lyrae II: a Gaia DR2 calibration of the period-Wesenheit-metallicity relation. *Monthly Notices of the Royal Astronomical Society*, 490(3):4254–4270.

Nemec, J.M., Cohen, J.G., Ripepi, V. et al (2013). Metal Abundances, Radial Velocities, and Other Physical Characteristics for the RR Lyrae Stars in The Kepler Field. *The Astrophysical Journal*, 773(2):181.

Nemec, J.M., Smolec, R., Benkő, J.M. et al (2011). Fourier analysis of non-Blazhko ab-type RR Lyrae stars observed with the Kepler space telescope. *Monthly Notices of the Royal Astronomical Society*, 417(2):1022–1053.

Ngeow, C.C., Yu, P.C., Bellm, E. et al (2016). The Palomar Transient Factory and RR Lyrae: The Metallicity-Light Curve Relation Based on ab-type RR Lyrae in the Kepler Field. *The Astrophysical Journal Supplement Series*, 227(2):30.

Persson, S.E., Madore, B.F., Krzemiński, W. et al (2004). New Cepheid Period-Luminosity Relations for the Large Magellanic Cloud: 92 Near-Infrared Light Curves. *Astronomical Journal*, 128(5):2239–2264.

Petersen, J.O. (1986). Studies of Cepheid type variability. IV. The uncertainties of Fourierdecomposition parameters. *Astronomy and Astrophysics*, 170:59–69.

Piersimoni, A.M., Bono, G. and Ripepi, V. (2002). BVI Time-Series Data of the Galactic Globular Cluster NGC 3201. I. RR Lyrae Stars. *Astronomical Journal*, 124(3):1528–1554.

Preston, G.W. (1959). A Spectroscopic Study of the RR Lyrae Stars. *The Astrophysical Journal*, 130:507.

Ricker, G.R., Winn, J.N., Vanderspek, R. et al (2015). Transiting Exoplanet Survey Satellite (TESS). *Journal of Astronomical Telescopes, Instruments, and Systems*, 1:014003.

Rood, R.T. (1973). Metal-Poor Stars. V. Horizontal-Branch Morphology. *The Astrophysical Journal*, 184:815–838.

Savino, A., Koch, A., Prudil, Z. et al (2020). The age of the Milky Way inner stellar spheroid from RR Lyrae population synthesis. *Astronomy and Astrophysics*, 641:A96.

Scargle, J.D. (1982). Studies in astronomical time series analysis. II. Statistical aspects of spectral analysis of unevenly spaced data. *The Astrophysical Journal*, 263:835–853.

Shappee, B.J., Prieto, J.L., Grupe, D. et al (2014). The Man behind the Curtain: X-Rays Drive the UV through NIR Variability in the 2013 Active Galactic Nucleus Outburst in NGC 2617. *The Astrophysical Journal*, 788(1):48.

Simon, N.R. and Lee, A.S. (1981). The structural properties of cepheid light curves. *The Astrophysical Journal*, 248:291–297.

Smolec, R. (2005). Metallicity Dependence of the Blazhko Effect. *Acta Astronomica*, 55:59–84.

Soszyński, I., Udalski, A., Szymański, M.K. et al (2014). Over 38000 RR Lyrae Stars in the OGLE Galactic Bulge Fields. *Acta Astronomica*, 64(3):177–196.

Walker, A.R. (1989). A Survey for RR Lyrae Variables in Five Small Magellanic Cloud Clusters. *Publications of the ASP*, 101:570.

Wright, E.L., Eisenhardt, P.R.M., Mainzer, A.K. et al (2010). The Wide-field Infrared Survey Explorer (WISE): Mission Description and Initial On-orbit Performance. *Astronomical Journal*, 140(6):1868–1881.

Yanny, B., Rockosi, C., Newberg, H.J. et al (2009). SEGUE: A Spectroscopic Survey of 240,000 Stars with g = 14-20. *Astronomical Journal*, 137(5):4377–4399.

Zinn, R. and West, M.J. (1984). The globular cluster system of the Galaxy. III. Measurements of radial velocity and metallicity for 60 clusters and a compilation of metallicities for 121 clusters. *The Astrophysical Journal Supplement Series*, 55:45–66.

CHAPTER 4. RR LYRAE MID-INFRARED PERIOD-LUMINOSITY-METALLICITY AND PERIOD-WESENHEIT-METALLICITY RELATIONS BASED ON GAIA DR3 PARALLAXES

Authors

Joseph P. Mullen (1), Massimo Marengo (1 and 2), Clara E. Martínez-Vázquez (3 and 4), Brian Chaboyer (5), Giuseppe Bono (6 and 7), Vittorio F. Braga (7 and 8), Massimo Dall'Ora (9), Valentina D'Orazi (6 and 10), Michele Fabrizio (7 and 11), Matteo Monelli (8 and 12), Frédéric Thévenin (13)

Affiliations

((1) Department of Physics and Astronomy, Iowa State University, Ames, IA, USA, (2) Department of Physics, Florida State University, Tallahassee, FL, USA, (3) Gemini Observatory, NSF's National Optical-Infrared Astronomy Research Laboratory, Hilo, HI, USA, (4) Cerro Tololo Inter-American Observatory, NSF's National Optical-Infrared Astronomy Research Laboratory, La Serena, Chile, (5) Department of Physics and Astronomy, Dartmouth College, Hanover, NH, USA, (6) Dipartimento di Fisica, Università di Roma Tor Vergata, Roma, Italy, (7) INAF-Osservatorio Astronomico di Roma, Monte Porzio Catone, Italy, (8) Instituto de Astrofísica de Canarias, La Laguna, Tenerife, Spain, (9) INAF-Osservatorio Astronomico di Capodimonte, Napoli, Italy, (10) INAF-Osservatorio Astronomico di Padova, Padova, Italy, (11) Space Science Data Center, Roma, Italy, (12) Departmento de Astrofísica, Universidad de La Laguna, La Laguna, Tenerife, Spain, (13) Université de Nice Sophia-antipolis, CNRS, Observatoire de la Côte d'Azur, Laboratoire Lagrange, Nice, France)

4.1 Abstract

We present new empirical infrared Period-Luminosity-Metallicity (PLZ) and Period-Wesenheit-Metallicity (PWZ) relations for RR Lyrae based on the latest Gaia EDR3 parallaxes. The relations are provided in the WISE $W1$ and $W2$ bands, as well as in the $W(W1, V - W1)$ and $W(W2, V - W2)$ Wesenheit magnitudes. The relations are calibrated using a very large sample of Galactic halo field RR Lyrae stars with homogeneous spectroscopic [Fe/H] abundances (over 1,000 stars in the $W1$ band), covering a broad range of metallicities $(-2.5 \lesssim [\mathrm{Fe/H}] \lesssim 0.0)$. We test the performance of our PLZ and PWZ relations by determining the distance moduli of both galactic and extragalactic stellar associations: the Sculptor dwarf spheroidal galaxy in the Local Group (finding $\bar{\mu}_0 = 19.47 \pm 0.06$), the Galactic globular clusters M4 ($\bar{\mu}_0 = 11.16 \pm 0.05$) and the Reticulum globular cluster in the Large Magellanic Cloud ($\bar{\mu}_0 = 18.23 \pm 0.06$). The distance moduli determined through all our relations are internally self-consistent (within $\lesssim 0.05$ mag) but are systematically smaller (by $\sim 2\text{-}3\sigma$) than previous literature measurements taken from a variety of methods/anchors. However, a comparison with similar recent RR Lyrae empirical relations anchored with EDR3 likewise shows to varying extents a systematically smaller distance modulus for PLZ/PWZ RR Lyrae relations.

4.2 Introduction

RR Lyrae stars (RRLs) have been extensively utilized as a primary standard candle within our Local Group of galaxies. They are easily identifiable, with a period between 0.2 and 1 day, and are found nearly everywhere due to being evolved $\sim$0.7 solar mass stars. As such, RRLs are the most widely used tracers of old (age $\gtrsim$ 10 Gyr, Savino et al. 2020; Walker 1989) stellar populations in the local neighborhood (see, e.g., Bono et al. 2016 and Catelan and Smith 2015 for a review). Besides their use in probing galactic structures, an accurate calibration of RRL distances allows for a cosmological distance ladder completely based on Population II stars, independent from Classical Cepheids. This has assumed great relevance over the last decade due

to the current tension in measured values of the Hubble constant, which is still mainly anchored on classical Cepheids (see Riess et al. 2022).

RRLs were first used as standard candles due to their evolutionary position on the Horizontal Branch (HB) yielding a nearly constant V-band magnitude, with a minor metallicity dependence (Baade, 1958). This correlation ultimately leads to a well-defined M_V vs. iron abundance relation (Caputo, 1998; Sandage, 1990); however, in its simplicity, this relation overlooks evolutionary effects on the HB and is prone to errors in accounting for extinction and possible non-linearities (Bono et al., 2003). While brightness in the V-band does not show any significant dependence on the period, Period-Luminosity-Metallicity relations (PLZ) do exist in the infrared (see e.g. Marconi et al. (2015); Neeley et al. (2017) for theoretical relations, and Dambis et al. (2013); Gilligan et al. (2021); Madore et al. (2013); Muraveva et al. (2018a); Neeley et al. (2019) for observational ones). These PLZ relations have an accuracy approaching other traditional stellar standard candles that can be characterized by a Leavitt Law (Leavitt, 1908; Leavitt and Pickering, 1912), such as Cepheids. The accuracy improves for the RRL PLZ relationships when moving to the infrared as both the importance of accounting for reddening decreases and the dispersion of the PLZ itself decreases, due in part to the dependence on metallicity increasing and the pulsational amplitude decreasing with longer wavelengths. Moving to the infrared minimizes temperature effects, as infrared RRL observations are mostly determined by the radius variation during the star's pulsation rather than the effective temperature changes that dominate in the optical wavelengths (Bono et al., 2016). We can similarly combine optical bands to create a Wesenheit magnitude that by construction is reddening independent, as well as less susceptible to temperature effects. These magnitudes can be effectively used in Period-Wesenheit-Metallicity relations (PWZ), in lieu of an infrared PLZ (Marconi et al., 2015).

Until recently, PLZ and PWZ relations were limited in their applications due to the scarcity of accurate high-resolution (HR, R $\gtrsim$ 20,000) spectroscopic metallicity measurements, capable of providing accuracy of $\sim$ 0.1 dex in [Fe/H] for individual RRL. Indeed, these relations have been predominantly based on RRL residing in globular clusters (GCs) with well-studied cluster

metallicity. The age of large area photometric time surveys (e.g., ASAS-SN (Jayasinghe et al., 2018; Shappee et al., 2014), Catalina Sky Survey (Drake et al., 2009), PanSTARRS (Chambers et al., 2016), DES (Abbott et al., 2018), Gaia (Clementini et al., 2016, 2019), TESS (Ricker et al., 2015), ZTF (Bellm et al., 2019), OGLE (Szymanski, 2005)), have, however, heralded a new age where large samples of RRL variables, especially in the field of the Galactic Halo and Bulge, are finally available. Using effectively these new RRL catalogs, however, still requires knowing their metallicities, which can be prohibitive if it requires taking spectra of such a large number of targets. This issue can be avoided if the metallic abundance for these stars could be estimated by studying the properties of their light curves, without the need of collecting their spectra. With this motivation in mind, in Mullen et al. 2021 (hereafter Paper I) and Mullen et al. 2022 (hereafter Paper II) we have provided new relations to derive photometric metallicities of fundamental and overtone RRL stars respectively, based on their optical V-band and infrared (WISE W1 and W2 bands, Wright et al. 2010) light curves. The distinction of our relations from other available photometric metallicities is that they are based on the largest available sample of homogeneous spectroscopic metallicities available to date (over 9,000 RRLs), which we published in Crestani et al. (2021) (C21 hereafter) and in Fabrizio et al. (2021). In this paper we expand on our previous work by providing PLZ and PWZ relations based on the same sample of calibrating RRLs. Metallicities for this sample are still derived from C21. Distances are instead obtained from the most recent Gaia EDR3 parallax values (Gaia Collaboration et al., 2022). At the time of this publication, there have already been some Gaia EDR3 distance calibrations using either smaller calibration samples or different bands/relations than those presented in this work (e.g., Garofalo et al. 2022; Gilligan et al. 2021; Li et al. 2022). Overall, the relations presented in this work are based on the largest available calibrating sample with individual spectroscopic metallicities obtained on a homogeneous scale, and as such they allow for studying the dependence of PLZ and PWZs over the entire [Fe/H] abundance range in the Galaxy.

This paper is structured as follows. In Section 4.3, we describe the data sets we adopt for our work: the metallicity catalog utilizing the work of C21, derivation of mean magnitudes from

optical and infrared time-series, and the Gaia parallax measurements. In Section 4.4, we explain how our PLZ/PWZ relations are obtained and calibrated. Section 4.5 assesses the precision of the Wesenheit and infrared relations as we apply our method to derive the distance modulus to M4 (a Galactic globular cluster), Reticulum (a globular cluster in the Large Magellanic Cloud), and Sculptor (a Local Group dwarf spheroidal galaxy) and compare our distance moduli with previous literature measurements. Our conclusions are presented in Section 4.6.

4.3   Datasets

Our calibration sample of RRLs is chosen from an extensive catalog of 8660 field RRLs, from which we have either [Fe/H] abundances derived from HR spectra ($R \gtrsim 20{,}000$) or an estimate of their metallicity based on the ΔS method (Preston, 1959). This HR+ΔS metallicity catalog is comprised of both the high-resolution metallicity catalog of C21 and the application of the spectrum selection criteria and ΔS metallicity calibration of C21 (applied in Fabrizio et al. 2021) to the full medium-resolution ($R \sim 2{,}000$) Large Scale Area Multi-Object Spectroscopic Telescope (LAMOST) DR2 survey (Deng et al., 2012; Liu et al., 2014) and Sloan Extension for Galactic Understanding and Exploration (SEGUE, Yanny et al., 2009) datasets. By utilizing metallicity measurements from the single work of C21, we ensure our entire sample is on a homogeneous metallicity scale (consistent with the globular cluster metallicity scale provided by Carretta et al. 2009). For a complete and detailed description of the metallicity scale, the HR metallicity catalog's demographics, the ΔS calibration, and the spectrum selection criteria, we refer the reader to the C21 paper.

The resultant HR+ΔS metallicity catalog was cross-matched with the *Gaia* EDR3 database (Fabricius et al., 2021; Gaia Collaboration et al., 2021; Lindegren et al., 2021b) to provide astrometric data. Finally, photometry is obtained by cross-matching the variables in our metallicity catalog with both the Wide-field Infrared Survey Explorer (WISE, Wright et al. 2010), and its Near-Earth Objects reactivation mission (NEOWISE, Mainzer et al. 2011) in the 3.4 and 4.6 μm bands, $W1$, and $W2$ respectively. Similarly, visible time-series photometric measurements

in the V band were taken from the All-Sky Automated Survey for Supernovae (ASAS-SN, Jayasinghe et al. 2018; Shappee et al. 2014). For a more detailed description of the NEOWISE, ASAS-SN survey and how we have integrated such measurements to our calibration sample, we refer the reader to Paper I and Paper II.

To compute new PLZ relationships, periods and mean magnitudes of this sample were derived by following the procedure from Paper I, summarized below. The period of each RRL star was refined using the Lomb-Scargle method (Lomb, 1976; Scargle, 1982) applied to the ASAS-SN and WISE time series data. The surveys' large temporal baseline ($\gtrsim 8$ years) allows us to determine well-defined periods with average accuracy on the order of $\sim 10^{-6}$ days, which properly phase the data without any readily detectable shifting in phase. Mean magnitudes for each band were determined by applying a Gaussian locally-weighted regression smoothing (GLOESS) algorithm to the phased data to gain a smoothed light curve. Each RRL star's mean magnitude is determined by integrating the smoothed light curve flux over one period, then subsequently converting back into magnitude. For more specifics on the GLOESS algorithm and the calculation of mean magnitude from a GLOESS light curve with its uncertainty, we refer you to Persson et al. (2004) or Neeley et al. (2015), respectively.

To ensure a clean sample of RRLs, a number of quality cuts were made on the input catalog. We first implement the various quality checks on light curve quality and data extraction as elaborated upon in Paper I. Quality checks include: comparing refined period to that of literature, defining the maximum allowable scatter around the GLOESS light curve, and implementing iterative rounds of outlier rejection for individual epochs relative to the GLOESS phased lightcurve. Furthermore, in order to eliminate possible contact eclipsing binary (W UMa) from our dataset, whose sinusoidal light curves can often be confused with the light curves of first overtone RRL, we required all the RRL in our sample to have photometric measurements in both V and $W1$. Following the procedure of Mullen et al. (2022) (Section 3.2), the amplitude ratio between the V and $W1$ magnitudes serves as a primary discriminator between RRL stars and eclipsing binaries. Note that this criterion does not cause any issues with sample size as the

ASAS-SN survey has nearly complete coverage ($\sim 98\%$) of the WISE stars used in this work. Subsequent quality cuts based upon astrometric criterion or due to the fitting method utilized are noted in the following section. The exact number of stars used in each calibration, after outlier rejection, is given in Table 4.1.

4.4 Calibration of PLZ and PWZ relations

Gaia EDR3 parallaxes were processed according to the recommendations in Gaia Collaboration et al. (2022). In particular, the parallaxes were corrected for the *Gaia* zero-point systematic error using the calibration of Lindegren et al. (2021a). Guided by §7.1.2 of the EDR3 documentation and Figure 19 in Fabricius et al. (2021), the uncertainty in the EDR3 parallaxes have been increased from their catalog values by $\sim 10\%$ to 60% depending on the magnitude of the star and its solution type in EDR3.

Reddenings were determined from the Lallement et al. (2019) 3-D maps. If the parallax uncertainty was less than 10% of the parallax, the distance to each star was estimated from its parallax, otherwise, the distance, as a first order approximation, was calculated from the PLZ relation of Gilligan et al. (2021) in the $W1$ band (assuming no reddening). After the initial reddening determination, the distance was recalculated and the reddening determined again. A comparison of the two reddening determinations indicated that two iterations was sufficient to lead to convergence in the reddening determination. Conversion from E(B-V) to extinction assumed $R_V = 3.1$ from Cardelli et al. (1989), and $A_{W1}/A_V = 0.061$, $A_{W2}/A_V = 0.048$ from the Yuan et al. (2013) extinctions. In the W1 sample, 93% of the stars have relatively low reddenings, with $E(B-V) < 0.2$, which corresponds to $A_{W1} < 0.038\,\mathrm{mag}$. In the W2 sample, 89% of the stars have $E(B-V) < 0.2$. The maximum reddening in the sample is $E(B-V) = 0.67$, corresponding to $A_{W1} = 0.13\,\mathrm{mag}$. Thus, uncertainties in the reddening values, considered to be $\sim 10\%$, will not significantly impact the PLZ fit.

In order to obtain a clean sample of RRLs, a number of additional quality cuts were made on the input catalog. Stars which may have spurious astrometric solutions can be identified by a

large value of the renormalised uniform weight error (RUWE, Lindegren et al., 2021b), and so only stars with $RUWE < 1.4$ were used in the fitting process ($\sim 10\%$ of RRL were removed due to this). A plot of the `astrometric_excess_noise` as a function of RUWE revealed that there were some stars which had large excess astrometric noise which had RUWE < 1.4. As a result, an additional cut of `astrometric_excess_noise` < 0.2 ($\sim 2\%$ of the data) was applied to the catalog prior to fitting the PLZ relation.

The overall properties of the data sample used to determine the PLZ relation are shown in Figure 4.1. There are over 1000 stars in the W1 sample (9% with HR spectroscopic [Fe/H]) and about 400 stars in the $W2$ sample (22% with HR [Fe/H]); Table 4.1 contains the exact sample size used for each relation. The existence of a period-luminosity (PL) relationship is clearly visible in the left panel of Figure 4.1, as RRLs with shorter periods are intrinsically less luminous than longer-period stars. Thus, at a given apparent magnitude, the stars with a shorter period have to be closer and hence have a larger parallax than stars with longer periods. The sample covers a broad [Fe/H] range, from -2.5 to 0.0 dex. Although their uncertainties are not shown in this figure, the parallaxes are of high quality ($\bar{\sigma} \approx 0.02$ mas) – there are only 48 stars in the W1 sample (all with $W1 > 13.45\,\mathrm{mag}$) which have $\varpi/\sigma_\varpi < 2$, while the lowest quality parallax in the W2 sample has $\varpi/\sigma_\varpi = 2.5$.

The PLZ calibration largely followed the procedure outlined in Gilligan et al. (2021) and Layden et al. (2019). In brief, the PLZ was fit using the Astrometric Based Luminosity (ABL) A_{m_o}, defined as:

$$\varpi 10^{0.2 m_o - 2} = 10^{0.2[a(\log P + 0.27) + b([\mathrm{Fe/H}] + 1.3) + c]} \tag{4.1}$$

where ϖ is the parallax in mas, m_o is the absorption corrected apparent magnitude, and the a, b and c are determined in the fit. The RRc stars had their period fundamentalized by adding 0.127 to $\log P$ (Braga et al., 2022; Iben and Huchra, 1971). The explicit, non-linear fit, which takes into account the uncertainties in all of the observed quantities was performed using a weighted orthogonal distance regression (Boggs et al., 1989; Zwolak et al., 2007) and the nonlinear fitting function `nls` in R (R Core Team, 2018). An intrinsic dispersion in the PLZ at constant $\log P$ and
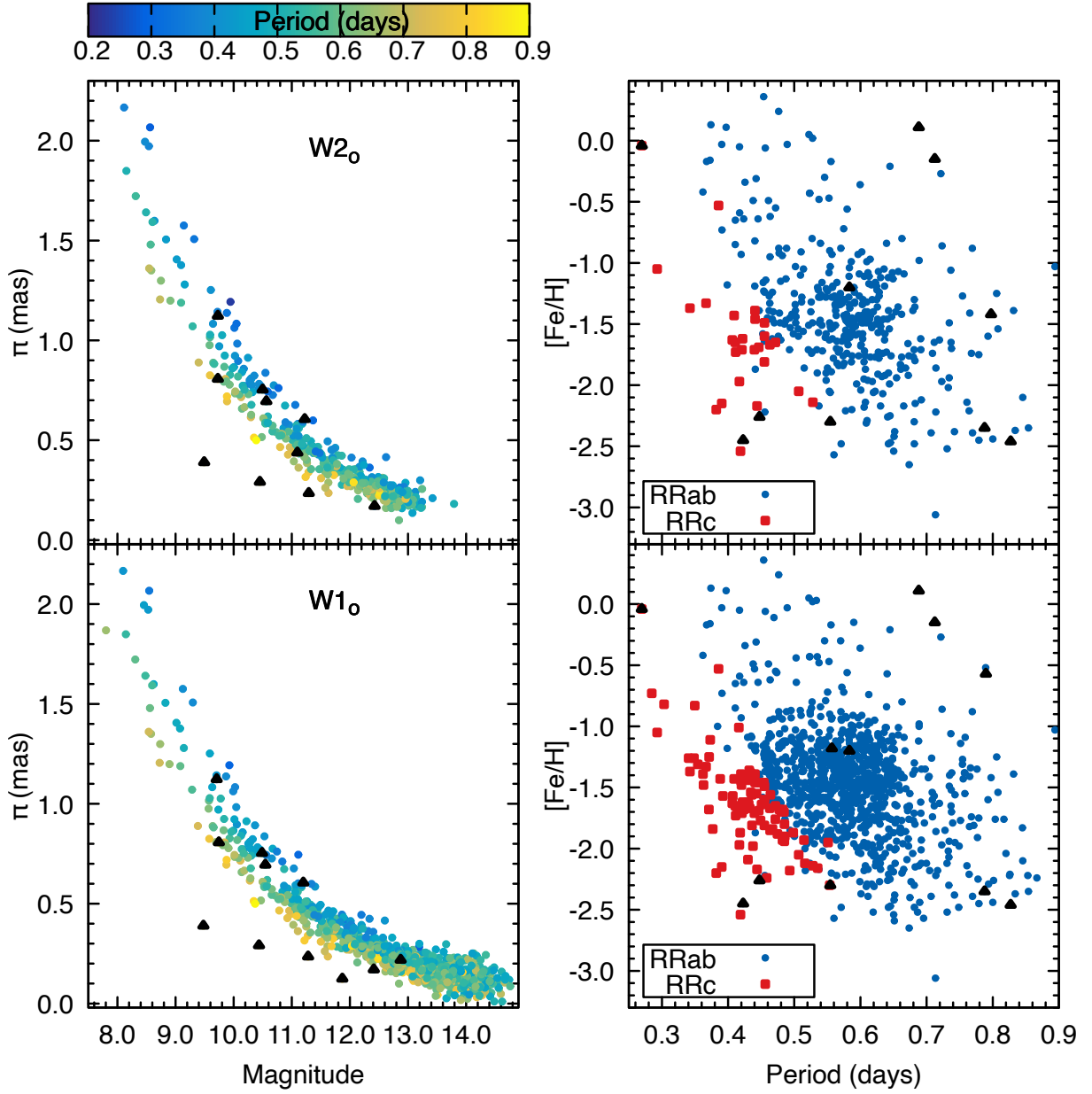
Figure 4.1   The photometric and parallax properties of the star used in the PLZ fits (left
panel), along with their Period–[Fe/H] distributions (right panel). The top
two panels show the W2 sample, while the bottom two panels show the W1
sample. Magnitudes have been dereddened, and RRc stars have had their
periods fundamentalized by adding 0.127 to log P_{FO}. The black triangles are
the stars which are more than 4σ outliers and which were discarded from the
final fit.

Table 4.1 Period-Luminosity-Metallicity and Period-Wessenheit-Metallicity relationship
coefficients, defined as $M = a(\log P + 0.27) + b([Fe/H] + 1.3) + c$. The number
of stars in a given fit is denoted by N, the assumed intrinsic dispersion in the
PLZ relation is denoted by σ_{disp} α is the color coefficient used in the Wesenheit
magnitude.

Magnitude	N	RUWE	σ_{disp}	α	a	b	c
W1	1052	< 1.4	0.02	$\cdots$	-2.44 ± 0.10	0.144 ± 0.014	-0.369 ± 0.008
W2	397	< 1.4	0.02	$\cdots$	-2.54 ± 0.10	0.151 ± 0.014	-0.367 ± 0.009
W(W1, V-W1)	1054	< 1.4	0.02	0.065	-2.55 ± 0.10	0.13 ± 0.015	-0.438 ± 0.008
W(W2, V-W2)	399	< 1.4	0.02	0.050	-2.62 ± 0.10	0.14 ± 0.015	-0.419 ± 0.009

[Fe/H] of 0.02 mag to 0.04 mag was assumed to exist in the PLZ relation during the fit process,

consistent with the intrinsic dispersion found in mono-metallicity clusters such as M4 and

Reticulum. The initial PLZ fit indicated that there were some outliers ($> 4\sigma$ residuals from the

fit) in the data. These $> 4\sigma$ outliers led to a poor fit (as judged by a quantile-quantile plot of the

fit residuals) and were removed from the fit, before the final fit was performed. As the number of

outliers was never large (at most 11 stars, which is less than 1% of the W1 sample, and less than

3% of the W2 sample) this outlier rejection did not substantially change the fit coefficients, but

did lead to a much higher fit quality and a reduced uncertainty in the fit coefficients. The results

of this fit for the $W1$ filter are illustrated in Figure 4.2. Fits for the W2 filter look similar, though

with $\sim 1/2$ the number of points.

In order to accurately estimate the uncertainties in the fitted coefficients, bootstrap

resampling was used to generate 10 000 data sets, and the fit was performed 10 000 times. The

bootstrap resampled datasets have the same number of points as the original dataset (see

Table 4.1), but the points in the dataset was selected randomly (with replacement) from the

original dataset. When picking the points for the bootstrap sample, the value of a particular

datapoint was selected from the uncertainty distribution (assuming Gaussian uncertainties in

[Fe/H], ϖ, period, magnitude and reddening) associated with that datapoint. The results of this

fitted process are summarized in Table 4.1. The distribution of the fit coefficients for the $W1$ fit is
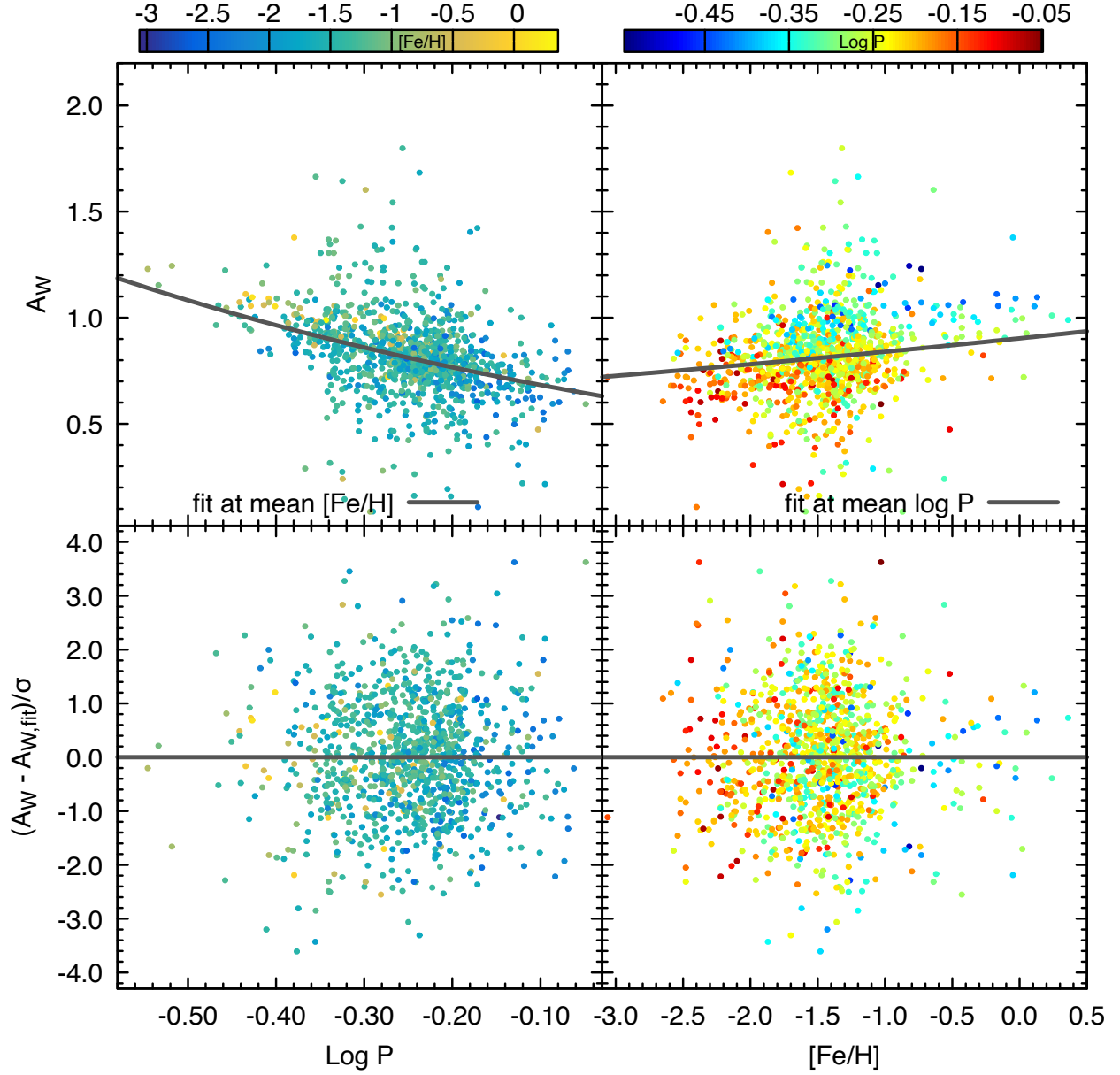
Figure 4.2   The P$W1$Z fit after the rejection of 4σ outliers. The vertical axis in the top panel is the ABL magnitude computed in the $W1$ band, $A_{W1} = \varpi 10^{0.2 m_{W1,o} - 2}$. Uncertainties A_{W1} (top panels) are not shown, but can be inferred by looking at the normalized fit residuals shown in the bottom panels. Points are colored by their [Fe/H] values in the left panels, and their $\log P$ values in the right panels.

shown in Figure 4.3. As expected, given the correlation between period and [Fe/H] in RRLs, there is a strong correlation between the log period slope and the [Fe/H] slope.

In addition to fitting PLZ relations in the $W1$ and $W2$ filters, absolute luminosity relations were also found for the reddening free Wesenheit magnitudes

$W(W1, V) = W1 - (V - W1) * 0.061/(1 - 0.061)$ and

$W(W2, V) = W2 - (V - W2) * 0.048/(1 - 0.048)$, and these fit coefficients are reported on the third and fourth line of Table 4.1. As a check to determine the sensitivity of these results to the assumed dispersion in the PLZ (at constant period and [Fe/H]) and the astrometric quality cut RUWE, the $W(W1, V)$ fit was performed for a few different values of these parameters (RUWE< 1.4 with $\sigma_{disp} = 0.04$ and RUWE< 1.2 with $\sigma_{disp} = 0.04$). The trial fitted coefficients were within 1σ of their value from the first fits; therefore, the reported fit uncertainties provide a reasonable estimate of the true uncertainties in the PLZ fits.

4.5 Distances of three stellar associations in the Milky Way and beyond

We selected three old stellar systems with multi-epoch RRL photometry available in $V, W1$, and $W2$ bands in order to test the PLZ and PWZ relations listed in Table 4.1 by measuring their distance moduli: Messier 4 (M4, NGC 6121) and Reticulum (two globular clusters, the first Galactic, and the second associated to the Large Magellanic Cloud), and the Sculptor dwarf spheroidal (dSph) galaxy in the Local Group. The three systems are between metal poor and metal intermediate, with [Fe/H] $= -1.66$ dex (Mackey and Gilmore, 2004) for Reticulum, [Fe/H] $= -1.10$ dex (see Braga et al., 2015) for M4, and [Fe/H] $= -1.85$ dex (Mullen et al., 2022) for Sculptor dSph. The three systems contain numerous known RRLs: 32 in Reticulum (Demers and Kunkel, 1976; Walker, 1992), 47 in M4 (Clement et al., 2001; Stetson et al., 2014), and 536 in Sculptor dSph (Martínez-Vázquez et al., 2016).

For this analysis, we used the mean V magnitudes published by Kuehn et al. (2013) for Reticulum, by Stetson et al. (2014) for M4, and by Martínez-Vázquez et al. (2016) in Sculptor dSph. The infrared photometry available for each system is in the Spitzer IRAC 3.6 and 4.5 μm
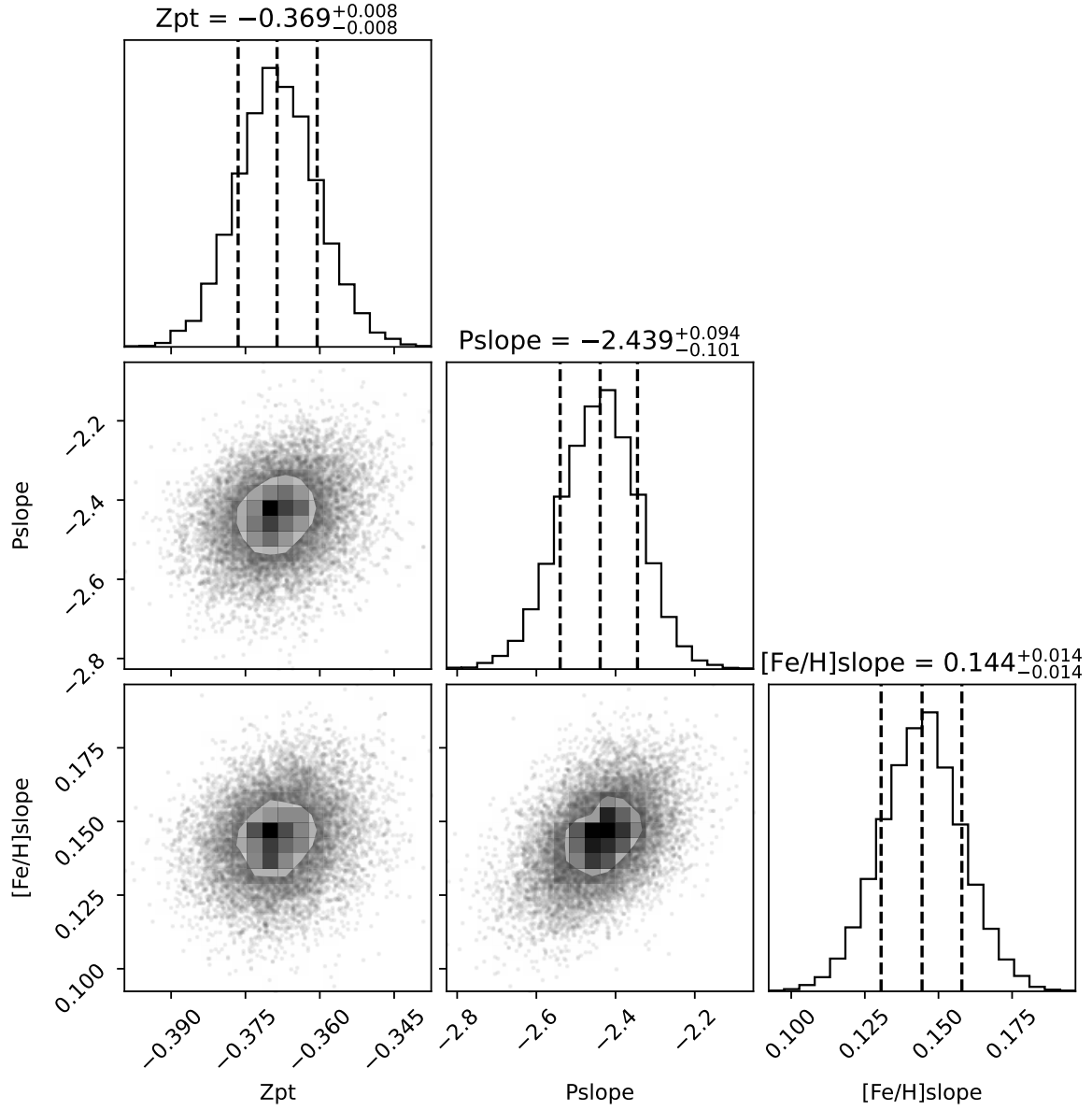
Figure 4.3   The distribution of the PW1[Fe/H] fit coefficients determined by bootstrap resampling. In the figure 'Zpt' stands for zero-point (coefficient c in Table 4.1); 'Pslope' stands for the log Period slope (coefficient a) and the slope with [Fe/H] (coefficient b) is called '[Fe/H] slope'.

filters (Garofalo et al., 2018; Muraveva et al., 2018b; Neeley et al., 2015, respectively), similar to $W1$ and $W2$, and showing no significant offset in mean magnitude as shown by Neeley et al. (2017). It is worth noting that only $W1$ photometry was available for Sculptor dSph, not $W2$.

For Reticulum and M4 we have derived four independent distance moduli: two of them using the $W1$ and $W2$ PLZ relations, and two more using the PWZ relations based on the $W1$ and $W2$ bands, combined with the V-band in the visible. For Sculptor dSph we only derived two distance moduli based on the $W1$ PLZ, and the V-$W1$ PWZ. For this reason we have limited out RRL samples to the stars that, in each system, have photometry in both optical and infrared bands. In addition to that, we have applied some quality criteria (described below) intended to remove outliers in the distance measurement.

For Reticulum, we followed the same methodology as in Gilligan et al. (2021) and reject from the 30 RRL stars with $V, W1$, and $W2$ measurements, those stars that Muraveva et al. (2018b) does not include in their calculations of the PL (i.e., V01, V08, V19, V24, V28, V32) since their position on the color-magnitude diagram is unusual or they have noisy light curves, leaving 24 RRLs in our final sample. In the case of M4, following Neeley et al. (2015), we reject two stars (V20 and V21) for being blended with nearby sources. Thus, we end up with 31 RRL stars having $W1$ mean magnitudes and 28 with $W2$ mean magnitudes. For Sculptor dSph, we only select the RRL classified by Martínez-Vázquez et al. (2016) containing both V and $W1$ photometry, ending up with 42 stars.

In order to get the true distance modulus (μ_0) from the PLZ relationships, we dereddened the $W1$ and $W2$ photometry. We adopted $E(B - V) = 0.03$ (Walker, 1992) for Reticulum, $E(B - V) = 0.37$ (Hendricks et al., 2012) for M4, and $E(B - V) = 0.018$ (Pietrzyński et al., 2008) for Sculptor dSph. The reddening was then converted into extinction in the WISE bands using the relations $A_{W1} = 0.203\, E(B - V)$ and $A_{W2} = 0.156\, E(B - V)$ (Monson et al., 2012) for Sculptor dSph and Reticulum (assuming $R_V = 3.1$). For M4, the ratio of total to selective absorption is different ($R_V = 3.62$, Hendricks et al. 2012), so we used the following extinction values, $A_{W1} = 0.251\, E(B - V)$ and $A_{W2} = 0.193\, E(B - V)$. We used these latter extinction

coefficients to update M4's α^* coefficients for the Wesenheit magnitudes, with

$\alpha^*(W1, V - W1) = 0.075$ and $\alpha^*(W2, V - W2) = 0.056$ (Gilligan et al., 2021).

The distance moduli we obtained for each system are listed in Table 4.2. The quoted uncertainties are the sum of the systematic and random uncertainties of each measurement. The former are obtained by propagation of errors considering the photometric uncertainties of the mean magnitudes in V, $W1$, and $W2$, the uncertainties of the coefficients in the relationships (see Table 4.1), and the nominal uncertainties of 0.2 dex in [Fe/H] and 10^{-4} days in the period. In the case of the distances calculated from PLZ, we also take account of the uncertainty that comes from the reddening value, considered to be 10%. The random uncertainties are instead estimated from the standard error of the mean, i.e., the standard deviation divided by the square root of the number of RRL stars used to derive the distance modulus.

Table 4.2   Distance moduli of stellar systems

System	Filter	μ_0 [mag]
Reticulum	PW(W1,V-W1)	18.22±0.10
Reticulum	PW(W2,V-W2)	18.23±0.11
Reticulum	W1	18.23±0.10
Reticulum	W2	18.24±0.12
M4 (NGC 6121)	PW(W1,V-W1)	11.19±0.08
M4 (NGC 6121)	PW(W2,V-W2)	11.14±0.08
M4 (NGC 6121)	W1	11.18±0.08
M4 (NGC 6121)	W2	11.13±0.08
Sculptor dSph	PW(W1,V-W1)	19.46±0.08
Sculptor dSph	W1	19.47±0.08

Figure 4.4 compares the distance moduli calculated through this work's PLZ/PWZ relations (blue squares) to a selection of literature distance measurements from the last ten years (i.e., from 2012) for these three stellar systems. Next to each measurement, we list the method used to estimate the distance modulus; for methods based upon RRL, we also note within parentheses how the zero-point of the calibration was obtained. The error bars plotted are those given by the original study, which for some works listed are just the random errors, not accounting for

additional uncertainties such as zero-point calibration, and therefore may be underestimated. It is worth noting that the different works are based upon different methods and/or stellar calibrators. They possess different intrinsic dispersion, and sometimes they may be based on fixed assumptions such as reddening and metallicity in the case of PLZ/PWZ. We refer the reader to explore the individual references listed for full details about the calibration utilized and determined distance moduli.

Overall, the distance moduli estimated with this work's various PLZ/PWZ relations are in good agreement with each other for Reticulum (within 0.02 mag) and Sculptor dSph (within 0.01 mag) and quite similar for M4 (within 0.05 mag), with an average distance modulus (blue vertical lines in Figure 4.4) of $\bar{\mu}_0 = 18.23 \pm 0.06$ for Reticulum, $\bar{\mu}_0 = 11.16 \pm 0.05$ for M4, and $\bar{\mu}_0 = 19.47 \pm 0.06$ for Sculptor dSph. The errors noted on the average distance moduli are just the statistical error due to photometry, i.e., the uncertainty divided by the square root of the number (N) of independent bands used in the average (N=2 for Sculptor and N=3 for M4 and Reticulum). An analysis of Figure 4.4 shows that our distance moduli and those RRL relations based on an EDR3 anchor tend to be consistently smaller than other distance moduli determinations in the literature. For Reticulum, we note that the distance modulus is smaller than the LMC ($\mu_0 \approx 18.4$ mag); however, some discrepancy is expected, as Reticulum is widely separated from the center of the LMC ($\sim$11 degrees on the plane of the sky, Walker 1992). Note that only M4 is close enough to currently provide a reliable distance measurement directly from parallax. The parallax distance to M4 reported by Vasiliev and Baumgardt (2021) yields a distance modulus of 11.26 ± 0.04 mag after accounting for the individual stellar parallax corrections of Lindegren et al. (2021a) and taking into account spatially correlated systematic errors. In comparison, the EDR3 anchored RRL measurements all provide smaller distance moduli than that from astrometry, with our average M4 measurement 2σ smaller.
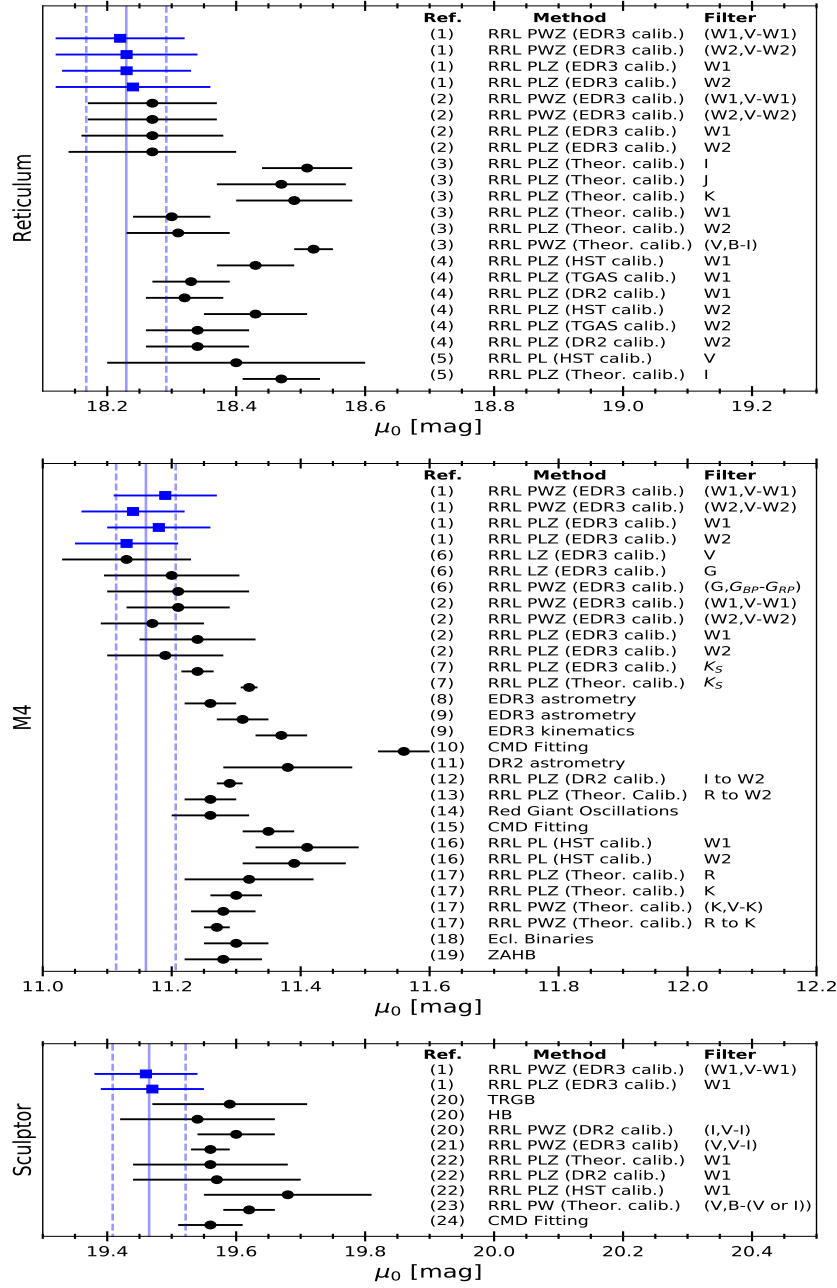
Figure 4.4   Comparison of the true distance moduli from this work (blue squares) and literature from the last decade (black circles).

The vertical lines represent the mean and statistical error (see text) of this work's measurements. Beside each measurement is listed a number corresponding to the reference used to make this figure (below), method used to estimate the distance modulus, and observation band. **References** - (1) This work; (2) Gilligan et al. 2021; (3) Braga et al. 2019; (4) Muraveva et al. 2018b; (5) Kuehn et al. 2013; (6) Garofalo et al. 2022; (7) Bhardwaj et al. 2021; (8) Vasiliev and Baumgardt 2021; (9) Baumgardt and Vasiliev 2021; (10) Valcin et al. 2020; (11) Shao and Li 2019; (12) Neeley et al. 2019; (13) Neeley et al. 2017; (14) Miglio et al. 2016; (15) Correnti et al. 2016 (16) Neeley et al. 2015; (17) Braga et al. 2015; (18) Kaluzny et al. 2013; (19) Hendricks et al. 2012; (20) Tran et al. 2022; (21) Nagarajan et al. 2021; (22) Garofalo et al. 2018; (23) Martínez-Vázquez et al. 2015; (24)Weisz et al. 2014.

Relative discrepancies between individual calibrations can partially be attributed to different assumptions in differential reddening (important with clusters such as M4) and small differences in photometric bands (such as those between IRAC and WISE). Futhermore, even in the Gaia EDR3 release, parallax measurements are still prone to bias with color and magnitude-dependent zero-point offset. Lindegren et al. (2021a), as applied, provides a first-order correction to this issue; however, the RRL stars used in our PLZ/PWZ relations possess a quite different color and magnitude than the very bright giant stars often used for direct parallax measurements of globular clusters. Note, however, that Vasiliev and Baumgardt (2021) suggests Lindegren et al. (2021a) might be overcorrecting the Gaia EDR3 parallaxes by $\varpi \sim 0.007$ mas, as applied in Baumgardt and Vasiliev (2021) yielding a slightly larger distance modulus. It will be interesting to see how future improvements to parallax corrections affect the different types of distance estimates.

In the mean time, this work corroborates the growing trend of EDR3 anchored RRL distance measurements yielding smaller distance moduli, as shown in works such as Garofalo et al. (2022), Gilligan et al. (2021), Nagarajan et al. (2021), and Bhardwaj et al. (2021). In Figure 4.5, we analyze the relative difference between the average distance moduli for M4, Reticulum, and Sculptor calculated in this work and three categories of calibrators: those marked in Figure 4.4 as *DR2 calib.* (Garofalo et al., 2018; Muraveva et al., 2018b; Neeley et al., 2019; Tran et al., 2022), *HST calib.*(Garofalo et al., 2018; Kuehn et al., 2013; Muraveva et al., 2018b; Neeley et al., 2015), or *EDR3 calib.* from other works (Bhardwaj et al., 2021; Garofalo et al., 2022; Gilligan et al., 2021; Nagarajan et al., 2021). For all stellar systems, we note a decreasing offset from the HST
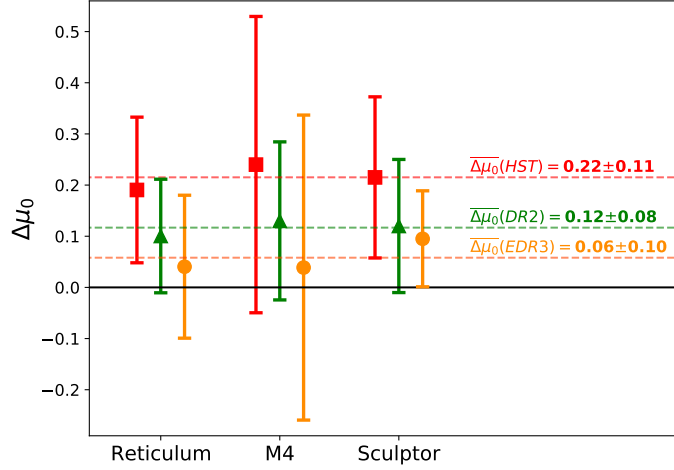
Figure 4.5   The difference in distance moduli between the average literature measurement of those marked in Figure 4.4 as either HST calibration (red squares), DR2 calib. (green triangles), or EDR3 calib. (yellow circles) and that of this work for three stellar systems: M4, Reticulum, and Sculptor. Errors are propagated from the error in the average distance moduli of this work added in quadrature with the average error of the literature moduli for each calibration type. Horizontal lines represent the average relative distance moduli across all three systems for each type of calibrator used.

calibrations ($\overline{\Delta\mu_0} = 0.22 \pm 0.11$ mag) to DR2 calibrations ($\overline{\Delta\mu_0} = 0.12 \pm 0.08$ mag) and continuing to other EDR3 calibrations ($\overline{\Delta\mu_0} = 0.06 \pm 0.10$ mag, consistent with our work). We regard the offset in distance moduli as a difference with the zero-point between the different calibrators. By doing this check, we also show that the systematically smaller EDR3 distances appear to be unrelated to the choice of metallicity term in individual PLZ calibrations, as we see the same trend across all three systems.

4.6   Conclusions

In this work, we provide new empirical PLZ/PWZ relations using infrared ($W1$ and $W2$ band) and optical (V band) photometry based on the latest Gaia EDR3 parallaxes. Our relations are calibrated using an entirely field RRL-based sample of both RRab and fundamentalized RRc variables for which homogeneous spectroscopic abundances are available and cover a broad range

of metallicities ($-2.5 \lesssim$ [Fe/H] $\lesssim 0.0$) derived from HR spectra and the ΔS method, using techniques developed by C21. We derive the period and mean magnitudes used in our calibration directly from the densely populated/ long temporal baselines of the ASASSN and WISE surveys, ensuring a uniform calibration sample. Furthermore, our work utilized the homogeneous processing and quality criterion of Mullen+2021 and Mullen+2022 to uniformly derive the period and mean magnitude, thereby ensuring homogeneity through all of our calibrating variables and a clean sample of RRL stars in ASSASN and WISE surveys. Our overall sample contained $\sim$1000 stars with W1 band magnitudes and $\sim$400 stars in W2, from which we applied Markov chain Monte Carlo to derive our PLZ/PWZ relations.

In order to test the performance of our newly derived PLZ and PWZ relations, we determine distance moduli to the Sculptor dwarf spheroidal galaxy (finding $\bar{\mu}_0 = 19.47 \pm 0.06$) and the globular clusters M4 ($\bar{\mu}_0 = 11.16 \pm 0.05$) and Reticulum ($\bar{\mu}_0 = 18.23 \pm 0.06$). The distance moduli determined through all of our relations are internally self-consistent (within $\lesssim 0.05$ mag). A comparison with previous literature measurements taken from a variety of methods/anchors reveals that our distance moduli are systematically smaller (by up to $\sim$ 2-3σ). Compared to direct EDR3 parallax measurements, our RRL EDR3-based PLZ/PWZ distance to M4 has a $\sim$0.1 mag smaller distance modulus. Similarly, other RRL EDR3 anchored calibrations all likewise show to varying extents a systematically smaller distance modulus for the RRL relations when compared to EDR3 parallaxes. We analyze the difference between the average distance moduli for HST, Gaia DR2, and Gaia DR3 calibrations for each of our stellar systems and note across each system a consistent offset relative to this work of $\overline{\Delta\mu_0}(HST) = 0.22 \pm 0.11$ mag and $\overline{\Delta\mu_0}(DR2) = 0.12 \pm 0.08$ mag. This suggests that the differences in distance moduli noted are not due to any selection bias in the metallicity term of the PLZ and point towards biases in distance moduli based upon what is used as the zero-point in the PLZ calibrations.

4.7   References

Abbott, T.M.C., Abdalla, F.B., Allam, S. et al (2018). The Dark Energy Survey: Data Release 1. *The Astrophysical Journal Supplement Series*, 239(2):18.

Baade, W. (1958). Galaxies and their Stellar Populations. (A Review of the Present State of Affairs). *Ricerche Astronomiche*, 5:3.

Baumgardt, H. and Vasiliev, E. (2021). Accurate distances to Galactic globular clusters through a combination of Gaia EDR3, HST, and literature data. *Monthly Notices of the Royal Astronomical Society*, 505(4):5957–5977.

Bellm, E.C., Kulkarni, S.R., Graham, M.J. et al (2019). The Zwicky Transient Facility: System Overview, Performance, and First Results. *Publications of the ASP*, 131(995):018002.

Bhardwaj, A., Rejkuba, M., de Grijs, R. et al (2021). RR Lyrae Variables in Messier 53: Near-infrared Period-Luminosity Relations and the Calibration Using Gaia Early Data Release 3. *The Astrophysical Journal*, 909(2):200.

Boggs, P.T., Donaldson, J.R., Byrd, R.h. et al (1989). Algorithm 676: Odrpack: Software for weighted orthogonal distance regression. *ACM Trans. Math. Softw.*, 15(4):348–364.

Bono, G., Braga, V.F., Pietrinferni, A. et al (2016). Classical Cepheids and RR Lyrae stars: similar, but not too much. *Mem. Societa Astronomica Italiana*, 87:358.

Bono, G., Caputo, F., Castellani, V. et al (2003). A pulsational approach to near-infrared and visual magnitudes of RR Lyr stars. *Monthly Notices of the Royal Astronomical Society*, 344(4):1097–1106.

Braga, V.F., Dall'Ora, M., Bono, G. et al (2015). On the Distance of the Globular Cluster M4 (NGC 6121) Using RR Lyrae Stars. I. Optical and Near-infrared Period-Luminosity and Period-Wesenheit Relations. *The Astrophysical Journal*, 799(2):165.

Braga, V.F., Fiorentino, G., Bono, G. et al (2022). On the use of field RR lyrae as galactic probes. VI. Mixed mode RR Lyrae variables in Fornax and in nearby dwarf galaxies. *Monthly Notices of the Royal Astronomical Society*.

Braga, V.F., Stetson, P.B., Bono, G. et al (2019). New near-infrared JHK_s light-curve templates for RR lyrae variables. *Astronomy & Astrophysics*, 625:A1.

Caputo, F. (1998). Evolution of Population II stars. *Astronomy and Astrophysics Reviews*, 9(1-2):33–61.

Cardelli, J.A., Clayton, G.C. and Mathis, J.S. (1989). The Relationship between Infrared, Optical, and Ultraviolet Extinction. *The Astrophysical Journal*, 345:245.

Carretta, E., Bragaglia, A., Gratton, R. et al (2009). Intrinsic iron spread and a new metallicity scale for globular clusters. *Astronomy and Astrophysics*, 508(2):695–706.

Catelan, M. and Smith, H.A. (2015). *Pulsating Stars*.

Chambers, K.C., Magnier, E.A., Metcalfe, N. et al (2016). The Pan-STARRS1 Surveys. *arXiv e-prints*, page arXiv:1612.05560.

Clement, C.M., Muzzin, A., Dufton, Q. et al (2001). Variable Stars in Galactic Globular Clusters. *Astronomical Journal*, 122(5):2587–2599.

Clementini, G., Ripepi, V., Leccia, S. et al (2016). Gaia Data Release 1. The Cepheid and RR Lyrae star pipeline and its application to the south ecliptic pole region. *Astronomy and Astrophysics*, 595:A133.

Clementini, G., Ripepi, V., Molinaro, R. et al (2019). Gaia Data Release 2. Specific characterisation and validation of all-sky Cepheids and RR Lyrae stars. *Astronomy and Astrophysics*, 622:A60.

Correnti, M., Gennaro, M., Kalirai, J.S. et al (2016). Constraining Globular Cluster Age Uncertainties using the IR Color-Magnitude Diagram. *The Astrophysical Journal*, 823(1):18.

Crestani, J., Fabrizio, M., Braga, V.F. et al (2021). On the Use of Field RR Lyrae as Galactic Probes. II. A New ΔS Calibration to Estimate Their Metallicity. *The Astrophysical Journal*, 908(1):20.

Dambis, A.K., Berdnikov, L.N., Kniazev, A.Y. et al (2013). RR Lyrae variables: visual and infrared luminosities, intrinsic colours and kinematics. *Monthly Notices of the Royal Astronomical Society*, 435(4):3206–3220.

Demers, S. and Kunkel, W.E. (1976). The Reticulum system: an analog to the Draco dwarf galaxy near the Large Magellanic Cloud. *The Astrophysical Journal*, 208:932.

Deng, L.C., Newberg, H.J., Liu, C. et al (2012). LAMOST Experiment for Galactic Understanding and Exploration (LEGUE) — The survey's science plan. *Research in Astronomy and Astrophysics*, 12(7):735–754.

Drake, A.J., Djorgovski, S.G., Mahabal, A. et al (2009). First Results from the Catalina Real-Time Transient Survey. *The Astrophysical Journal*, 696(1):870–884.

Fabricius, C., Luri, X., Arenou, F. et al (2021). Gaia Early Data Release 3. Catalogue validation. *Astronomy and Astrophysics*, 649:A5.

Fabrizio, M., Braga, V.F., Crestani, J. et al (2021). On the Use of Field RR Lyrae As Galactic Probes: IV. New Insights Into and Around the Oosterhoff Dichotomy. *The Astrophysical Journal*, 919(2):118.

Gaia Collaboration, Brown, A.G.A., Vallenari, A. et al (2021). Gaia Early Data Release 3. Summary of the contents and survey properties. *Astronomy and Astrophysics*, 649:A1.

Gaia Collaboration, Vallenari, A., Brown, A.G.A. et al (2022). Gaia Data Release 3: Summary of the content and survey properties. *arXiv e-prints*, page arXiv:2208.00211.

Garofalo, A., Delgado, H.E., Sarro, L.M. et al (2022). New LZ and PW(Z) relations of RR Lyrae stars calibrated with Gaia EDR3 parallaxes. *Monthly Notices of the Royal Astronomical Society*, 513(1):788–806.

Garofalo, A., Scowcroft, V., Clementini, G. et al (2018). SMHASH: a new mid-infrared RR Lyrae distance determination for the Local Group dwarf spheroidal galaxy Sculptor. *Monthly Notices of the Royal Astronomical Society*, 481(1):578–595.

Garofalo, A., Scowcroft, V., Clementini, G. et al (2018). SMHASH: a new mid-infrared RR Lyrae distance determination for the Local Group dwarf spheroidal galaxy Sculptor. *Monthly Notices of the Royal Astronomical Society*, 481(1):578–595.

Gilligan, C.K., Chaboyer, B., Marengo, M. et al (2021). Metallicities from high-resolution spectra of 49 RR Lyrae variables. *Monthly Notices of the Royal Astronomical Society*, 503(4):4719–4733.

Hendricks, B., Stetson, P.B., VandenBerg, D.A. et al (2012). A New Reddening Law for M4. *Astronomical Journal*, 144(1):25.

Iben, I., J. and Huchra, J. (1971). Comments on the Instability Strip for Halo Population Variables. *Astronomy and Astrophysics*, 14:293.

Jayasinghe, T., Kochanek, C.S., Stanek, K.Z. et al (2018). The ASAS-SN catalogue of variable stars I: The Serendipitous Survey. *Monthly Notices of the Royal Astronomical Society*, 477(3):3145–3163.

Kaluzny, J., Thompson, I.B., Rozyczka, M. et al (2013). The Cluster AgeS Experiment (CASE). V. Analysis of Three Eclipsing Binaries in the Globular Cluster M4. *Astronomical Journal*, 145(2):43.

Kuehn, C.A., Dame, K., Smith, H.A. et al (2013). Variable Stars in Large Magellanic Cloud Globular Clusters. III. Reticulum. *Astronomical Journal*, 145(6):160.

Lallement, R., Babusiaux, C., Vergely, J.L. et al (2019). Gaia-2MASS 3D maps of Galactic interstellar dust within 3 kpc. *Astronomy and Astrophysics*, 625:A135.

Layden, A.C., Tiede, G.P., Chaboyer, B. et al (2019). Infrared K-band Photometry of Field RR Lyrae Variable Stars. *Astronomical Journal*, 158(3):105.

Leavitt, H.S. (1908). 1777 variables in the Magellanic Clouds. *Annals of Harvard College Observatory*, 60:87–108.3.

Leavitt, H.S. and Pickering, E.C. (1912). Periods of 25 Variable Stars in the Small Magellanic Cloud. *Harvard College Observatory Circular*, 173:1–3.

Li, X.Y., Huang, Y., Liu, G.C. et al (2022). Photometric metallicity and distance estimates for $\sim$ 136,000 rr lyrae stars from gaia dr3.

Lindegren, L., Bastian, U., Biermann, M. et al (2021a). Gaia Early Data Release 3. Parallax bias versus magnitude, colour, and position. *Astronomy and Astrophysics*, 649:A4.

Lindegren, L., Klioner, S.A., Hernández, J. et al (2021b). Gaia Early Data Release 3. The astrometric solution. *Astronomy and Astrophysics*, 649:A2.

Liu, X.W., Yuan, H.B., Huo, Z.Y. et al (2014). LSS-GAC - A LAMOST Spectroscopic Survey of the Galactic Anti-center. In Feltzing, S., Zhao, G., Walton, N.A. et al, editors, *Setting the scene for Gaia and LAMOST*, volume 298 of *IAU Symposium*, pages 310–321.

Lomb, N.R. (1976). Least-Squares Frequency Analysis of Unequally Spaced Data. *Astrophysics and Space Science*, 39(2):447–462.

Mackey, A.D. and Gilmore, G.F. (2004). Photometry of Magellanic Cloud clusters with the Advanced Camera for Surveys - I. The old Large Magellanic Cloud clusters NGC 1928, 1939 and Reticulum. *Monthly Notices of the Royal Astronomical Society*, 352(1):153–167.

Madore, B.F., Hoffman, D., Freedman, W.L. et al (2013). A Preliminary Calibration of the RR Lyrae Period-Luminosity Relation at Mid-infrared Wavelengths: WISE Data. *The Astrophysical Journal*, 776(2):135.

Mainzer, A., Bauer, J., Grav, T. et al (2011). Preliminary Results from NEOWISE: An Enhancement to the Wide-field Infrared Survey Explorer for Solar System Science. *The Astrophysical Journal*, 731(1):53.

Marconi, M., Coppola, G., Bono, G. et al (2015). On a New Theoretical Framework for RR Lyrae Stars. I. The Metallicity Dependence. *The Astrophysical Journal*, 808(1):50.

Martínez-Vázquez, C.E., Monelli, M., Bono, G. et al (2015). Variable stars in Local Group Galaxies - I. Tracing the early chemical enrichment and radial gradients in the Sculptor dSph with RR Lyrae stars. *Monthly Notices of the Royal Astronomical Society*, 454(2):1509–1516.

Martínez-Vázquez, C.E., Monelli, M., Gallart, C. et al (2016). Probing the early chemical evolution of the Sculptor dSph with purely old stellar tracers. *Monthly Notices of the Royal Astronomical Society: Letters*, 461(1):L41–L45.

Miglio, A., Chaplin, W.J., Brogaard, K. et al (2016). Detection of solar-like oscillations in relics of the Milky Way: asteroseismology of K giants in M4 using data from the NASA K2 mission. *Monthly Notices of the Royal Astronomical Society*, 461(1):760–765.

Monson, A.J., Freedman, W.L., Madore, B.F. et al (2012). The Carnegie Hubble Program: The Leavitt Law at 3.6 and 4.5 μm in the Milky Way. *The Astrophysical Journal*, 759(2):146.

Mullen, J.P., Marengo, M., Martínez-Vázquez, C.E. et al (2021). Metallicity of Galactic RR Lyrae from Optical and Infrared Light Curves. I. Period-Fourier-Metallicity Relations for Fundamental-mode RR Lyrae. *The Astrophysical Journal*, 912(2):144.

Mullen, J.P., Marengo, M., Martínez-Vázquez, C.E. et al (2022). Metallicity of galactic rr lyrae from optical and infrared light curves: Ii. period-fourier-metallicity relations for first overtone rr lyrae.

Muraveva, T., Delgado, H.E., Clementini, G. et al (2018a). RR Lyrae stars as standard candles in the Gaia Data Release 2 Era. *Monthly Notices of the Royal Astronomical Society*, 481(1):1195–1211.

Muraveva, T., Garofalo, A., Scowcroft, V. et al (2018b). The Carnegie RR Lyrae Program: mid-infrared period-luminosity relations of RR Lyrae stars in Reticulum. *Monthly Notices of the Royal Astronomical Society*, 480(3):4138–4153.

Nagarajan, P., Weisz, D.R. and El-Badry, K. (2021). RR Lyrae-based Distances for 39 Nearby Dwarf Galaxies Calibrated to Gaia eDR3. *arXiv e-prints*, page arXiv:2111.06899.

Neeley, J.R., Marengo, M., Bono, G. et al (2017). On a New Theoretical Framework for RR Lyrae Stars. II. Mid-infrared Period-Luminosity-Metallicity Relations. *The Astrophysical Journal*, 841(2):84.

Neeley, J.R., Marengo, M., Bono, G. et al (2015). On the Distance of the Globular Cluster M4 (NGC 6121) Using RR Lyrae Stars. II. Mid-infrared Period-luminosity Relations. *The Astrophysical Journal*, 808(1):11.

Neeley, J.R., Marengo, M., Freedman, W.L. et al (2019). Standard Galactic field RR Lyrae II: a Gaia DR2 calibration of the period-Wesenheit-metallicity relation. *Monthly Notices of the Royal Astronomical Society*, 490(3):4254–4270.

Persson, S.E., Madore, B.F., Krzemiński, W. et al (2004). New Cepheid Period-Luminosity Relations for the Large Magellanic Cloud: 92 Near-Infrared Light Curves. *Astronomical Journal*, 128(5):2239–2264.

Pietrzyński, G., Gieren, W., Szewczyk, O. et al (2008). The Araucaria Project: the Distance to the Sculptor Dwarf Spheroidal Galaxy from Infrared Photometry of RR Lyrae Stars. *Astronomical Journal*, 135(6):1993–1997.

Preston, G.W. (1959). A Spectroscopic Study of the RR Lyrae Stars. *The Astrophysical Journal*, 130:507.

R Core Team (2018). *R: A Language and Environment for Statistical Computing*. R Foundation for Statistical Computing, Vienna, Austria.

Ricker, G.R., Winn, J.N., Vanderspek, R. et al (2015). Transiting Exoplanet Survey Satellite (TESS). *Journal of Astronomical Telescopes, Instruments, and Systems*, 1:014003.

Riess, A.G., Breuval, L., Yuan, W. et al (2022). Cluster Cepheids with High Precision Gaia Parallaxes, Low Zeropoint Uncertainties, and Hubble Space Telescope Photometry. *arXiv e-prints*, page arXiv:2208.01045.

Sandage, A. (1990). The Vertical Height of the Horizontal Branch: The Range in the Absolute Magnitudes of RR Lyrae Stars in a Given Globular Cluster. *The Astrophysical Journal*, 350:603.

Savino, A., Koch, A., Prudil, Z. et al (2020). The age of the Milky Way inner stellar spheroid from RR Lyrae population synthesis. *Astronomy and Astrophysics*, 641:A96.

Scargle, J.D. (1982). Studies in astronomical time series analysis. II. Statistical aspects of spectral analysis of unevenly spaced data. *The Astrophysical Journal*, 263:835–853.

Shao, Z. and Li, L. (2019). Gaia parallax of Milky Way globular clusters - A solution of mixture model. *Monthly Notices of the Royal Astronomical Society*, 489(3):3093–3101.

Shappee, B.J., Prieto, J.L., Grupe, D. et al (2014). The Man behind the Curtain: X-Rays Drive the UV through NIR Variability in the 2013 Active Galactic Nucleus Outburst in NGC 2617. *The Astrophysical Journal*, 788(1):48.

Stetson, P.B., Braga, V.F., Dall'Ora, M. et al (2014). Optical and Near-Infrared UBVRIJHK Photometry for the RR Lyrae Stars in the Nearby Globular Cluster M4 (NGC 6121). *Publications of the ASP*, 126(940):521.

Szymanski, M.K. (2005). The Optical Gravitational Lensing Experiment. Internet Access to the OGLE Photometry Data Set: OGLE-II BVI maps and I-band data. *Acta Astronomica*, 55:43–57.

Tran, Q.H., Hoyt, T.J., Freedman, W.L. et al (2022). Distances to Local Group Galaxies via Population II, Stellar Distance Indicators I: The Sculptor Dwarf Spheroidal. *arXiv e-prints*, page arXiv:2205.08548.

Valcin, D., Bernal, J.L., Jimenez, R. et al (2020). Inferring the age of the universe with globular clusters. *Journal of Cosmology and Astroparticle Physics*, 2020(12):002–002.

Vasiliev, E. and Baumgardt, H. (2021). Gaia EDR3 view on galactic globular clusters. *Monthly Notices of the Royal Astronomical Society*, 505(4):5978–6002.

Walker, A.R. (1989). A Survey for RR Lyrae Variables in Five Small Magellanic Cloud Clusters. *Publications of the ASP*, 101:570.

Walker, A.R. (1992). The LMC Cluster GLC 0435-59 (Reticulum): Photometry of the RR Lyraes and a Color-Magnitude Diagram. *Astronomical Journal*, 103:1166.

Weisz, D.R., Dolphin, A.E., Skillman, E.D. et al (2014). The Star Formation Histories of Local Group Dwarf Galaxies. I. Hubble Space Telescope/Wide Field Planetary Camera 2 Observations. *The Astrophysical Journal*, 789(2):147.

Wright, E.L., Eisenhardt, P.R.M., Mainzer, A.K. et al (2010). The Wide-field Infrared Survey Explorer (WISE): Mission Description and Initial On-orbit Performance. *Astronomical Journal*, 140(6):1868–1881.

Yanny, B., Rockosi, C., Newberg, H.J. et al (2009). SEGUE: A Spectroscopic Survey of 240,000 Stars with g = 14-20. *Astronomical Journal*, 137(5):4377–4399.

Yuan, H.B., Liu, X.W. and Xiang, M.S. (2013). Empirical extinction coefficients for the GALEX, SDSS, 2MASS and WISE passbands. *Monthly Notices of the Royal Astronomical Society*, 430(3):2188–2199.

Zwolak, J.W., Boggs, P.T. and Watson, L.T. (2007). Algorithm 869: Odrpack95: A weighted orthogonal distance regression code with bound constraints. *ACM Trans. Math. Softw.*, 33(4):27.

CHAPTER 5.   GENERAL CONCLUSION

5.1   Summary of Results

This dissertation represents the culmination of three published peer-reviewed journal articles (Mullen et al. 2021, Mullen et al. 2022, and Mullen et al. 2023) exploring the chemical and structural nature of our galactic neighborhood using photometric methods with RRLs acting as tracers of old (age> 10 Gyr) stellar populations. Through this work, I have calibrated new period-ϕ_{31}-[Fe/H] relations to provide photometric metallicities for RRab and RRc variables in the optical and, for the first time, infrared wavelengths. The relations are calibrated from an extensive sample of field RRL variables (~ 9000) for which homogeneous spectroscopic abundances are available and cover a broad range of metallicities ($-2.5 <$ [Fe/H] $\lessapprox 0.0$). These metallicities are derived from both HR spectra and the ΔS method, using techniques developed by C21. Photometric time series data of the calibration stars were extracted from the ASAS-SN (V band) and WISE (with NEOWISE extension, $W1$ and $W2$ bands) surveys. The long-temporal baselines of these surveys provide well-sampled light curves that allow for reliable Fourier expansions and accurate determination of the RRL pulsation periods (better than 10^{-6} days).

Comparisons between other optical photometric metallicity relations available in the literature show that this work's V-band relations provide reliable [Fe/H] abundances without noticeable trends over the broadest metallicity range (i.e., the entire metallicity range found in the Milky Way halo). The V-band relations consistently reproduce spectroscopic metallicities within a RMS $\simeq 0.40$ dex for RRab and $\simeq 0.30$ dex for RRc. I have also shown the existence of an intrinsic scatter in the period-ϕ_{31}-[Fe/H] plane that is often underestimated but becomes apparent with large calibration datasets covering a broad metallicity range.

By applying the V-band relations to ensembles of RRLs in galactic globular clusters, estimates of the clusters' metallicity are derived with accuracy comparable to high-resolution

spectroscopy measurements (within ± 0.08 dex). Additionally, I have shown that these relations can reproduce the [Fe/H] distribution of systems with a more complicated history of chemical enrichment, such as the Sculptor dSph, consistent with previous and independent spectroscopic and photometric predictions.

For the first time, mid-infrared period-ϕ_{31}-[Fe/H] relations (in the WISE $W1$ and $W2$ bands) have also been obtained. Despite having fewer RRLs to derive these relations, the errors obtained are similar to those in the optical. The RRab photometric and spectroscopic metallicities are consistent across the whole [Fe/H] calibration range within RMS $\simeq 0.50$ dex. The mid-infrared RRc relation has an accuracy of $\simeq 0.29$ dex in the low and moderate metallicity range ([Fe/H] $\lessgtr -0.5$ dex). In the high metallicity range, the relation appears to under-predict the [Fe/H] abundance expected from spectroscopy; further analysis (relying on a larger sample of solar-metallicity RRc calibrators) is needed to understand the root cause of this deviation. While the infrared relations are slightly less accurate than optical, they can still provide statistically representative metallicities for large ensembles of RRLs.

By combining optical and infrared photometric metallicities, it is possible to further improve the reliability of [Fe/H] measurements. The photometric relations presented here offer a good compromise between efficiency and accuracy, with uncertainties only 2 or 3 times larger than metallicities from labor-intensive line-fitting HR spectroscopy. These readily obtainable metallicities of individual RRL will be crucial in determining accurate distances with PLZ and PWZ relations, where metallicity is a key component.

This dissertation further provides new empirical PLZ/PWZ relations using infrared ($W1$ and $W2$ bands) and optical (V band) photometry based on the latest Gaia EDR3 parallaxes. These relations are calibrated using the same homogeneous field RRL-based spectroscopic abundances of C21, covering a broad range of metallicities. The homogeneous processing and quality criterion presented in the derivation of the period-ϕ_{31}-[Fe/H] relations is similarly applied here to uniformly derive the period and mean magnitude from the ASAS-SN and WISE photometry. The repetition of methods ensures both homogeneity through all of the calibrating variables, a clean

sample of RRLs, and that the metallicity used in the PLZ relation will be consistent with that derived from this works photometric metallicities. Markov chain Monte Carlo was applied to derive the PLZ/PWZ relations.

In order to test the performance of the newly derived PLZ and PWZ relations, distance moduli were obtained for the Sculptor dwarf spheroidal galaxy (finding $\bar{\mu}_0 = 19.47 \pm 0.06$) and the globular clusters M4 ($\bar{\mu}_0 = 11.16 \pm 0.05$) and Reticulum ($\bar{\mu}_0 = 18.23 \pm 0.06$). The distance moduli determined through all of this dissertation's PLZ/PWZ relations are internally self-consistent (within $\lesssim 0.05$ mag). A comparison with previous literature measurements taken from various methods/anchors reveals that this work's distance moduli are systematically smaller (by up to $\sim$ 2-3σ). Similarly, other RRL EDR3 anchored calibrations likewise show, to varying extents, a systematically smaller distance modulus for the RRL relations when compared to Gaia DR2 anchored calibrations. The difference between the average distance moduli for HST, Gaia DR2, and Gaia DR3 calibrations and this work is analyzed for each stellar system. Across each system, there is a consistent offset relative to this work of $\overline{\Delta\mu_0}(HST) = 0.22 \pm 0.11$ mag and $\overline{\Delta\mu_0}(DR2) = 0.12 \pm 0.08$ mag. This suggests that the differences in distance moduli noted are not due to any selection bias in the metallicity term of the PLZ and point toward biases in distance moduli related to the zero-point used in the respective PLZ calibrations.

5.2 Future Work

In the near future, the faint limiting magnitude of the Vera Rubin LSST Survey will allow time-series observations to be extended to the outer halo (up to $\sim$400 kpc for RRLs), where numerous RRLs are expected to be discovered. At these distances, large-scale spectroscopic and parallax measurements will be unfeasible. Only by utilizing the unique properties of RRLs as standard candles through PLZ/PWZ relations and the chemical abundances through photometric metallicities will we be able to derive distances and determine the chemical structure of the older population of the outer halo. Application of the methods/relations provided by this dissertation will provide key information on galactic evolution, addressing questions such as: Is there any

trace of a radial metallicity gradient throughout the halo? Can we see any stellar overdensities or anisotropy in the spatial or chemical abundances indicative of unknown ultra-diffuse galaxies?

Whether in the mid-infrared or optical for the RRab or RRc, the relations and methods presented here will be crucial to facilitate the quick determination of reliable RRL metallicities for the many upcoming wide-area time-domain surveys and ELTs. The mid-infrared relations will allow present and future infrared telescopes (such as JWST and the Nancy Roman telescope) to reach RRLs in high-extinction environments where spectral observations are not feasible.

Although photometric metallicities have been around for more than a quarter of a century, this work shows there remains significant room for improvement. This is shown both through the discovery of systematic bias in literature relations and in the presentation of alternative fitting/calibration methodologies. The emphasis on photometric metallicity accuracy will gain increasing prevalence in the near future as astronomers must increasingly rely more upon photometric over spectroscopic techniques in more extreme environments.

One way to improve accuracy is to provide further photometric metallicity relations. For bands without a readily available period-ϕ_{31}-[Fe/H] calibration, additional conversions are often made (see Chap 2) to transform the observed Fourier parameter to its approximate equivalent in another wavelength in order to be used in available literature Period-Fourier-metallicity relations. This technique is commonly utilized and will provide first-order abundances for immediate chemo-structural analysis. Direct calibrations in each band are ideal to avoid introducing additional sources of error but are usually lacking even in standard filters from large surveys. Currently, for LSST (possessing u,g,r,i,z,y filters), only the g and r bands have directly calibrated photometric metallicity relations for RRab (Ngeow, 2022). Gaia currently provides photometric metallicities, but the utilized relation was calibrated in a different band and then applied using a transformation of Fourier parameters. Gaia's photometric relation also suffers from systematic biases (see Chap 2), and metallicities are only provided for the G-band. Work has yet to be provided for direct calibration of the BP and RP Gaia bands.

This dissertation provides the impetus for a framework of photometric relations to be derived across multiple bands. As shown in this work, when multiple bands are calibrated and used in conjunction, it will narrow down the error in photometric metallicity. Furthermore, accurate metallicities have now been shown to be available out to the mid-infrared.

To further ensure accuracy in the proposed RRL photometric metallicity calibrations, future works should seek to increase the number of spectroscopic metallicity calibrators in the extreme metal-poor ([Fe/H]< -2.5) and rich ([Fe/H]> -0.5) RRL populations. These subsets are critical in calibrating both PLZ/PWZ relations and photometric metallicities. As shown by Chap 2 and 3, most literature photometric metallicity calibrations suffer from major systematic biases in part due to a lack of high/low metallicity calibrators. Through the recent creation of an extensive metallicity catalog that possesses field RRLs in both metallicity extremes, I was able to provide critical calibration leverage and create more accurate period-Fourier-metallicity relations.

However, even then, this crucial leverage is provided by $< 2\%$ of the total spectroscopic metallicity sample population. By applying the optical and infrared photometric metallicity calibrations presented in this work to the entire RRL sample identified with Gaia and possessing available ASAS-SN/ WISE photometry, one can easily identify a metal-poor/rich sample 2-3 orders of magnitude greater than that currently available with spectroscopy. This sample set would be an excellent candidate for follow-up spectroscopic observations, as these RRL sample sets are nearly uniform across the sky. The high-precision metallicities derived from these observations will be ideal in pinning down the area of largest uncertainty in photometric metallicity calibrations.

As an equally important byproduct, these extreme metal-poor/rich populations can provide us with more detailed information to pursue galactic/stellar evolutionary questions. By analyzing the extreme metal-poor population, astronomers can get the earliest glimpse into all galaxy components before significant chemical enrichment has occurred. On the opposite extreme, even though RRLs are older (age > 10 Gyr) population II stars, a subset of these stars possess solar-level abundances. These RRLs are likely the result of binary evolution, causing a younger,

more metal-rich population to develop to the HB instability strip stage quicker than it would solitarily (Bobrick et al., 2022). However, the type of binary interaction needed to explain this metal-rich extreme population is solely theoretical and poorly constrained observationally; there are only two bona fide RRL found in a binary system. Analyzing the chemical enrichment via spectroscopy of a larger sample could tell us crucial information on any fundamental differences between these metal-rich RRLs and the slightly more metal-poor bulk of the RRLs, ultimately helping to constrain evolutionary models.

There exist countless more diverse uses for the chemical abundance and distance methods provided here, as the era of large-scale time-series surveys is inundating us with vast amounts of photometric data across all Local Group components.

5.3   References

Bobrick, A., Iorio, G., Belokurov, V. et al (2022). RR Lyrae From Binary Evolution: Abundant, Young and Metal-Rich. *arXiv e-prints*, page arXiv:2208.04332.

Crestani, J., Fabrizio, M., Braga, V.F. et al (2021). On the Use of Field RR Lyrae as Galactic Probes. II. A New ΔS Calibration to Estimate Their Metallicity. *The Astrophysical Journal*, 908(1):20.

Mullen, J.P., Marengo, M., Martínez-Vázquez, C.E. et al (2022). Metallicity of Galactic RR Lyrae from Optical and Infrared Light Curves. II. Period-Fourier-Metallicity Relations for First Overtone RR Lyrae. *The Astrophysical Journal*, 931(2):131.

Mullen, J.P., Marengo, M., Martínez-Vázquez, C.E. et al (2023). RR Lyrae Mid-infrared Period-Luminosity-Metallicity and Period-Wesenheit-Metallicity Relations Based on Gaia DR3 Parallaxes. *The Astrophysical Journal*, 945(1):83.

Mullen, J.P., Marengo, M., Martínez-Vázquez, C.E. et al (2021). Metallicity of Galactic RR Lyrae from Optical and Infrared Light Curves. I. Period-Fourier-Metallicity Relations for Fundamental-mode RR Lyrae. *The Astrophysical Journal*, 912(2):144.

Ngeow, C.C. (2022). Evaluating the V-band Photometric Metallicity with Fundamental Mode RR Lyrae in the Kepler Field. *The Astrophysical Journal*, 164(2):45.